Developments in finite element simulations of aluminium extrusion

Joeri Lof

DEVELOPMENTS IN FINITE ELEMENT SIMULATIONS OF ALUMINIUM EXTRUSION

PROEFSCHRIFT

ter verkrijging van
de graad van doctor aan de Universiteit Twente,
op gezag van de rector magnificus,
prof. dr. F. A. van Vught,
volgens besluit van het College voor Promoties
in het openbaar te verdedigen
op vrijdag 8 september 2000 te 15:00 uur.

door

Joeri Lof
geboren op 14 maart 1973
te 's-Hertogenbosch

Dit proefschrift is goedgekeurd door de promotoren:

Prof. dr. ir. J. Huétink

Prof. dr. ir. F. J. A. M. van Houten

Summary

Aluminium extrusion is a forming process used to produce profiles. A large variety of profiles can be made by pressing a billet of hot aluminium through a hole that closely resembles the required cross-section of the profile. At the present time, design of extrusion dies and operation in extrusion companies is primarily based on trial and error. The experience of the die designer, the press operator and the die corrector to a large extent determine the performance of the process. In order to improve the performance, it is necessary to have more knowledge about the extrusion process. Numerical simulations can be a valuable tool in obtaining such knowledge.

In this thesis some new developments in the simulation of aluminium extrusion with the finite element method are reported. The subject matter is presented in four chapters, which have also been submitted as articles for publication elsewhere. Attention is focussed on the following three topics:

- Modelling the bearing area.

- Experimental verification of the simulations.

- Development of a practical method for the simulation of arbitrary profiles.

In the simulation of extrusion, it is common to use a viscoplastic constitutive model to describe the material behaviour and thus neglect the elastic properties of the material. The reason for this is that the elastic deformations are small compared to the very large plastic deformations that occur during the process. However, inside a parallel bearing channel, the deformations of the material are minimal and elastic effects do have a significant effect on the results.

To investigate the phenomena that occur in the bearing area, detailed 2D simulations of the aluminium flow in this area are performed. With these simulations, the effect of

material behaviour, friction and bearing geometry is investigated. From the results, it can be concluded that elastic effects play an important role in parallel bearings. It is also demonstrated that the resistance in parallel bearings is very sensitive to small changes in bearing geometry and process conditions. This explains the unpredictable behaviour of extrusion dies observed in practise. To avoid this unpredictable behaviour a new design approach is suggested.

Experimental verification of the numerical results is provided by comparing simulations to laboratory scale extrusion experiments. The numerical simulations are performed with a general solute-dependent elasto-viscoplastic constitutive model based on the Sellars-Tegart law. The parameters for this model are determined with compression tests. The extrusion trials are performed isothermally. The results of the numerical simulations showed good agreement with the experimental results.

The application of the numerical simulations in the extrusion industry is limited because of the complexity of these simulations. To overcome this obstacle, a practical method is developed which can be used for the simulation of arbitrary profiles. An equivalent bearing model is developed to model the resistance in the bearing area, without using a large number of elements. To avoid the time-consuming and complex work necessary for the development of the FEM model for a particular die, a specialised pre-processor is developed. This pre-processor provides a direct link between the die design in the CAD system Pro/Engineer and the simulations in the FEM code DiekA.

The simulations can be used in practise to investigate particular aspects of the extrusion process. The simulations have already been used successfully to improve the cross-sectional shape of legs used in porthole dies and to develop a design rule which can be used to determine the bearing geometry in order to obtain a uniform exit velocity of the profile. In principle, the simulations can also be used directly in the design process to improve the design of specific dies.

Acknowledgments

This research was carried out within the framework of the Eureka project IPECTIES. This project was initiated by BOAL B.V. in the Lier, the Netherlands and PHOENIX S.P.A. in Paderno, Italy. I would like to thank Kjell Nilsen and Mr. Lombardi for their commitment to this research. I also like to thank them and Peter Koenis, Dick van Beekhoven and Aad Knapen from BOAL for the pleasant cooperation during the project. The same holds for Andrew den Bakker who is no longer working for BOAL.

At the university I have worked with a number of people on extrusion research. First and foremost I would like to thank Han Huétink who has been my supervisor during this project. Thanks to Tom Vaneker, Fred van Houten and Joop Brinkman for the nice cooperation. I would also like to thank Herman Mooi who provided, with his research, the basis for my work. During the past four years, Reinier van Rossum, Arjan Klomp, Gerrit Klaseboer, Wenhua Cao, Yvo Blokhuis and Kasper Valkering worked for longer or shorter periods on the project. I would like to thank them not only for their contribution to this research, but also for the nice times.

The fourth chapter of this thesis is the result of a cooperation with the materials science department of the Technical University of Delft. The work on hot deformation modelling and the extrusion trials presented in this chapter were financially supported by the Technology Foundation (STW). I would like to thank Jörgen van de Langkruis, Pim Kool and Sybrand van der Zwaag for the great cooperation.

Furthermore I would like to thank all the members of the DiekA group for the nice time I had working here the last four years. I would especially like to mention Ton van de Boogaard and Bert Geijselaers for their contribution with regard to the contents of my thesis. Thanks to Debbie Zimmerman and Annemarie Teunissen for their supporting activities and to Nico van Vliet for his support with computer related issues. Katrina Emmett is acknowledged for the correction of the English language. I like to thank Frits van Eerden for being my roommate for four years, which must have been hard.

Contents

Chapter 1

Introduction

Aluminium extrusion is a forming process used to produce long, straight aluminium products, called profiles. A large variety of profiles can be produced by pressing a billet of hot aluminium through a die orifice which closely resembles the desired cross-section of the profile. In the industrial application of the extrusion process, die design and process control are mainly based on empirical knowledge. This empirical knowledge is not well documented and is to a large extent only accessible through the experience of die designers, die correctors and press operators. Because of this the performance of the extrusion process is mainly determined by the subjective influences of these people.

In recent years a trend can be observed towards a more objective documentation of the empirical knowledge available at extrusion companies. The development of automated design applications or expert systems can be seen as a part of this trend. These systems require the explicit formulations of design rules. To formulate such rules more knowledge of the mechanics behind the extrusion process is required. The finite element method (FEM) can be a valuable tool in obtaining such knowledge, providing insight into the process that cannot easily be obtained in any other way.

The work presented in this thesis is focussed on the development of numerical simulation tools for the extrusion process. This work is part of a larger research project which includes the following elements:

- Development of a semi-automatic die design application. The objective of this application is to reduce the subjective influences of the die designer on the design process and to significantly reduce the time required for the design.

- Development of numerical tools to simulate the extrusion process. The objective of this is to increase the knowledge of the extrusion process and to obtain objective design rules for extrusion dies.
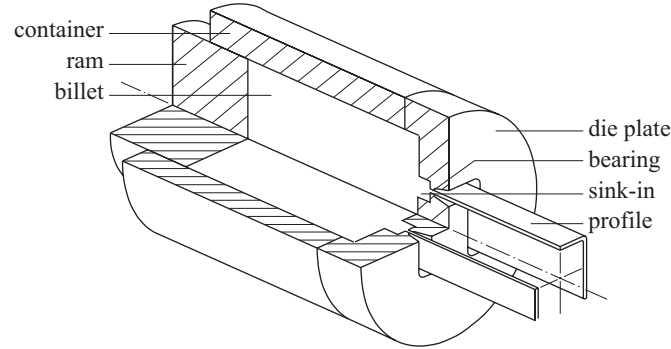
Figure 1.1: The extrusion process.
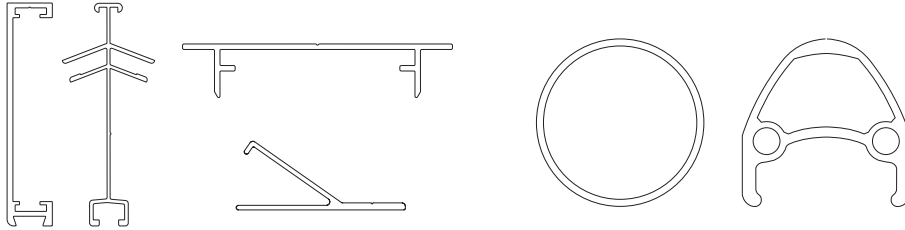
Figure 1.2: Examples of profiles (left: flat profiles; right: hollow profiles).

- Collection of empirical data on the extrusion process and verification of the design rules by means of experiments conducted in an industrial setting.

1.1 Aluminium extrusion

The work presented in this thesis is primarily aimed at the development of simulations tools for the direct extrusion process. An illustration is given in Figure 1.1. The direct extrusion process consists of the following steps. First, a preheated aluminium billet is loaded into the container. A ram presses this billet through a die, producing a profile with a cross-section determined by the shape of the die orifice. When the billet is almost completely extruded, the ram and container are retracted and the remaining part of the billet is sheared off. Then a new billet is inserted and the cycle is repeated.

A distinction must be made between the extrusion of solid profiles and the extrusion of hollow profiles, examples which are given in Figure 1.2. Solid profiles are generally
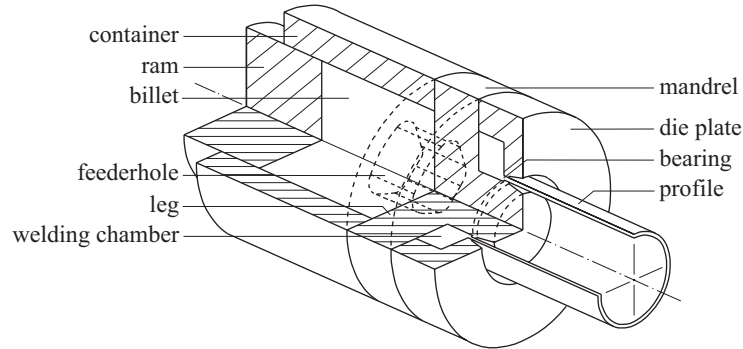
Figure 1.3: Extrusion of a hollow profile.

produced with a die that consists of only one part (flat die). Hollow profiles are produced with a porthole die, which consists of two parts, a mandrel to define the inner geometry of the profile and a die plate which defines the outer geometry. This is illustrated in Figure 1.3. In porthole dies, the aluminium flow is split by legs, which support the core. The material flows between the legs, through the feeder holes, and welds together in the welding chamber.

In the industrial application of extrusion, optimisation of process conditions is focussed on achieving the maximum extrusion speed, for which the quality requirements imposed on the product are still satisfied. The process window is limited by two factors, the maximum extrusion load and the maximum exit temperature (see Figure 1.4). The maximum extrusion load is either imposed by the strength of the die or by the maximum capacity of the extrusion press. The extrusion load can be lowered by increasing the initial temperature of the billet. However, this is limited by the maximum exit temperature of the material. When this temperature gets too high, surface defects or even melting of the material can occur. So basically optimisation of the process comes down to choosing an optimum initial temperature. In practise it is not possible to achieve the optimised process conditions, because of the variation in temperature which occurs during the extrusion cycle and between different dies. As a result, the process has to be operated under conditions which are below the optimum.

In the design of extrusion dies, a major challenge is to obtain a uniform exit velocity over the entire cross-section of the profile. When profile thickness varies or when the material flow to part of the profile is restricted by the die, the exit velocity tends to be non-uniform. This is even more complex for dies that contain multiple openings, because not only the exit velocity within the profile, but also the velocity between
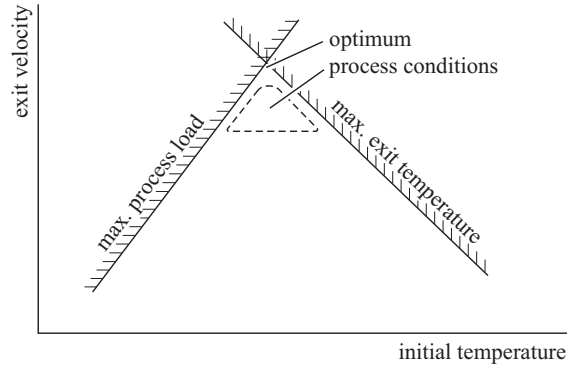
Figure 1.4: Optimisation of process conditions.

the profiles must be balanced. Several possibilities exist to control the exit velocity. The most direct influence is obtained at the bearing area. But exit velocity can also be controlled by an appropriate design of welding chamber and feeder holes.

At the moment, the design of extrusion dies is primarily based on the experience of the designer. When the die is manufactured, it is first tested in a trial pressing. Often a distorted or curved profile is produced during this trial pressing, caused by an unbalance in the exit velocity of the profile. If this is the case, the die is corrected in order to obtain a uniform exit velocity. After the correction, a new trial pressing is performed until the profile satisfies the requirements. At that point the die is used in production. During the production phase of a die, wear and plastic deformation occur. This requires additional corrections to the die and eventually causes the end of its lifespan.

The goal of the simulation tools developed here is to reduce the problems encountered in extrusion practise. The most important problem is the unpredictable behaviour of extrusion dies, which necessitates trial pressing and correction of most extrusion dies. A second problem is the lack of knowledge about the exact mechanics of the process. This complicates optimisation of the process conditions and hinders innovation in die design.

1.2 Numerical simulations of aluminium extrusion

The knowledge available on the extrusion process has been gathered primarily by experimental work and analytical calculations [1, 2]. It is only during the last 10 years that numerical simulations of aluminium extrusion have been reported in literature. This is largely due to the high computational demands that are associated with this kind of simulations. Early work was mainly concerned with 2D extrusion problems [3, 4, 5] or simple 3D geometries with low extrusion ratios [6, 7, 8]. With the increase of computer power more complex extrusion problems have been modelled. Simple porthole dies have been modelled in 3D by Tong [9] and by Mooi [10]. For these kinds of extrusion problems, pre-processing issues start to emerge. For the simulation of more complex profiles it is essential to automate large parts of the pre-processing. Van Rens [11] developed a meshing algorithm specifically aimed at the geometry associated with extrusion of thin-walled sections, enabling simulations of this type of profiles.

In the present work a number of developments in the numerical simulation of extrusion are reported. Attention is focussed on the following three subject areas:

- Modelling of the bearing area. This area is considered to be the most important area in the extrusion process, since most deformation occurs here. It is also the most difficult area to model in a FEM simulation because of its small scale compared to the rest of the process.

- Experimental verification of the numerical model.

- Development of a practical method for the simulation of the extrusion of complex profiles.

1.3 Overview of this thesis

This thesis consists of four main chapters, based on papers which have been submitted for publication elsewhere. As a consequence of presenting the material in this form, some of the subject matter is repeated. Material covered in preceding chapters is indicated with a vertical line in the left margin. Below, an overview is presented of the four papers and how they relate to the subject of this thesis.

Chapter 2: Adaptive return mapping algorithms for J_2 elasto-visco-plastic flow [12]

In simulations of aluminium extrusion, it is common to use a viscoplastic constitutive model and thus neglect the elastic properties of the material. To investigate whether this assumption is justified, simulations are performed with an elasto-viscoplastic model. This resulted in the development of a new method for modelling elasto-plastic and elasto-viscoplastic behaviour. This method can be considered a mix between an elasto-plastic and rigid-plastic model [13]. Subsequently, an elasto-viscoplastic model was developed which uses a new type of integration algorithm to calculate the incremental stress update. This algorithm is presented in Chapter 2.

The subject of this chapter is not directly related to aluminium extrusion simulations, since the method can be used to model general J_2 elasto-(visco)plastic material behaviour. However, the algorithm is suitable to describe the characteristics of hot aluminium alloys. The article also introduces a very straightforward method in which rate dependent behaviour can be introduced into the constitutive equations.

Chapter 3: Elasto-viscoplastic FEM simulations of the aluminium flow in the bearing area for extrusion of thin-walled sections [14]

The bearing area is the most difficult area to model in the extrusion process. In this article the characteristics of the aluminium flow in the bearing area are investigated. To this end a detailed 2D model of the bearing area is constructed. The influence of the elastic behaviour of aluminium in the bearing channel is investigated. This requires a modification to the Sellars-Tegart law, in order to include an elastic region in the constitutive behaviour.

The model is also used to investigate the influence of a number of design parameters. The results of these simulations show that in parallel bearings sudden changes in contact behaviour can occur. This makes the resistance in this type of bearing very sensitive to small changes in the geometry and in the extrusion conditions. This is considered to be the primary reason for the unpredictable behaviour of extrusion dies found in practise. To avoid this unpredictable behaviour, an alternative design approach for the bearing is suggested.

Chapter 4: Comparison of experimental AA6063 extrusion trials to 3D numerical simulations, using a general solute-dependent constitutive model. [15]

To assess the reliability of the simulations, it is important to have a good experimental verification of the numerical results. In Chapter 4, laboratory scale extrusion experiments are compared to numerical simulations. It is shown that a good agreement between experimental and numerical results can be obtained under well controlled experimental conditions and under the condition that an accurate description of the material properties is available. Small differences that still exist between numerical and experimental results can be attributed to the lack of material data for high strain rates and to dynamic precipitation that occurs under specific conditions.

Chapter 5: FEM simulations of the extrusion of complex thin-walled aluminium sections. [16]

In this chapter, attention is focussed on the development of a practical method for simulations of the extrusion of profiles with arbitrary cross-sections. To avoid excessive detail in the bearing area, an equivalent bearing model is developed [17]. With this model it is possible to describe the resistance of the bearing channel without using a very large number of elements.

To avoid time-consuming work in the development of the FEM model, a specialised pre-processor is developed. This pre-processor is implemented in the 3D CAD application Pro-Engineer, providing a direct coupling between the design process and the FEM simulations. This pre-processor automatically generates the FEM model for a specific die with minimal effort on the part of the user, drastically reducing the time necessary for pre-processing. A simulation for a complex extrusion die is used as an example to show the current capabilities of the proposed method.

Additional work

In Appendix A, an overview of the theoretical background of the simulations is presented. Work of a more practical nature has also been published [18, 19]. In these papers, it is demonstrated how the results of the simulations can be used to improve the design of dies and to develop design rules.

References

[1] W. Johnson and H. Kudo. *The mechanics of metal extrusion.* Manchester University Press, 1962.

[2] K. Laue and H. Stenger. *Extrusion.* American Society for Metals, 1981.

[3] G. Grasmo, K. Holthe, S. Støren, H. Valberg, R. Flatval, L. Hanssen, M. Lefstad, O. Lohne, T. Welo, R. Ørsund, and J. Herberg. Modelling of two-dimensional extrusion. In *Proc. 5th International Extrusion Technology Seminar*, pages 367–376, Wauconda, Illinois, 1992. Aluminum Association and Aluminum Extruders Council.

[4] C. Devadas and O. Celliers. Metal flow during the extrusion proces. In *Proc. 5th International Extrusion Technology Seminar*, volume 1, pages 359–368, Wauconda, Illinois, 1992. Aluminum Association and Aluminum Extruders Council.

[5] B. S. Kang, B. M. Kim, and J. C. Choi. Preform design in extrusion by FEM and its experimental confirmation. *J. Mater. Proc. Tech.*, 41:237–248, 1994.

[6] K. I. Mori, K. Osakada, and H. Yamaguchi. FE simulations of 3D extrusion of sections. In D. R. J. Owen, editor, *3rd Int. Conf. Comp. Plast.*, pages 1139–1149. Pineridge Press, 1992.

[7] M. Kiuchi, J. Yanagimoto, and V. Mendoza. Flow of solid metal during extrusion: 3D simulations by FE method. In Shen and Dawson, editors, *Simulation of Materials Processing: Theory Methods and Applications*, pages 847–852, Rotterdam, 1995. Balkema.

[8] Y. S. Kang and D. Y. Yang. Investigation into the thermo-viscoplastic finite element analysis of square die extrusion of square section with Lagrangian description. *Int. J. Mach. Tools Manufact.*, 36:907, 1996.

[9] L. Tong. *FE simulation of bulk forming processes with a mixed Eulerian-Lagrangian formulation.* PhD thesis, Swiss Federal Institute of Technology Zürich, Switserland, 1995.

[10] H. G. Mooi. *Finite element simulation of aluminium extrusion.* PhD thesis, University of Twente, The Netherlands, 1996.

[11] B. J. E. van Rens. *Finite element simulations of the aluminium extrusion process.* PhD thesis, Technical University Eindhoven, The Netherlands, 1999.

[12] J. Lof and A. H. van den Boogaard. Adaptive return mapping algorithms for J_2 elasto-viscoplastic flow. *Int. J. Numer. Meth. Engng.*, 2000. submitted.

[13] J. Huétink, A. H. van den Boogaard, A. D. Rietman, J. Lof, and T. Meinders. A mixed elastoplastic / rigid-plastic material model. *Int. J. Numer. Meth. Engng.*, 46:1421–1434, 1999.

[14] J. Lof. Elasto-viscoplastic FEM simulations of the extrusion of the aluminium flow in the bearing area for extrusion of thin walled sections. *J. Mater. Proc. Tech.*, 2000. submitted.

[15] J. van de Langkruis, J. Lof, W. H. Kool, S. van der Zwaag, and J. Huétink. Comparison of experimental AA6063 extrusion trials to 3D numerical simulations, using a general solute-dependent constitutive model. *Comp. Mat. Sci.*, 2000. accepted for publication.

[16] J. Lof and Y. Blokhuis. FEM simulations of the extrusion of complex thin walled aluminium sections. *J. Mater. Proc. Tech.*, 2000. submitted.

[17] J. Lof and J. Huétink. Isothermal elasto-viscoplastic FEM simulations of the extrusion of a thin aluminium tube. *Comp. Mater. Sci.*, 2000. submitted.

[18] J. Lof, G. Klaseboer, J. Huétink, and P. T. G. Koenis. FEM simulations of aluminium extrusion using an elasto-viscoplastic material model. In *Proc. 7th International Extrusion Technology Seminar*, volume 2, pages 157–168, Wauconda, Illinois, 2000. Aluminum Association and Aluminum Extruders Council.

[19] J. Lof, J. Huétink, and K.E. Nilsen. FEM simulations of the material flow in the bearing area of the aluminium extrusion process. In *Proc. 7th International Extrusion Technology Seminar*, volume 2, pages 211–222, Wauconda, Illinois, 2000. Aluminum Association and Aluminum Extruders Council.

Chapter 2

Adaptive return mapping algorithms for J_2 elasto-viscoplastic flow

J. Lof and A. H. van den Boogaard

Abstract

In this paper a new class of integration algorithms for elasto-viscoplastic constitutive equations is proposed. It is based on the generalised trapezoidal rule, which is a weighted combination of the start and end of the increment. But instead of taking constant weights, the weights are a function of the plastic multiplier. In this way the magnitude of the plastic strain increment determines the way the integration is performed. The stress update and consistent tangent are derived for the case of J_2 flow. Several candidates within the class of adaptive return mapping algorithms are investigated. It is shown numerically that some of the proposed algorithms are more accurate than commonly used algorithms such as mean normal and radial return.

2.1 Introduction

A time-continuous model normally forms the basis for the constitutive equations in any numerical method for modelling elasto-viscoplastic material behaviour. In this time-continuous model the relation between stresses and strains in the inelastic domain is defined in a rate formulation. In a numerical solution procedure it becomes necessary to integrate the constitutive equations to obtain an incremental formulation. It is recognized that return mapping algorithms, like the generalised trapezoidal rule and the generalised midpoint rule are the most efficient for large scale inelastic computations. The accuracy and stability of these methods was analysed by Ortiz and Popov in their renowned paper [1].

Within the family of return mapping algorithms, the Euler backward integration, for J_2 flow also referred to as radial return method is the most popular. This method was first introduced by Wilkins [2] and further generalised later [3, 4]. Other return mapping algorithm include the trapezoidal rule, which is also known as the mean normal method [5], the closest point procedure [6] and the steepest decent method [7, 8]. As an alternative to return mapping algorithms, substepping algorithms can be used for the integration of the constitutive relations [9, 10]. A comparison between the return mapping and the substepping approach was made by Potts and Ganendra [11].

In the work presented in this paper, a generalised trapezoidal rule is used to integrate the constitutive relations. In other words, the integral is approximated by a weighted combination of the direction at the start and the end of the increment. Huétink et al. [12] proposed a model in which the constant weights of the generalised trapezoidal rule are replaced by weights dependent on the plastic multiplier. In this way an elastoplastic model was derived that degenerates to the rigid plastic model for large strain increments. In the present paper a class of adaptive return mapping algorithms is proposed which is also based on weights that are dependent on the plastic multiplier. The adaptive algorithm presented here is different from the one proposed by Huétink et al. because it consistently takes into account the elasticity in the model. Thus it does not degenerate to the rigid plastic model for large strain increments. For J_2 flow, the adaptive algorithm provides a very robust and accurate procedure. In principal the approach can also be applied to other plasticity models. However for models other than J_2, the complexity increases dramatically, limiting the practical applicability to J_2 flow. A general formulation of the adaptive algorithm is presented for elasto-viscoplastic J_2 flow. This makes the proposed algorithm very suitable for (hot) bulk metal forming simulations.

In Section 2.2 a time-continuous constitutive model is presented that can be used to model elastoplastic and elasto-viscoplastic material behaviour. Rate dependent material behaviour is often introduced by so-called overstress models, such as the Perzyna model [13] or the Duvaut-Lions model [14]. In these models the stress is allowed to be outside the yield surface. The part of the stress that is outside the yield surface (called the overstress) determines the viscoplastic strain rate. Simo and Hughes [15] give a thorough treatment on this subject and on the subject of return mapping algorithms. Wang [16] suggested to introduce viscoplastic behaviour by defining a 'yield' function which is rate dependent. This approach is adopted in the present paper and elaborated. It is shown that this results in an incremental formulation that is similar to the standard rate independent model with the exception that a time parameter is introduced into the incremental algorithm.

In Section 2.3 the time-continuous constitutive equations are integrated to derive an incremental formulation for the case of associative J_2 flow. The stress update algorithm and the consistent tangent modulus are derived for the general case that the interpolation factor is a function of the plastic multiplier. Since the algorithm is proposed for large strain increments, the algorithm must be applicable to large deformation analysis. Objective integration can be obtained by using a corotational formulation [17]. For simplicity, the algorithm is derived for infinitesimal deformations only.

In Section 2.4 some suitable functions for the integration weights are discussed. Here it is demonstrated that for the case of J_2 flow there is an obvious candidate which is not available for other plasticity models. In Section 2.5 the accuracy of the proposed adaptive return mapping algorithms are compared to standard return mapping algorithms, such as the radial return method and the mean normal method. It is shown that some members of the class of adaptive algorithms are more accurate than standard algorithms such as radial return. The proposed algorithm shows an interesting similarity to the rigid plastic formulation for large strain increments. This is discussed in Section 2.6. In this section the algorithm is also compared with the mixed elastoplastic / rigid plastic model proposed by Huétink *et al.*.

2.2 Time-continuous model

In this section a set of constitutive equations is presented that can be used to characterise a wide set of elasto-viscoplastic materials [18]. For simplicity only isotropic material behaviour is considered here. The equations are presented in rate form, with a superposed dot denoting a derivative with respect to time.

$$\dot{\boldsymbol{\varepsilon}} = \dot{\boldsymbol{\varepsilon}}^e + \dot{\boldsymbol{\varepsilon}}^{vp} \tag{2.1}$$

$$\dot{\boldsymbol{\sigma}} = \mathbf{E} : \left(\dot{\boldsymbol{\varepsilon}} - \dot{\boldsymbol{\varepsilon}}^{vp} \right) \tag{2.2}$$

$$\dot{\boldsymbol{\varepsilon}}^{vp} = \dot{\lambda} \frac{\partial Q}{\partial \boldsymbol{\sigma}} \tag{2.3}$$

$$g = g\left(\boldsymbol{\sigma}, \kappa, \dot{\kappa} \right) \tag{2.4}$$

$$\dot{\lambda} \geq 0 \, , \quad \dot{\lambda} g = 0 \, , \quad g \leq 0 \tag{2.5}$$

- Equation 2.1 is the rate form of the strain decomposition. The total strain $\boldsymbol{\varepsilon}$ is assumed to be the sum of an elastic part $\boldsymbol{\varepsilon}^e$ and a (visco)plastic part $\boldsymbol{\varepsilon}^{vp}$. Because the model presented here can be used to model rate dependent and rate independent behaviour, the inelastic part of the strain tensor is referred to as the plastic strain. For rate dependent plasticity this should be interpreted as viscoplastic strain.

- Equation 2.2 represents the linear elastic relation between the Cauchy stress $\boldsymbol{\sigma}$ and the elastic strain. The elastic behaviour is defined by the 4th-order tensor $\mathbf{E}$ representing the generalised Hooke's law.

- Equation 2.3 is the evolution law (flow rule) for the plastic strain rate. Q is a plastic potential which defines the direction of the plastic strain rate. $\dot{\lambda}$ is the plastic multiplier which is used to scale the plastic strain rate.

- Equation 2.4 represents the limit function g. This function describes the behaviour of the material in the plastic domain. It can be interpreted as a generalisation of the yield function from rate independent to rate dependent materials. The model is limited to isotropic material behaviour, dependent on the equivalent plastic strain and the equivalent plastic strain rate, defined by:

$$\dot{\kappa} = \sqrt{\tfrac{2}{3} \dot{\boldsymbol{\varepsilon}}^{vp} : \dot{\boldsymbol{\varepsilon}}^{vp}} \tag{2.6}$$

- Equations 2.5 are the Kuhn-Tucker loading-unloading conditions.

2.2.1   Limit function

The specific constitutive behaviour of the material is defined in (2.4) as a relation between the stress and the equivalent plastic strain and the equivalent plastic strain rate. In the case of a standard rate independent plasticity model, the plastic strain rate is removed and the limit function is equal to the yield function, which states that the effective stress $\overline{\sigma}$ is equal to the yield stress σ_y:

$$g = f\left(\boldsymbol{\sigma}, \kappa\right) = \overline{\sigma} - \sigma_y\left(\kappa\right) \tag{2.7}$$

When introducing rate dependent behaviour in the constitutive models, often a Perzyna-type model is used [13, 16, 19]. This model allows the stress to be outside the yield surface. The distance between the yield surface and the actual stress determines the evolution of the viscoplastic strain rate. This model can be described by defining the limit function as:

$$g\left(\boldsymbol{\sigma}, \kappa, \dot{\lambda}\right) = \gamma\phi\left(\overline{\sigma} - \sigma_y\left(\kappa\right)\right) - \dot{\lambda} \tag{2.8}$$

In which γ is a fluidity parameter and ϕ is an arbitrary positive function. The plastic multiplier $\dot{\lambda}$ is used as a measure for the plastic strain rate. In this paper a different approach is used, the relation between stress, strain and strain rate is directly given by the limit function. The limit function can be interpreted as a rate dependent yield function, which states that in the plastic region the effective stress $\overline{\sigma}$ must be equal to the flow stress σ_f:

$$g\left(\boldsymbol{\sigma}, \kappa, \dot{\kappa}\right) = \overline{\sigma} - \sigma_f\left(\kappa, \dot{\kappa}\right) \tag{2.9}$$

This way of defining the material behaviour is especially suitable for simulations of hot metal forming. At high temperatures, rate dependent effects become important in metals. The material laws that describe these effects are often written as a relation between effective stress and equivalent plastic strain and equivalent plastic strain rate, which can be directly used in (2.9). Examples of such models are the Norton-Hoff law which is a generalisation of the power law and the Sellars-Tegart law which can be used to describe the behaviour of hot aluminium alloys [20]. Hot metals can in general be described quite well by a J_2 flow rule.

2.3   Time discretisation

The rate formulation for the constitutive equations presented in Section 2.2 cannot be directly applied in a finite element model. To obtain an incremental formulation the

evolution law (2.3) has to be integrated over a finite time interval $[t_n, t_{n+1}]$. Using a generalised trapezoidal rule [1] this results in:

$$\Delta \boldsymbol{\varepsilon}^{vp} = \int_{t_n}^{t_{n+1}} \dot{\lambda} \frac{\partial Q}{\partial \boldsymbol{\sigma}} \mathrm{d}t \approx \Delta \lambda \left((1 - \alpha) \left[\frac{\partial Q}{\partial \boldsymbol{\sigma}} \right]_n + \alpha \left[\frac{\partial Q}{\partial \boldsymbol{\sigma}} \right]_{n+1} \right) \tag{2.10}$$

Generalising the notion of associative plasticity to viscoplasticity for J_2 flow the viscoplastic potential Q can be replaced by the limit function g. Differentiating g with respect to the stress, yields that the direction of the plastic strain is in the direction of the deviatoric stress. And hence the derivative in (2.10) can be replaced by the deviatoric stress $\mathbf{s}$. Equations 2.1 to 2.5 can be written in incremental form as:

$$\Delta \boldsymbol{\varepsilon} = \Delta \boldsymbol{\varepsilon}^e + \Delta \boldsymbol{\varepsilon}^{vp} \tag{2.11}$$

$$\Delta \boldsymbol{\sigma} = \mathbf{E} : \left(\Delta \boldsymbol{\varepsilon} - \Delta \boldsymbol{\varepsilon}^{vp} \right) \tag{2.12}$$

$$\Delta \boldsymbol{\varepsilon}^{vp} = \Delta \lambda \left((1 - \alpha) \mathbf{s}_n + \alpha \mathbf{s}_{n+1} \right) = \Delta \lambda \mathbf{s}^* \tag{2.13}$$

$$g_{n+1} = \sqrt{\tfrac{3}{2} \mathbf{s}_{n+1} : \mathbf{s}_{n+1}} - \sigma_f \left(\kappa_{n+1}, \dot{\kappa}_{n+1} \right) \tag{2.14}$$

$$\Delta \lambda \geq 0 \;, \quad \Delta \lambda g_{n+1} = 0 \;, \quad g_{n+1} \leq 0 \tag{2.15}$$

Here the deviatoric stress tensor $\mathbf{s}^*$ is introduced to denote the direction of the plastic strain during the increment. Note that the value of α determines the direction of $\mathbf{s}^*$. The values of the state variables κ_{n+1} and $\dot{\kappa}_{n+1}$ at the end of the increment are defined as:

$$\Delta \kappa = \sqrt{\tfrac{2}{3} \Delta \boldsymbol{\varepsilon}^{vp} : \Delta \boldsymbol{\varepsilon}^{vp}} = \Delta \lambda \sqrt{\tfrac{2}{3} \mathbf{s}^* : \mathbf{s}^*} \tag{2.16}$$

$$\kappa_{n+1} = \kappa_n + \Delta \kappa \tag{2.17}$$

$$\dot{\kappa}_{n+1} = \frac{\Delta \kappa}{\Delta t} \tag{2.18}$$

From the above equations it becomes apparent that there is no fundamental difference between the incremental formulation of rate dependent and independent constitutive behaviour. Both the equivalent plastic strain and equivalent plastic strain rate are calculated from the equivalent plastic strain increment. The only difference is the

16
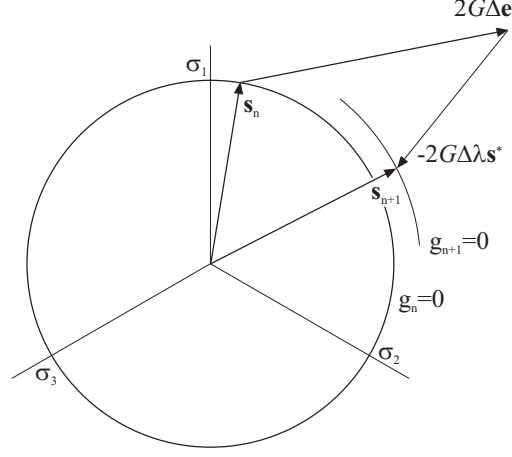
Figure 2.1: Return mapping algorithm in π-plane.

introduction of the constant time increment Δt, which introduces a time scale in the constitutive model.

Depending on the value of the interpolation factor α, different return mapping algorithms are obtained. Taking $\alpha = \frac{1}{2}$ coincides with the trapezoidal rule (mean normal), $\alpha = 1$ results in Euler backward integration (radial return). Huétink *et al.* [12] suggested to take α as a function of the plastic multiplier in order to obtain an algorithm that is a mix between an elastoplastic and a rigid plastic method. This suggestion is elaborated in this paper to define a class of adaptive integration algorithms for elasto-viscoplastic materials. In the next section, the stress update algorithm is derived for this class of algorithms.

2.3.1 Stress update algorithm

In a finite element application the constitutive equations are normally solved as a strain driven problem. From an estimate of the total strain increment first an elastic trial stress is calculated. If this trial stress satisfies the Kuhn-Tucker conditions it is assumed to be the actual stress and the material is in the elastic state. If the Kuhn-Tucker conditions are not satisfied by the elastic trial stress, the material is in the plastic domain. In this case the stress is calculated by enforcing the condition $g_{n+1} = 0$, as illustrated in Figure 2.1. When evaluating the deviatoric part of the

17

stress and strain only, this can be written as:

$$\mathbf{s}_{n+1} = \mathbf{s}_n + 2G\left(\Delta\mathbf{e} - \Delta\lambda\mathbf{s}^*\right) \qquad (2.19)$$

$$g_{n+1} = \sqrt{\tfrac{3}{2}\mathbf{s}_{n+1} \colon \mathbf{s}_{n+1}} - \sigma_f\left(\kappa_{n+1}, \dot{\kappa}_{n+1}\right) = 0 \qquad (2.20)$$

With G the shear modulus and $\Delta\mathbf{e}$ the deviatoric part of the total strain increment. On substituting (2.19) together with the definition of the state variables (2.16-2.18) into (2.20), a scalar equation for $\Delta\lambda$ is obtained. Depending on the type of constitutive model, sometimes an explicit expression for $\Delta\lambda$ can be found. However, in general $\Delta\lambda$ has to be determined iteratively. A Newton-Raphson method can be used to this end, but as illustrated in Appendix A, the derivative of g with respect to $\Delta\lambda$ is very expensive to compute. A much more efficient iterative procedure in this case is the secant method, which requires only the evaluation of g and not its derivative.

Obtaining a efficient global iteration process requires the derivation of the consistent tangent matrix. The consistent tangent follows from the linearisation of the stress update algorithm (2.19, 2.20). The consistent tangent for the adaptive return mapping algorithm is derived in Appendix B.

2.4   Candidate functions for $\alpha\left(\Delta\lambda\right)$

The integration algorithm as proposed in this paper requires a function which relates the interpolation weight α to the plastic multiplier $\Delta\lambda$. Some restrictions have to be made on this function. Because α weights between the start and end of the increment, it is bounded between 0 and 1. From the work of Ortiz and Popov [1] it is known that for J_2 flow and perfect plasticity, the generalized trapezoidal rule is unconditionally stable for $\alpha \geq \tfrac{1}{2}$. For values of $\alpha < \tfrac{1}{2}$ it is possible that the return mapping fails to intersect the limit surface $g_{n+1} = 0$, as illustrated in Figure 2.2. The lower limit for α is defined by the point where the return mapping direction $\mathbf{s}^*$ is tangent to the limit surface.

To derive an expression for the lower limit of α as a function of $\Delta\lambda$, one should consider that normally the return mapping actually has two solutions, indicated with $\Delta\lambda_1$ and $\Delta\lambda_2$ in Figure 2.2. At the point at which the return mapping is tangent to the limit surface, the return mapping only has one solution, indicated with $\Delta\lambda_c$. For perfect plasticity the solution of the return mapping can be calculated explicitly by
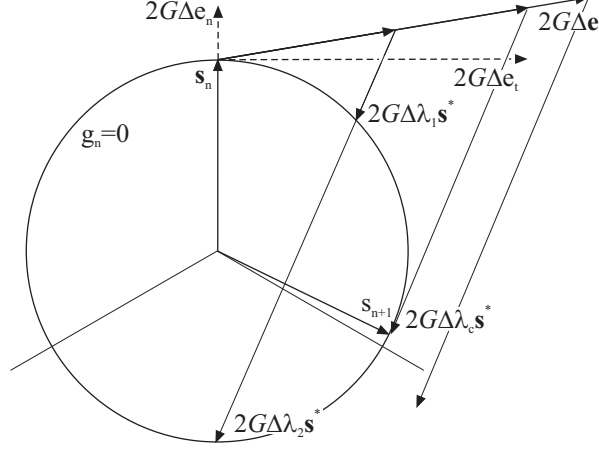
Figure 2.2: Three situations for the return mapping: two intersections points; tangent to $g_n = 0$; no intersection.

substituting (2.13) and (2.19) into (2.20). After some manipulation, the following expression can be derived:

$$\tfrac{2}{3}\sigma_f^2 G\left(2\alpha - 1\right)\Delta\lambda^2 + \left(\tfrac{2}{3}\sigma_f^2 + 2G(1-\alpha)\Delta\mathbf{e}:\mathbf{s}_n\right)\Delta\lambda - \left(G\Delta\mathbf{e} + \mathbf{s}_n\right):\Delta\mathbf{e} = 0 \tag{2.21}$$

This is a quadratic equation in $\Delta\lambda$ for which the solution is known explicitly. From Figure 2.2 it can be seen that the most critical direction for the strain increment is tangent to $g_n = 0$ at $\mathbf{s}_n$. For these strain increments, the contraction $\Delta\mathbf{e}:\mathbf{s}_n$ is equal to zero. The solution of (2.21) is then given by:

$$\Delta\lambda = \frac{-1 \pm \tfrac{1}{2}\sqrt{\tfrac{2}{3}\sigma_f^2\left(\tfrac{2}{3}\sigma_f^2 + \left(2\alpha - 1\right)4G^2\Delta\mathbf{e}_t:\Delta\mathbf{e}_t\right)}}{2G\left(2\alpha - 1\right)} \tag{2.22}$$

From this equation it can be seen that for $\alpha \geq \tfrac{1}{2}$ indeed there are always two solutions. For $\alpha < \tfrac{1}{2}$, the critical value of the plastic multiplier $\Delta\lambda_c$ is determined by the condition that the discriminant equals zero. In that situation we have:

$$\Delta\lambda_c = \frac{-1}{2G\left(2\alpha - 1\right)} \tag{2.23}$$

For the return mapping to have a solution we must require $\Delta\lambda \leq \Delta\lambda_c$, which yields the following condition for α:

$$2\alpha \geq 1 - \frac{1}{2G\Delta\lambda} \tag{2.24}$$

19
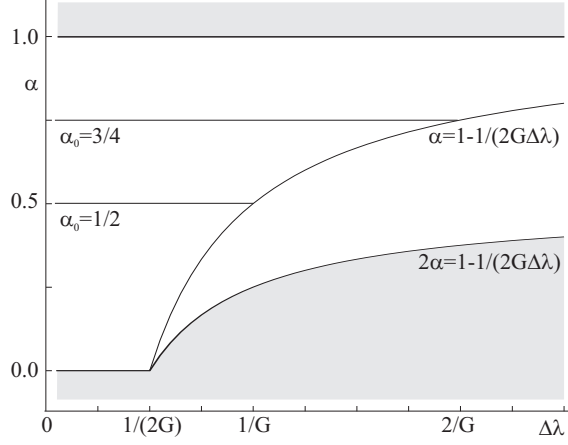
Figure 2.3: C^0-continuous candidates for α.

In Figure 2.3 the values of α in which the return mapping algorithm has a solution is indicated (white area). In order to obtain a suitable function α, the following consideration is made. In the stress update (2.19), the new stress depends on the initial stress and the plastic strain increment. For large strain increments it can be argued that the influence of the initial stress $\mathbf{s}_n$ vanishes. This can be achieved by taking α as (indicated in Figure 2.3):

$$\alpha = 1 - \frac{1}{2G\Delta\lambda} \tag{2.25}$$

With this choice for α the stress update (2.19) reduces to:

$$\mathbf{s}_{n+1} = \frac{\Delta\mathbf{e}}{\Delta\lambda} \tag{2.26}$$

It must be noted here that the elimination of the initial stress $\mathbf{s}_n$ by a scalar α is only possible for J_2 flow. For more general plasticity models it is necessary to use a fourth order tensor for α in order to eliminate the initial stress. This drastically increases the complexity of the model.

The above choice for α (2.25) is obviously not suitable for small strain increments because the value of α becomes negative. For low values of $\Delta\lambda$ the value of α can be bounded to a minimum value α_0.

$$\alpha = \max\left(\alpha_0, 1 - \frac{1}{2G\Delta\lambda}\right), \qquad 0 \leq \alpha_0 \leq 1 \tag{2.27}$$
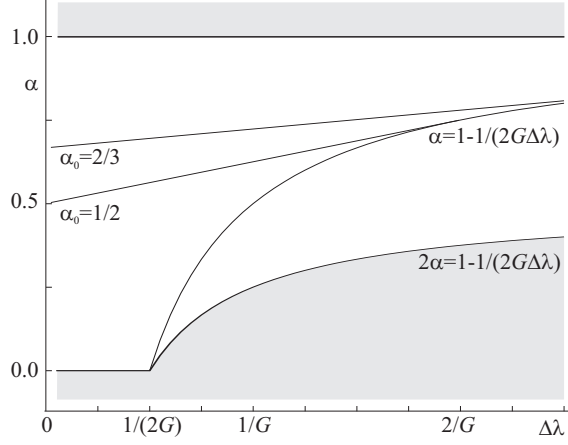
Figure 2.4: C^1-continuous candidates for α.

At the transition between the constant α_0 and the function defined by (2.25), the derivative of α is not defined. This means that a consistent tangent cannot be computed at that point. In the practical application of the algorithm it does not pose a problem to use either the derivative of α to the left or the right of the transition point.

Another possible function for α is illustrated in Figure 2.4. To preserve C^1-continuity at the transition, for low values of $\Delta\lambda$, α is taken as a linear function, tangent to the function proposed in (2.25). Such a function is completely defined by choosing a value α_0 at $\Delta\lambda = 0$:

$$\alpha = \max\left(\alpha_0 + \frac{(1-\alpha_0)^2}{2}G\Delta\lambda, 1 - \frac{1}{2G\Delta\lambda}\right), \qquad 0 \leq \alpha_0 \leq 1 \qquad (2.28)$$

With this choice for α a consistent tangent can be computed for every value of $\Delta\lambda$.
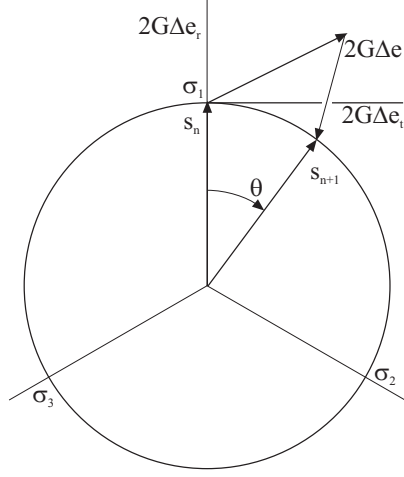
Figure 2.5: π-plane indicating deviatoric stress and strain increments.

2.5   Iso-error maps

To evaluate the accuracy of the proposed algorithm a comparison is made with standard integration algorithms. This comparison is performed for perfect plasticity, but the results are typical for more complex strain and strain rate dependent constitutive models.

In Figure 2.5 the initial stress $\mathbf{s}_n$ is plotted in the π-plane. From this initial state a prescribed deviatoric strain increment $\Delta\mathbf{e}$ is applied. Depending on the integration algorithm a new stress $\mathbf{s}_{n+1}$ is calculated somewhere on the yield surface. This stress can be characterised by the angle θ. The exact solution for the angle θ is known from [3]. The error (in degrees) that is made by the return mapping algorithm is plotted in iso-error maps (Figures 2.6-2.8), in which the axis represent the radial and the tangential components of the strain increment $\Delta\mathbf{e}$.

In case of hardening and especially strain rate dependent behaviour, an accurate prediction of the equivalent plastic strain increment is important. The accuracy in θ is an indication of the error in the direction of the stress, whereas the accuracy in $\Delta\kappa$ indicates the error in the magnitude of the stress by (2.9). Iso-error maps for $\Delta\kappa$ (%) are also presented in Figures 2.6-2.8.
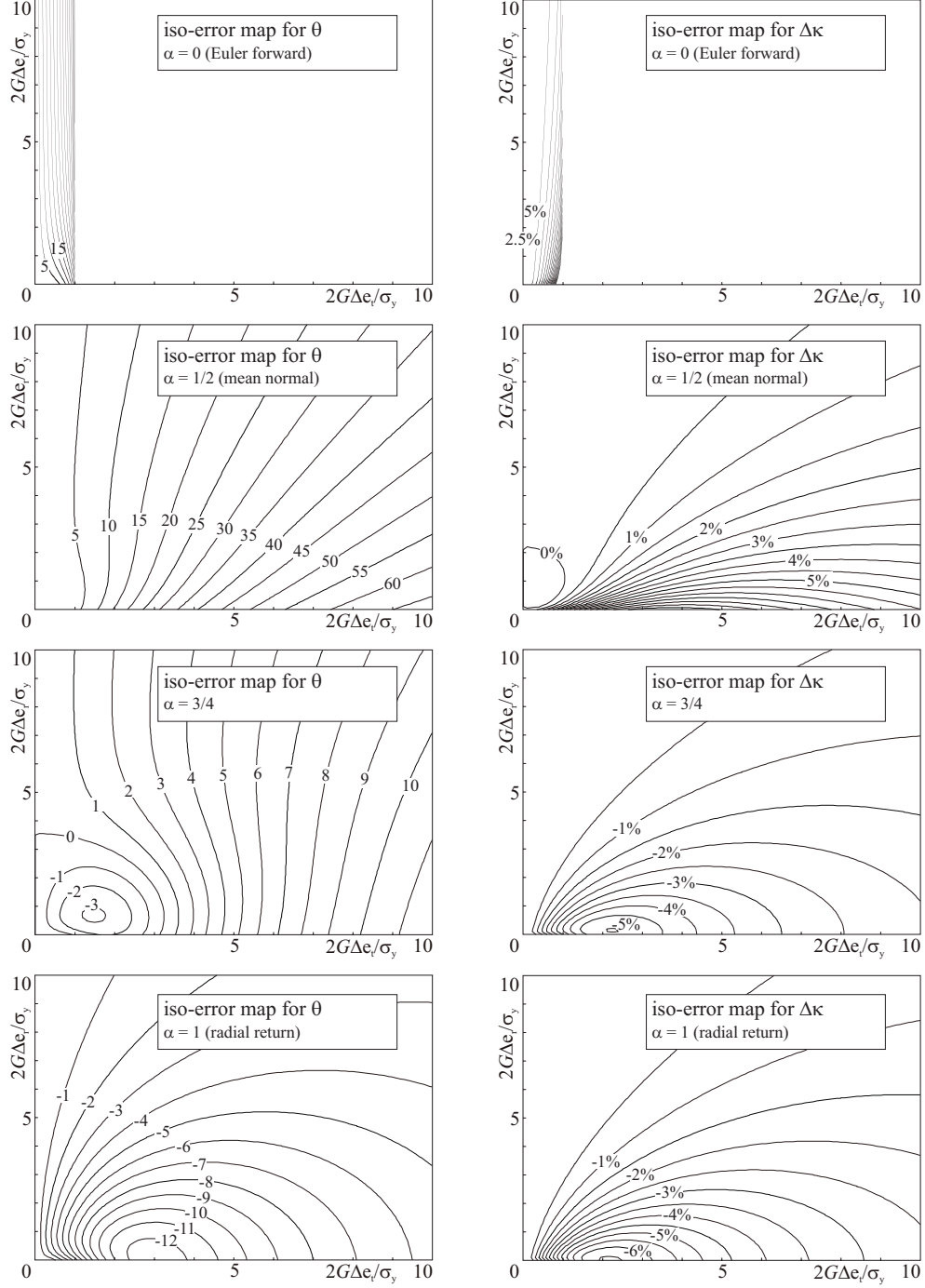
Figure 2.6: Iso-error maps for standard return mapping algorithms.
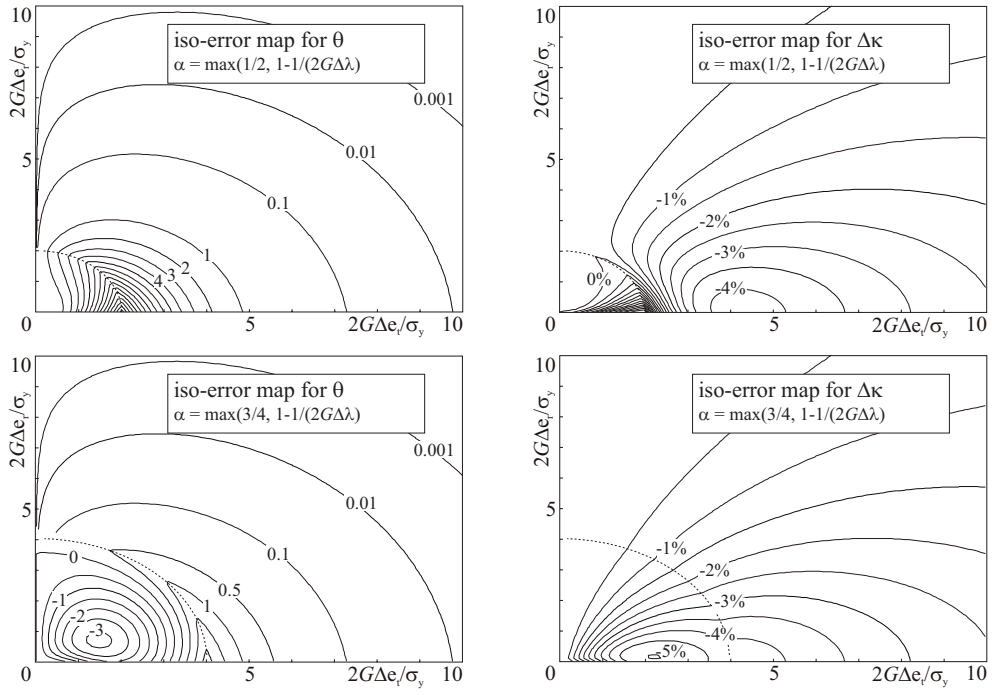
Figure 2.7: Iso-error maps for algorithm with C^0-continuous α.
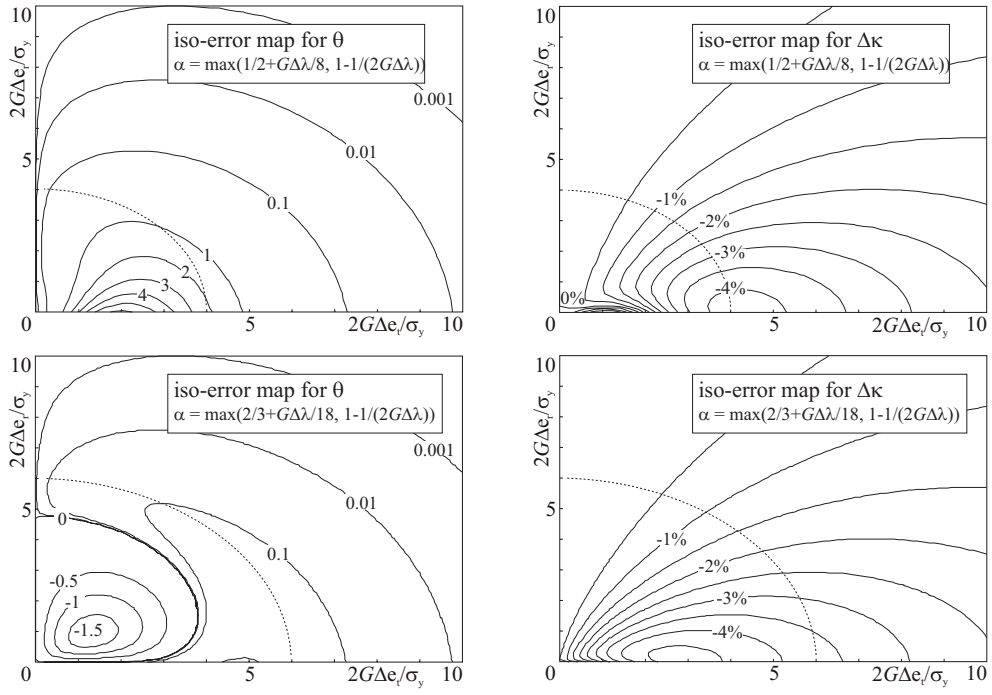
Figure 2.8: Iso-error maps for algorithm with C^1-continuous α.

2.5.1 Discussion of the iso-error maps

In Figure 2.6 the iso-error maps for the return mapping algorithm with constant α are plotted. The figure includes iso-error maps for Euler forward integration ($\alpha = 0$), the mean normal method ($\alpha = \frac{1}{2}$), the radial return method ($\alpha = 1$) and also for the case that $\alpha = \frac{3}{4}$. It is clear that the explicit Euler forward algorithm is only suitable for very small strain increments. The mean normal method is the only return mapping algorithm that is second order accurate. However, it is demonstrated in Figure 2.6 that for large strain increments the accuracy reduces dramatically. For the remaining two algorithms ($\alpha = \frac{3}{4}$ and $\alpha = 1$), the accuracy is reasonable. For small strain increments, the algorithm with $\alpha = \frac{3}{4}$ shows a good accuracy, however, for larger strain increments, the error increases. Radial return is the only algorithm that approaches the exact solution when the increments approach infinity.

In Figure 2.7, the iso-error maps for two of the adaptive return mapping algorithms are presented. Both algorithms are based on α defined by (2.27) with constant values of $\alpha_0 = \frac{1}{2}$ and $\alpha_0 = \frac{3}{4}$. The value $\alpha_0 = \frac{1}{2}$ is chosen because it is the only choice which gives a second order accurate integration for small values of the strain increment. However by numerical experimentation it turned out that a value $\alpha_0 = \frac{3}{4}$ resulted in the lowest maximum error. It is apparent that for large strain increments, the solution approaches the exact solution much faster than the radial return algorithm. This indicates that the choice to eliminate the initial stress $\mathbf{s}_n$ from the stress update, results in a very accurate algorithm for large strain increments. The dotted circle represents the transition between the two parts of the algorithm. Inside this circle the iso-error maps are equal to the corresponding maps in Figure 2.6. The algorithm with $\alpha_0 = \frac{3}{4}$ shows an overall better accuracy than the return mapping algorithm with constant α. It combines the high accuracy of a constant value of $\alpha = \frac{3}{4}$ for small strain increments and the high accuracy of (2.25) at high strain increments.

In Figure 2.8 the iso-error maps of the C^1-continuous adaptive return mapping algorithms defined by (2.28) are plotted. Two maps are plotted with starting values $\alpha_0 = \frac{1}{2}$ and $\alpha_0 = \frac{2}{3}$. Again $\alpha_0 = \frac{1}{2}$ was used as a starting value, it turned out that $\alpha_0 = \frac{2}{3}$ produced the best results. Outside the dotted circle the plots are identical to those of Figure 2.7. But in contrast to the maps in Figure 2.7, the iso-error contours are smooth on the transition. This is due to the C^1-continuity of α. Especially the second plot with $\alpha_0 = \frac{2}{3}$ shows significantly increased accuracy compared to standard algorithms such as radial return. The maximum error reduces from around $12°$ to approximately $1.5°$.
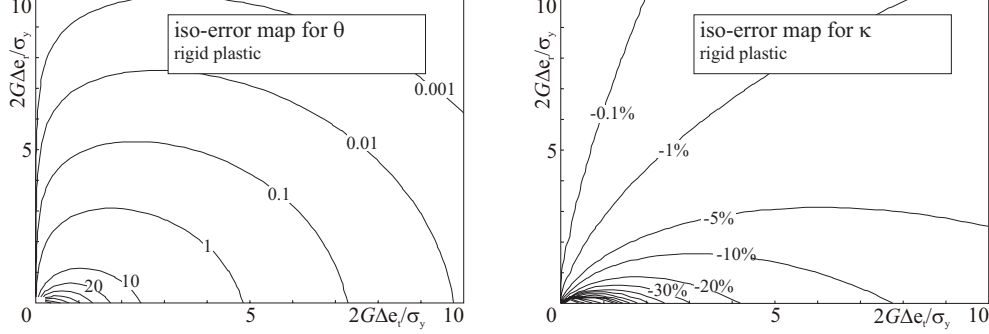
Figure 2.9: Iso-error maps for the rigid plastic model.

2.6   Connection to rigid plastic model

For large strain rates, the adaptive return mapping algorithm shows an interesting similarity to the rigid plastic formulation. In a rigid plastic model (also referred to as flow formulation) the elastic behaviour of the material is neglected. The deviatoric part of this model can be characterised by the following incremental formulation:

$$\mathbf{s}_{n+1} = \frac{\Delta \mathbf{e}}{\Delta \gamma} \tag{2.29}$$

$$g_{n+1}\left(\kappa, \dot{\kappa}\right) = 0 \tag{2.30}$$

Where $\Delta\gamma$ is a scaling parameter like the plastic multiplier, that is solved by enforcing (2.30). This formulation is very similar to the stress update for large strain increments (2.26) of the model proposed in this paper. The mixed elastoplastic / rigid plastic model proposed by Huétink *et al.* [12] takes advantage of this similarity by replacing the elastoplastic model by a rigid plastic model for large strain increments.

The difference in the stress update for large strain rates in the adaptive algorithm compared to the rigid plastic model and also to the mixed elastoplastic / rigid plastic model is the evaluation of the equivalent plastic strain and equivalent plastic strain rate. In the model proposed in this paper, the equivalent plastic strain and the equivalent plastic strain rate are updated by taking the plastic part of the total strain increment only (2.16). In the rigid plastic model they are determined based on the total strain increment:

$$\Delta \kappa = \sqrt{\tfrac{2}{3} \Delta \mathbf{e} \colon \Delta \mathbf{e}} \tag{2.31}$$

27
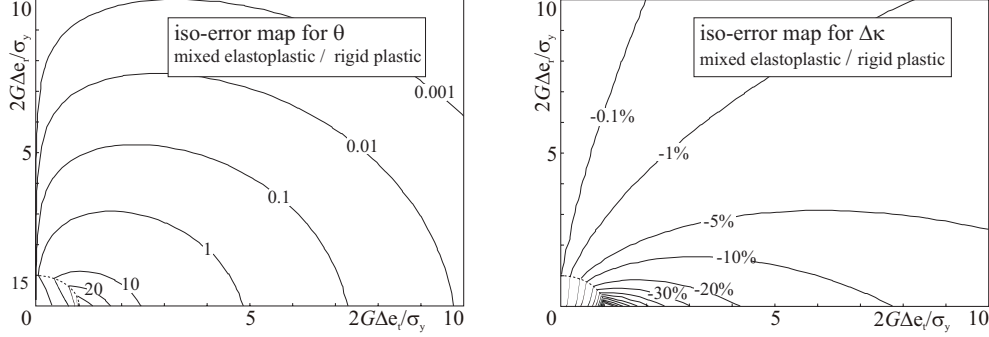
Figure 2.10: Iso-error maps for the mixed elastoplastic / rigid plastic model.

So the essential difference between the two models is that in the rigid plastic model the contribution of elastic strain is neglected in the evolution of the state variables.

In Figure 2.9 and 2.10, iso-error maps are presented for the rigid plastic and the mixed elastoplastic / rigid plastic model. In these maps it is apparent that the rigid plastic and the mixed model shows the same accuracy for the stress in the case of large strain increments, as the adaptive return mapping presented in this paper. The rigid plastic model shows a very large error for small strain increments because the elastic part of the strain is neglected. This problem is partly solved in the mixed model. It could be improved even more by increasing the radius at which the transition between elastoplastic and rigid plastic occurs. However, the problem with the mixed model is that a discontinuity occurs in the equivalent plastic strain increment at the transition between the two parts of the model. The reason for this is that the contribution of the elastic strain is neglected in the rigid plastic part of the model. The discontinuity in equivalent plastic strain increment potentially results in a discontinuity in the stress when hardening or strain rate dependent behaviour is modelled. This may lead to convergence problems in the global equilibrium iterations.

2.7   Concluding remarks

In this paper a class of adaptive return mapping algorithms is proposed, in which the weights of the time integration are a function of the plastic multiplier. The algorithm is applicable to both rate independent and rate dependent flow. It is shown that for the incremental algorithm, there is no fundamental difference between rate dependent and rate independent plasticity.

For large values of the plastic multiplier (i.e. large plastic increments) an obvious candidate function for α is presented which approaches the exact solution much faster then the commonly used radial return method. For small values of the plastic multiplier, several candidate functions for α are investigated. The accuracy of the proposed models was illustrated with iso-error maps. It is shown with these maps that some of the adaptive algorithms improve the accuracy of the return mapping considerably. The proposed method shows a similarity to the rigid plastic and the mixed elastoplastic / rigid plastic model but it does not neglect the elastic contribution to the strain and it does not show the bad accuracy of the rigid plastic model in the case of small strain increments.

References

[1] M. Ortiz and E. P. Popov. Accuracy and stability of integration algorithms for elastoplastic constitutive relations. *Int. J. Numer. Meth. Engng.*, 21:1561–1576, 1985.

[2] M. L. Wilkins. Calculation of elastic-plastic flow. In B. Alder et al., editor, *Methods of Computational Physics*, volume 3, New York, 1964. Academic Press.

[3] R. D. Krieg and D. B. Krieg. Accuracies of numerical solution methods for the elastic-perfectly plastic model. *J. Pressure Vessel Tech.*, 99:510–515, 1977.

[4] J. C. Nagtegaal. On the implementation of inelastic constitutive equations with special reference to large deformation problems. *Comput. Methods Appl. Mech. Engrg.*, 33:469–484, 1982.

[5] J. R. Rice and D. M. Tracy. Computational fracture mechanics. In S. J. Fenves, editor, *Proc. Symp. Numer. Meth. Struct. Mech.*, page 585, New York, 1973. Academic Press.

[6] M. Ortiz, P. M. Pinsky, and R. L. Taylor. Operator split methods for the numerical solution of the elastoplastic dynamic problem. *Comput. Methods Appl. Mech. Engrg.*, 39:137–157, 1983.

[7] J. C. Simo and M. Ortiz. A unified approach to finite deformation elastoplastic analysis based on the use of hyper-elastic constitutive equations. *Comput. Methods Appl. Mech. Engrg.*, 49:221–245, 1984.

[8] M. Ortiz and J. C. Simo. An analysis of a new class of integration algorithms for elastoplastic constitutive relations. *Int. J. Numer. Meth. Engng.*, 21:1561–1576, 1989.

[9] J. W. Wissman and C. Hauck. Efficient elasto-plastic finite element analysis with higher order stress-point algorithms. *Computers & Structures*, 17:89–95, 17.

[10] S. W. Sloan. Substepping schemes for numerical integration of elasto-plastic stress-strain relations. *Int. J. Numer. Meth. Engng.*, 24:893–911, 1987.

[11] D. M. Potts and D. Ganendra. An evaluation of substepping and implicit stress point algorithms. *Comput. Methods Appl. Mech. Engrg.*, 119:341–354, 1994.

[12] J. Huétink, A. H. van den Boogaard, A. D. Rietman, J. Lof, and T. Meinders. A mixed elastoplastic / rigid-plastic material model. *Int. J. Numer. Meth. Engng.*, 46:1421–1434, 1999.

[13] P. Perzyna. Fundamental problems in viscoplasticity. In *Recent Advances in Applied Mechanics*, volume 9, pages 243–377, New York, 1966. Acedemic Press.

[14] J. C. Simo, J. G. Kennedy, and S. Govindjee. Non-smooth multisurface plasticity and visco-plasticity - loading/unloading conditions and numerical algorithms. *Int. J. Numer. Meth. Engng.*, 26:2161–2185, 1988.

[15] J. C. Simo and T. J. R. Hughes. *Computational Inelasticity*. Springer-Verlag, New York, 1998.

[16] W. M. Wang, L. J. Sluys, and R. de Borst. Viscoplasticity for instabilities due to strain softening and strain-rate softening. *Int. J. Numer. Meth. Engng.*, 40:3839–3864, 1997.

[17] B. E. Healy and R. H. Dodds Jr. A large strain plasticity model for implicit finite element analysis. *Computational Mechanics*, 9:95–112, 1992.

[18] F. Auricchio and R. L. Taylor. A generalized visco-plasticity model and its algorithmic implementation. *Computers & Structures*, 53:637–647, 1994.

[19] M. Ortiz and J.C. Simo. An analysis of a new class of integration algorithms for elastoplastic constitutive relations. *Int. J. Numer. Meth. Engng.*, 23:353–366, 1986.

[20] H. J. Frost and M. F. Ashby. *Deformation-mechanism maps*, chapter 1, page 13. Pergamon press, 1982.

Appendix A - Iterative stress update

If the material is in the plastic state, the stress and plastic strain are determined by solving (2.19, 2.20). This can be done by eliminating the deviatoric stress $\mathbf{s}_{n+1}$ from (2.20) which leaves a scalar expression $g(\Delta\lambda) = 0$. This can be solved iteratively by several methods. Very efficient in this case is the secant method because it does not require the derivative of g with respect to $\Delta\lambda$. Also a Newton-Raphson method can be used:

$$\Delta\lambda^{i+1} = \Delta\lambda^i - \frac{g^i}{\frac{\mathrm{d}g}{\mathrm{d}\Delta\lambda}^i} \tag{2.32}$$

For the sake of completeness the derivative in the above expression is derived below.

$$\frac{\mathrm{d}g}{\mathrm{d}\Delta\lambda} = \frac{\partial g}{\partial \mathbf{s}_{n+1}}\frac{\mathrm{d}\mathbf{s}_{n+1}}{\mathrm{d}\Delta\lambda} + \frac{\partial g}{\partial \kappa}\frac{\mathrm{d}\kappa_{n+1}}{\mathrm{d}\Delta\lambda} + \frac{\partial g}{\partial \dot{\kappa}}\frac{\mathrm{d}\dot{\kappa}_{n+1}}{\mathrm{d}\Delta\lambda} \tag{2.33}$$

$$\frac{\partial g}{\partial \mathbf{s}_{n+1}} = \frac{\frac{3}{2}\mathbf{s}_{n+1}}{\sqrt{\frac{3}{2}\mathbf{s}_{n+1} : \mathbf{s}_{n+1}}} \tag{2.34}$$

$$\frac{\partial g}{\partial \kappa} = -\frac{\mathrm{d}\sigma_f}{\mathrm{d}\kappa} \tag{2.35}$$

$$\frac{\partial g}{\partial \dot{\kappa}} = -\frac{\mathrm{d}\sigma_f}{\mathrm{d}\dot{\kappa}} \tag{2.36}$$

$$\frac{\mathrm{d}\mathbf{s}_{n+1}}{\mathrm{d}\Delta\lambda} = -\frac{2G(\mathbf{s}_n + 2G\alpha\Delta\mathbf{e})}{(1 + 2G\Delta\lambda\alpha)^2} + \frac{4G^2\Delta\lambda(\Delta\lambda\mathbf{s}_n - \Delta\mathbf{e})}{(1 + 2G\Delta\lambda\alpha)^2}\frac{\mathrm{d}\alpha}{\mathrm{d}\Delta\lambda} \tag{2.37}$$

$$\frac{\mathrm{d}\kappa}{\mathrm{d}\Delta\lambda} = \frac{2}{3}\sqrt{\frac{3}{2}\mathbf{s}^*\colon\mathbf{s}^*}$$
$$+ \Delta\lambda\frac{\alpha\mathbf{s}_{n+1}\colon\mathbf{s}_{n+1} + (1-2\alpha)\,\mathbf{s}_n\colon\mathbf{s}_{n+1} - (1-\alpha)\,\mathbf{s}_n\colon\mathbf{s}_n}{\sqrt{\frac{3}{2}\mathbf{s}^*\colon\mathbf{s}^*}}\frac{\mathrm{d}\alpha}{\mathrm{d}\Delta\lambda}$$
$$+ \alpha\Delta\lambda\frac{(1-\alpha)\,\mathbf{s}_n + \alpha\mathbf{s}_{n+1}}{\sqrt{\frac{3}{2}\mathbf{s}^*\colon\mathbf{s}^*}}\frac{\mathrm{d}\mathbf{s}_{n+1}}{\mathrm{d}\Delta\lambda} \tag{2.38}$$

$$\frac{\mathrm{d}\dot{\kappa}}{\mathrm{d}\Delta\lambda} = \frac{1}{\Delta t}\frac{\mathrm{d}\kappa}{\mathrm{d}\Delta\lambda} \tag{2.39}$$

Appendix B - Consistent tangent matrix

Obtaining an efficient global iteration process requires the derivation of the consistent tangent matrix. The consistent tangent follows from the linearisation of the stress update algorithm (2.19, 2.20):

$$\mathrm{d}\mathbf{e} = \left(\frac{1 + 2G\Delta\lambda\alpha}{2G}\right)\mathbf{I}^4\colon\mathrm{d}\mathbf{s}$$
$$+ \left(\left(\alpha + \Delta\lambda\frac{\mathrm{d}\alpha}{\mathrm{d}\lambda}\right)\mathbf{s}_{n+1} - \left((1-\alpha) - \Delta\lambda\frac{\mathrm{d}\alpha}{\mathrm{d}\lambda}\right)\mathbf{s}_n\right)\mathrm{d}\lambda \tag{2.40}$$

$$\mathrm{d}g = \left(\frac{\frac{3}{2}\mathbf{s}_{n+1}}{\sqrt{\frac{3}{2}\mathbf{s}_{n+1}\colon\mathbf{s}_{n+1}}} - h\frac{\Delta\lambda\alpha\mathbf{s}^*}{\sqrt{\frac{3}{2}\mathbf{s}^*\colon\mathbf{s}^*}}\right)\colon\mathrm{d}\mathbf{s}$$
$$- \left(h\left(\sqrt{\frac{2}{3}\mathbf{s}^*\colon\mathbf{s}^*} + \frac{\Delta\lambda\mathbf{s}^*\colon(\mathbf{s}_{n+1}-\mathbf{s}_n)}{\sqrt{\frac{3}{2}\mathbf{s}^*\colon\mathbf{s}^*}}\frac{\mathrm{d}\alpha}{\mathrm{d}\lambda}\right)\right)\mathrm{d}\lambda = 0 \tag{2.41}$$

With $\mathbf{I}^4$ the fourth order unity tensor and the viscoplastic modulus h defined as:

$$h = \frac{\partial\sigma_f}{\partial\Delta\kappa} = \frac{\partial\sigma_f}{\partial\kappa} + \frac{1}{\Delta t}\frac{\partial\sigma_f}{\partial\dot{\kappa}} \tag{2.42}$$

Eliminating $\mathrm{d}\lambda$ from these equations results in the following expression for the deviatoric part of the tangent modulus:

$$\mathrm{d}\mathbf{s} = \left[\mathbf{D} + \frac{\mathbf{D}\colon\mathbf{uv}\colon\mathbf{D}}{A - \mathbf{v}\colon\mathbf{D}\colon\mathbf{u}}\right]\colon\mathrm{d}\varepsilon \tag{2.43}$$

With:

$$\mathbf{D} = \left(\frac{2G}{1 + 2G\Delta\lambda\alpha}\right)\mathbf{I}^4 \tag{2.44}$$

$$\mathbf{u} = \left(\left(\alpha + \Delta\lambda \frac{\mathrm{d}\alpha}{\mathrm{d}\lambda} \right) \mathbf{s}_{n+1} - \left((1 - \alpha) - \Delta\lambda \frac{\mathrm{d}\alpha}{\mathrm{d}\lambda} \right) \mathbf{s}_n \right) \tag{2.45}$$

$$\mathbf{v} = \left(\frac{\frac{3}{2}\mathbf{s}}{\sqrt{\frac{3}{2}\mathbf{s}_{n+1} : \mathbf{s}_{n+1}}} - h \frac{\Delta\lambda\alpha\mathbf{s}^*}{\sqrt{\frac{3}{2}\mathbf{s}^* : \mathbf{s}^*}} \right) \tag{2.46}$$

$$A = -\left(h \left(\sqrt{\frac{2}{3}\mathbf{s}^* : \mathbf{s}^*} + \frac{\Delta\lambda\mathbf{s}^* : (\mathbf{s}_{n+1} - \mathbf{s}_n)}{\sqrt{\frac{3}{2}\mathbf{s}^* : \mathbf{s}^*}} \frac{\mathrm{d}\alpha}{\mathrm{d}\lambda} \right) \right) \tag{2.47}$$

Chapter 3

Elasto-viscoplastic FEM simulations of the aluminium flow in the bearing area for extrusion of thin-walled sections

J. Lof

Abstract

The use of the Finite Element Method (FEM) is becoming increasingly important in the understanding of processes that occur during aluminium extrusion. The bearing area is one of the most difficult areas to model in a numerical simulation. To investigate the phenomena that occur in the bearing, detailed 2D simulations of the aluminium flow are presented in this paper. In the simulations the effects of material behaviour, friction coefficient, bearing length and bearing angle are investigated. It is demonstrated that elastic effects play an important role when the aluminium flows through the bearing channel. To accurately model this effect an elasto-viscoplastic constitutive model is necessary. It is observed that the resistance in a parallel bearing can be very sensitive to small changes in bearing geometry. This can explain the unpredictable behaviour of extrusion dies observed in practise. A design approach is suggested that reduces the sensitivity of the bearing.

3.1 Introduction

Aluminium extrusion is a forming process used to produce profiles. A large variety of profiles can be made by pressing a billet of hot aluminium through a hole that closely resembles the required cross-section of the profile. To obtain an acceptable product it is important that the exit velocity of the profile is uniform over the entire cross-section. Expected differences in exit velocity are compensated for by locally adjusting the bearing geometry to increase or decrease the resistance in the bearing channel. Currently this is often done by trial and error.

In the design of extrusion dies, it is a major challenge to get the dies right first time. To do this, the processes that occur inside the die must be understood. It is very difficult to perform measurements inside a die, therefore numerical simulations are necessary to gain more insight into the extrusion process. A widely used method to simulate forming processes is the Finite Element Method (FEM), which can also be applied to extrusion.

In the past, numerical simulations of extrusion have been limited to relatively simple geometries and low extrusion ratios, because of computational restrictions [1, 2]. Recently attention has shifted to extrusion of more complex thin-walled sections [3, 4, 5]. For the simulation of extrusion of thin-walled sections, accurate modelling of the bearing and the area just in front of the bearing constitutes a major challenge. In this area, high deformations and deformation gradients occur. In addition, somewhere in or just in front of the bearing a transition between sticking and slipping friction occurs [6]. To better understand the processes that occur in the bearing area, a detailed 2D model is developed. With this model the effects of bearing geometry, material behaviour and friction coefficient are investigated. The results of this model can also be used to construct a less detailed model that can be used in simulations of the entire process, this aspect is described in other publications [7, 8, 9].

When modelling the extrusion process with a FEM code, it is common to use a viscoplastic constitutive model. This kind of model neglects the elastic behaviour of the material. However when the material enters the bearing channel, plastic deformations are minimal and elastic effects have a significant influence on the material behaviour. To investigate the influence of these elastic effects in the bearing area, simulations are performed with and without taking into account the elastic effects. In Section 3.2 this is discussed in more detail. In Section 3.3, the numerical model of the bearing area is discussed. In Section 3.4 the results of the simulations are presented. The practical implications of these results are discussed in Section 3.5.

3.2 Material modelling

Hot aluminium has a rate dependent or viscoplastic behaviour. In the first part of this section constitutive equations that can be used to model hot aluminium are derived. These equations relate the Cauchy stress tensor $\boldsymbol{\sigma}$ to the strain increment $\Delta\boldsymbol{\varepsilon}$. Firstly, a viscoplastic model is derived. In this model, the elastic contribution is neglected. Secondly, an elasto-viscoplastic model is derived, which includes elastic effects.

In simulations of extrusion it is common to use a viscoplastic model and neglect the elasticity of the material. The reason for this is that the elastic deformations are small compared to the very large plastic deformations that occur during the process. However, in some areas of the process the elasticity is of interest. Especially inside the bearing channel the deformations of the material are very small and elastic effects are dominant. The processes which occur inside and just in front of the bearing, to a large extent determine the local exit velocity of the profile and the extrusion pressure. Therefore it is important to have an accurate model of the bearing area which incorporates elastic effects.

Since large deformations occur just in front of the bearing, the constitutive model should be applicable to large deformation analysis. Objective integration is obtained by using a corotational formulation [10]. For simplicity, the constitutive model is derived for infinitesimal deformations only.

3.2.1 Time continuous constitutive equations

To begin with, a set of constitutive equations is given used to characterize elasto-viscoplastic materials. The Von Mises criterion is used to define the effective stress $\overline{\sigma}$ (J_2 flow). The equations are presented in rate form, with a superposed dot denoting a derivative with respect to time.

$$\dot{\boldsymbol{\varepsilon}} = \dot{\boldsymbol{\varepsilon}}^e + \dot{\boldsymbol{\varepsilon}}^{vp} \tag{3.1}$$

$$\dot{\boldsymbol{\sigma}} = \mathbf{E} : \left(\dot{\boldsymbol{\varepsilon}} - \dot{\boldsymbol{\varepsilon}}^{vp} \right) \tag{3.2}$$

$$\dot{\boldsymbol{\varepsilon}}^{vp} = \dot{\lambda}\mathbf{s} \tag{3.3}$$

$$g\left(\boldsymbol{\sigma}, \kappa, \dot{\kappa}\right) = \overline{\sigma} - \sigma_f\left(\kappa, \dot{\kappa}\right) \tag{3.4}$$

$$\dot{\lambda} \geq 0 \ , \quad \dot{\lambda}g = 0 \ , \quad g \leq 0 \tag{3.5}$$

- Equation 3.1 is the rate form of the strain decomposition. The total strain ε is assumed to be the sum of an elastic part ε^e and viscoplastic part ε^{vp}.

- Equation 3.2 is the linear elastic relation between the Cauchy stress $\boldsymbol{\sigma}$ and the elastic strain in rate form. The elastic modulus $\mathbf{E}$ is a 4th order tensor based on the scalar values of the Young's modulus E and Poisson's ratio ν.

- Equation 3.3 is the evolution law (flow rule) for the viscoplastic strain rate. Extending the notion of associative plasticity to viscoplasticity, the viscoplastic strain is assumed to be in the direction of the deviatoric stress. The viscoplastic multiplier $\dot{\lambda}$ is used to scale the viscoplastic strain rate. The deviatoric stress $\mathbf{s}$ is defined by:

$$\boldsymbol{\sigma} = \mathbf{s} - p\mathbf{I}\,, \quad p = -\tfrac{1}{3}\mathrm{tr}\left(\boldsymbol{\sigma}\right) \tag{3.6}$$

- Equation 3.4 gives the limit function. This function describes the rate dependent behaviour of the material in the plastic domain. It can be interpreted as a generalisation of the Von Mises yield function from rate independent plasticity to rate dependent plasticity. The Von Mises stress is given by:

$$\overline{\sigma} = \sqrt{\tfrac{3}{2}\mathbf{s} : \mathbf{s}} \tag{3.7}$$

The flow stress σ_f is a function of the state variables κ and $\dot{\kappa}$, respectively the equivalent viscoplastic strain and equivalent viscoplastic strain rate. They are defined by:

$$\dot{\kappa} = \sqrt{\tfrac{2}{3}\dot{\varepsilon}^{vp} : \dot{\varepsilon}^{vp}} \tag{3.8}$$

- Equations 3.5 are the Kuhn-Tucker loading-unloading conditions. The material can be in two states. Firstly the elastic state for which the plastic multiplier $\dot{\lambda}$ is equal to zero and the limit function is lower or equal to zero. Secondly the plastic state, for which the plastic multiplier is larger than zero and the limit function is equal to zero. On the boundary between these two states, the viscoplastic strain rate and the limit function are equal to zero. At this boundary, the limit function corresponds to the yield function used in rate independent plasticity.

3.2.2 Viscoplastic constitutive equations

The model presented in this subsection is based on the assumption that the plastic strain increment is much larger than the elastic increment. Therefore the elastic part

can be neglected. The plastic strain increment now equals the total strain increment. Plastic incompressibility is enforced by an augmented penalty method. This augmentation requires an incremental procedure. To obtain this the time continuous model is integrated over a time increment $[t_n, t_{n+1}]$ with a Euler backward algorithm. The total strain increment is split into a deviatoric part and a volumetric part:

$$\Delta \varepsilon = \Delta \mathbf{e} + \Delta \varepsilon^{vol} \mathbf{I} \tag{3.9}$$

With the assumption that the deviatoric strain equals the plastic strain, (3.2-3.5) can be written as:

$$\Delta \mathbf{e} = \Delta \lambda \mathbf{s}_{n+1} \tag{3.10}$$

$$g_{n+1} = 0 \tag{3.11}$$

The deviatoric stress follows directly from (3.10), with the viscoplastic multiplier $\Delta \lambda$ eliminated by enforcing (3.11):

$$\mathbf{s}_{n+1} = \tfrac{2}{3} \sigma_f \left(\kappa_{n+1}, \dot{\kappa}_{n+1} \right) \frac{\Delta \mathbf{e}}{\Delta e_q} \tag{3.12}$$

Here Δe_q is the equivalent strain given by:

$$\Delta e_q = \sqrt{\tfrac{2}{3} \Delta \mathbf{e} \colon \Delta \mathbf{e}} \tag{3.13}$$

The hydrostatic part of the stress tensor is determined by the plastic incompressibility condition. An augmented penalty method is used to enforce this condition:

$$p_{n+1} = p_n - C_b \Delta \varepsilon^{vol} \tag{3.14}$$

Where C_b is the bulk modulus. An advantage of this augmented penalty method is that no extremely high penalty factor is required to avoid loss of material. With this formulation it is possible to use an elastic compressibility for the volumetric strain when using an elastic bulk modulus. Nearly incompressible behaviour is obtained by setting the bulk modulus to a very high value.

Combining the deviatoric and hydrostatic part, the following relation between stress and strain increment is obtained:

$$\boldsymbol{\sigma}_{n+1} = \tfrac{2}{3} \sigma_f \left(\kappa_{n+1}, \dot{\kappa}_{n+1} \right) \frac{\Delta \mathbf{e}}{\Delta e_q} + \left(C_b \text{tr} \left(\Delta \varepsilon \right) - p_n \right) \mathbf{I} \tag{3.15}$$

The state variables κ and $\dot{\kappa}$ are estimated from the equivalent strain increment:

$$\kappa_{n+1} = \kappa_n + \Delta e_q \tag{3.16}$$

$$\dot{\kappa}_{n+1} = \frac{\Delta e_q}{\Delta t} \tag{3.17}$$

The viscoplastic model is very suitable for calculations where large plastic deformations occur. However, in most processes there are also areas with very little or no plastic deformation. In these areas the equivalent strain increment will be equal or almost equal to zero. This will cause (3.15) to become singular. This problem can be solved by giving the equivalent strain increment a small minimum value. The resulting stresses and strains in these areas will not be correct. An indication of the error that occurs is given in [11]. Often the results in areas with no plastic deformation are of little interest and a viscoplastic model is sufficient to obtain the desired results.

3.2.3 Elasto-viscoplastic constitutive equations

In an elasto-viscoplastic model the viscoplastic strain increment does not follow directly from the total strain increment. To obtain an expression for the viscoplastic strain increment the evolution law (3.3) has to be integrated over the time interval $[t_n, t_{n+1}]$. Using a Euler backward (radial return) integration algorithm, this results in the following set of equations:

$$\Delta \varepsilon = \Delta \varepsilon^e + \Delta \varepsilon^{vp} \tag{3.18}$$

$$\Delta \boldsymbol{\sigma}_{n+1} = \mathbf{E} : \left(\Delta \varepsilon - \Delta \varepsilon^{vp} \right) \tag{3.19}$$

$$\Delta \varepsilon^{vp} = \Delta \lambda \mathbf{s}_{n+1} \tag{3.20}$$

$$g_{n+1} = \overline{\sigma}_{n+1} - \sigma_f \left(\kappa_{n+1}, \dot{\kappa}_{n+1} \right) \tag{3.21}$$

$$\Delta \lambda \geq 0 \ , \quad \Delta \lambda g_{n+1} = 0 \ , \quad g_{n+1} \leq 0 \tag{3.22}$$

Table 3.1: Constitutive parameters for AA6063 alloy.

parameter		min	used	max
elastic properties:	E (MPa)		40000	
($T = 773$ K)	ν		0.35	
plastic properties:	$\dot{\kappa}_0$ (1/s)	0.001	0.005	0.01
	s_m (MPa)	25	25	76
	m	2.4	5.4	6.0
	A (1/s)	10^9	$6 \cdot 10^9$	10^{12}
	Q (J/mol)	$1.3 \cdot 10^5$	$1.4 \cdot 10^5$	$1.8 \cdot 10^5$
	R (J/molK)		8.314	

The state variables are defined as:

$$\kappa_{n+1} = \kappa_n + \sqrt{\tfrac{2}{3}\Delta\varepsilon^{vp} : \Delta\varepsilon^{vp}} \qquad (3.23)$$

$$\dot{\kappa}_{n+1} = \frac{\sqrt{\tfrac{2}{3}\Delta\varepsilon^{vp} : \Delta\varepsilon^{vp}}}{\Delta t} \qquad (3.24)$$

The viscoplastic multiplier $\Delta\lambda$ can be eliminated by enforcing the Kuhn-Tucker conditions (3.22). In the elastic domain, the stresses can be calculated directly from the total strain increment with (3.19). In the plastic domain the stresses are calculated by solving $g_{n+1} = 0$.

3.2.4 Flow stress for aluminium alloys at elevated temperature

The actual behaviour of a specific aluminium alloy in the plastic domain is defined by an expression for the flow stress. This describes the relation between the effective stress, the equivalent viscoplastic strain and equivalent viscoplastic strain rate. In this paper, the Sellars-Tegart law [12] is used to model the behaviour of the aluminium alloy:

$$\sigma_f\left(\dot{\kappa}\right) = s_m \operatorname{arcsinh}\left(\left(\frac{\dot{\kappa}}{A}\exp\left(\frac{Q}{RT}\right)\right)^{\frac{1}{m}}\right) \qquad (3.25)$$

It can be easily seen that for $\dot{\kappa} = 0$ the flow stress is zero. Hence no elastic behaviour can be modelled with this material law. However, from the literature it is known that
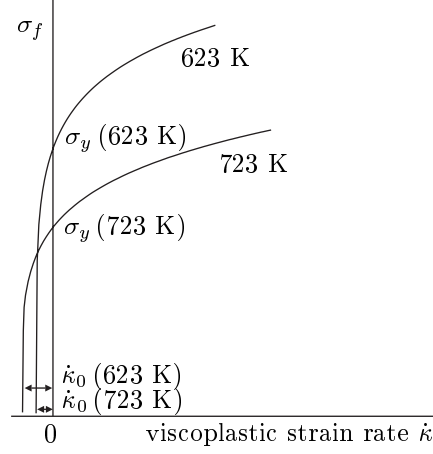
Figure 3.1: Influence of parameter $\dot{\kappa}_0$ on the flow stress.

even at elevated temperatures (673 K - 873 K) a small elastic region is present [13, 14]. To include such an elastic region a modified Sellars-Tegart law is introduced:

$$\sigma_f \left(\dot{\kappa}, T \right) = s_m \text{arcsinh} \left(\left(\frac{\dot{\kappa} + \dot{\kappa}_0 \left(T \right)}{A} \exp \left(\frac{Q}{RT} \right) \right)^{\frac{1}{m}} \right) \tag{3.26}$$

A temperature dependent parameter $\dot{\kappa}_0 \left(T \right)$ is added. In Figure 3.1 the influence of this parameter on the flow stress is shown. Normally a small value of $\dot{\kappa}_0$ between 0.01 and 0.001 is sufficient to obtain a realistic size of the elastic region.

Most experimental data obtained for specific aluminium alloys aims at describing the flow stress as a function of the strain rate and sometimes the strain. Not much attention is paid to the yield stress at high temperatures. In the simulations presented in this paper the modified Sellars-Tegart law is used to describe the material behaviour. The parameters for this model are fitted to data obtained experimentally for an AA6063 aluminium alloy. They are based on unpublished work done at Kings College (London). Other experimental data for the AA6063 alloy is published by Akeret [15] or more recently by Langkruis [16]. In Table 3.1 an overview is given of the parameter ranges found for this alloy.

Large differences can be observed between the different experimental data. A number of reasons can be suggested to account for these differences. Firstly, different testing methods are used to determine the parameters, namely torsion tests compared to compression tests. Secondly, small variations in alloy composition are possible

42
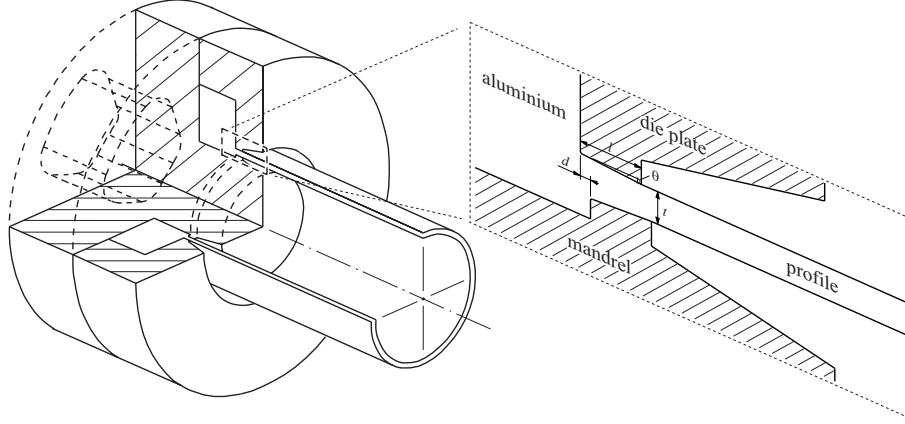
Figure 3.2: Bearing geometry for tube extrusion.

within the AA6063 norm. In addition to this, with the same composition, different material behaviour can occur because of variations in the solution state of the alloy components [17]. Taking all this into consideration, it can be concluded that it is very difficult to obtain reliable data for specific aluminium alloys.

3.3 Numerical modelling of the bearing area

To simulate the extrusion process an Arbitrary Lagrangian Eulerian (ALE) code, DiekA, was used. This code was developed during the last fifteen years by Huétink *et al.* [18, 19]. In the ALE method the mesh displacement can be controlled independently from the material displacement. The method was first developed in fluid mechanics to model fluid-structure interaction and to model the motion of free surfaces [20, 21]. Later it was introduced to solid mechanics where it is used to avoid mesh distortion which occurs when modelling large deformations with a Lagrangian description. In the bearing area of the extrusion process, very large deformations occur. These can be modelled well with an ALE method.

Extrusion is not a stationary process, because of the cyclic loading of the billet. The result is that the temperature in the bearing area varies during the process. Modelling these changes would require a transient calculation of at least one extrusion cycle. This is beyond the scope of this work. To study the processes in the bearing only a stationary isothermal solution is investigated.
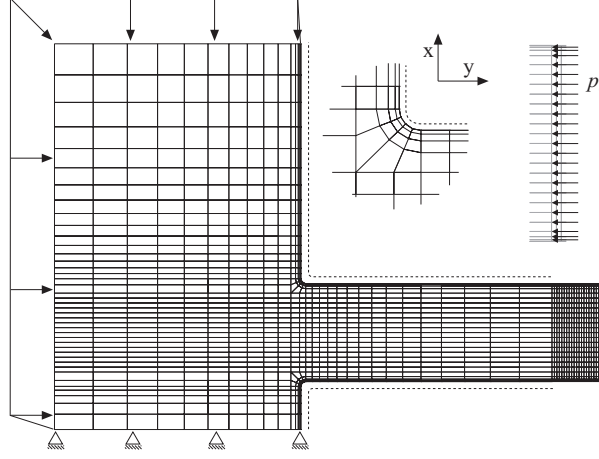
Figure 3.3: FEM mesh for the bearing area.

3.3.1 FEM model for the bearing area

An extrusion die used for the extrusion of tubes is illustrated in Figure 3.2. In this figure also a detailed view of the bearing is presented. The geometry of the bearing shown in the detailed view is used for the numerical model. The diameter of the extruded tube is 80 mm and the wall thickness is about 2 mm. Some specific bearing dimensions like the bearing length l and angle θ will be varied. A simple pre-processor was developed to automatically generate a FEM mesh based on the desired dimensions of the bearing area. In Figure 3.3 this mesh is plotted. Axi-symmetrical 4-node elements are used to model the aluminium. A well-known problem with these elements is that they have extreme stiffness for incompressible plasticity. This is often referred to as volume-locking. Selective reduced integration, also known as the $\overline{B}$-approach [22, 23], is used to prevent this.

During the extrusion process the normal pressure on the interface between aluminium and die is so high that no slipping friction occurs. The aluminium sticks to the wall throughout almost the entire die. At some point in the bearing area the pressure decreases to the extent that the friction stresses become lower than the internal shear strength of the aluminium and the material will slip along the die surface. To model friction in the region where slip may occur contact elements are used (dotted boundary in Figure 3.3). These elements are based on a penalty formulation [24]. A Coulomb friction law is implemented in these elements. It is very difficult to determine the friction coefficient under extrusion conditions. Estimates in the literature vary between

Figure 3.4: Control of the mesh on free surfaces inside the bearing channel.

0.1 [4] to values above 1 [25]. The influence of this parameter on the resistance in the bearing is investigated. If no specific value of the friction coefficient is specified, a value $\mu = 0.5$ is used.
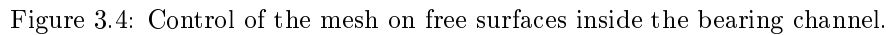
At the start of the simulation no normal stress is working at the wall inside the bearing channel. Because of this no friction will occur at this wall. To initiate friction a small pressure $p_c = 1.4$ MPa, counteracting the flow of the aluminium is applied at the exit of the bearing channel, as indicated in Figure 3.3. This pressure is applied for 1000 displacement increments and then removed. The next 9000 increments are performed without this pressure. At that time approximately 15 mm of profile is extruded and a stationary solution is obtained.

3.3.2 Controlling the mesh displacement

When a standard Updated Lagrangian method is used to control the mesh, extensive distortion of the mesh occurs after each increment. This would make it necessary to perform a re-meshing after each couple of increments. An alternative approach which is often used in simulations of extrusion is the Eulerian method. With this method the mesh is fixed at its location and the material flows through the mesh. No mesh distortion occurs but it is difficult to model the free surface of the profile after it leaves the bearing. With the ALE method it is possible to control the mesh displacement independently of the material displacement.

In the simulations presented in this paper, the mesh inside the die and bearing channel is fixed to its location, effectively a Eulerian method. To avoid material flowing out of the mesh at the free surfaces, a mixed Lagrangian Eulerian description is used. This is illustrated in Figure 3.4. The nodes move with the material for the displacement component normal to the surface. For the component parallel to the surface the nodes do not move with the material. This description is used on the free surfaces, but also
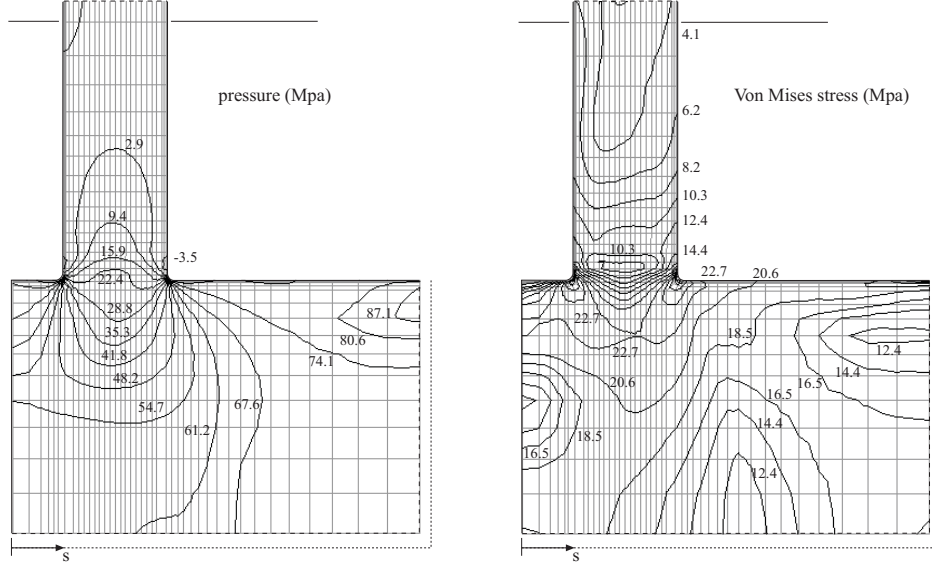
Figure 3.5: Pressure and Von Mises stress in the bearing area ($l = 5$ mm $\mu = 0.5$).

on the dotted boundaries indicated in Figure 3.3. This means that it is possible that the material loses contact with the wall in the bearing channel. This happens for instance when the bearing angle θ is negative (relieved bearing), but it also occurs under certain conditions in parallel bearings.

3.4 Results of the simulations

A large number of simulations were performed with the model discussed in the previous section. Simulations were carried out with both the viscoplastic and the elasto-viscoplastic model. The influence of the friction coefficient has been studied as well as the influence of the bearing length and the bearing angle.

In the first part of this section, some general results will be discussed. The simulations presented here are done with the elasto-viscoplastic model. In the second part of this section, a comparison is made between the viscoplastic and the elasto-viscoplastic models. It is shown that the elastic effects have a significant influence on the resistance of the material in the bearing channel. The results presented in the first two parts of this section are based on a parallel bearing channel. In the third part, the effect of changes in the bearing angle are discussed.

46

Table 3.2: Conversion of Von Mises stress to equivalent plastic strain rate according to (3.26).

Von Mises stress $\overline{\sigma}$ (MPa)	eq. plastic strain rate $\dot{\kappa}$ (1/s)
< 10.3	(elastic)
12.4	0.05
14.4	0.14
16.5	0.32
18.5	0.66
20.6	1.32
22.6	2.54
24.7	4.56
26.8	8.19
28.8	14.02
30.9	24.19

3.4.1 General results

To begin with, the results of a simulation with a parallel bearing ($\theta = 0$, $l = 5$ mm, $t = 2$ mm) are presented in Figure 3.5. This simulation was carried out using the elasto-viscoplastic model. The yield stress of the aluminium is approximately 10.3 MPa, so Von Mises stresses below this value indicate that the material is in the elastic domain. This is the case in almost the entire bearing channel. For values of the Von Mises stress above 10.3 MPa, the material is in the plastic domain. The Von Mises stress can be directly related to an equivalent plastic strain rate by the modified Sellars-Tegart law (3.26). The equivalent values are listed in Table 3.2.

To compare the results of different simulations, a measure for the resistance of the bearing must be defined. The average pressure on the inflow edge is taken as this measure. This average pressure P is calculated by integrating over the dotted area S, indicated in Figure 3.5:

$$P = \frac{1}{S} \int_s p \mathrm{d}s \tag{3.27}$$

In Figure 3.6 the influence of changes in the bearing length are plotted. As discussed in Section 3.3.1, a small pressure p_c is applied to the exit in the initial stage of the
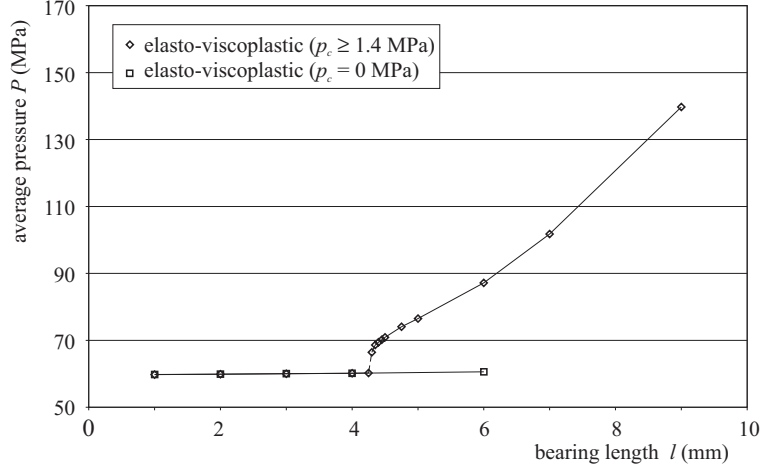
Figure 3.6: Influence of bearing length on the resistance in the bearing channel ($\mu = 0.5$).

simulation. This pressure is necessary to initiate contact between the aluminium and the wall of the bearing channel. After approximately 1.5 mm is extruded, this pressure is removed while the simulations is continued. To illustrate the effect of p_c, simulations are also performed without this pressure. The results of these simulations show that the bearing length has no effect on the resistance in the bearing channel, indicating that there is no contact between the bearing wall and the aluminium. In the case $p_c = 1.4$ MPa, there is a transition between two states. For short bearing lengths, there is no contact in the stationary solution of the simulation. For longer bearings, there is contact.

So at a certain bearing length a bifurcation occurs. For longer bearings, two stable solutions can be distinguished, one with and one without contact in the bearing. By applying an initial pressure, the simulation is forced to the solution with contact. Higher values of the pressure p_c will not change the results. For lower values of p_c the transition to a solution with contact may not occur or occur at a higher value of the bearing length.

For short bearing lengths, the solution with contact in the bearing is not stable and will eventually move to a situation without contact. This effect is explained in more detail with the help of Figure 3.7. Two zones (A and B) are indicated in this figure. In zone A stresses in the y-direction will be in tension (positive values). In this area the material has the tendency to lose contact with the bearing wall, because the material
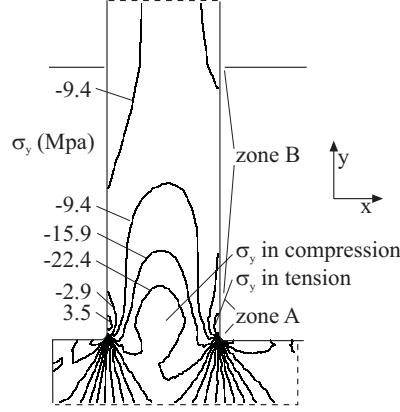
48

Figure 3.7: Contact in the bearing channel.

is stretched in the y-direction. This tendency is counteracted by the pressure that is built up inside the bearing channel by the friction forces at the wall (zone B). If these friction forces are sufficient, which is the case for long bearings, the contact will remain. If the forces are too low, contact will be lost at zone A and eventually along the entire bearing length.

3.4.2 Influence of elastic material behaviour

To investigate the difference between the viscoplastic and the elasto-viscoplastic material models, simulations with both models are made. In Figure 3.8 the results for simulations with different bearing lengths are shown. For the viscoplastic model, the transition to a solution with contact comes at a much higher value of the bearing length. The reason for this is that the pressure p_c is too low to accumulate sufficient resistance in the bearing to force the simulation to the solution with contact. If p_c is increased to 2.3 MPa, the transition occurs at a lower value of l.

For the solution without contact, an average pressure of approximately 60 MPa is calculated. This pressure is generated by the deformation that occurs before the material enters the bearing channel. The elasto-viscoplastic and the viscoplastic models show identical results for the solution without contact. The reason for this is that the plastic deformations are high in the area in front of the bearing channel. Elastic effects will have no significant influence in this area. When contact occurs, the resistance in the bearing channel is approximately 50% higher for the viscoplastic model
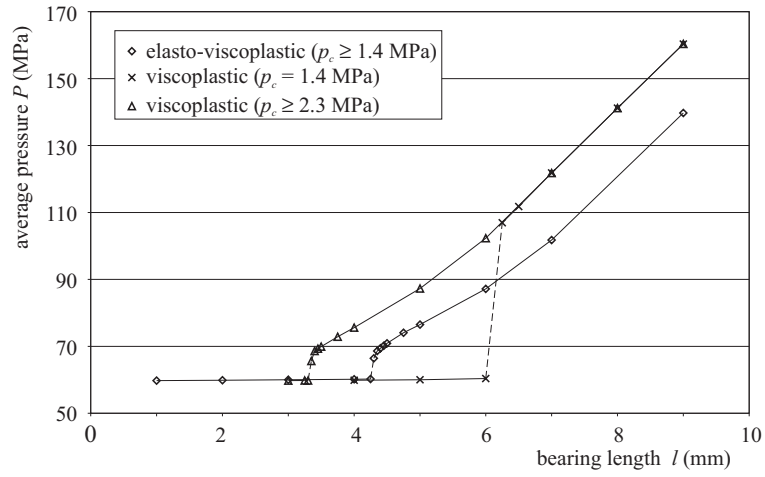
49

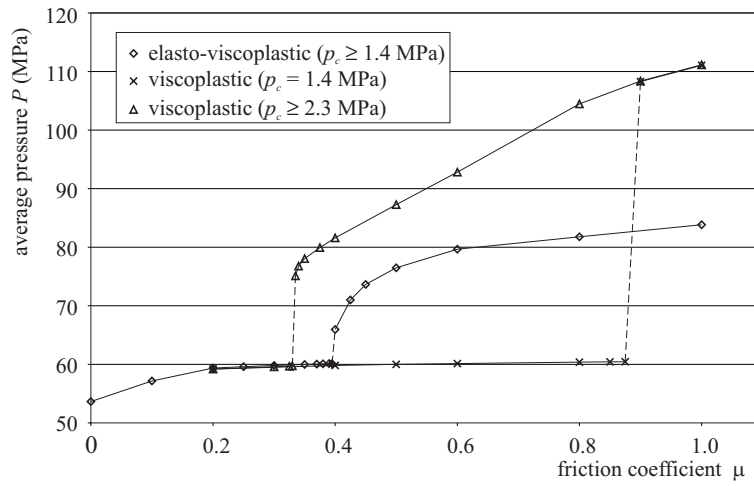Figure 3.8: Influence of bearing length on the resistance in the bearing channel ($\mu = 0.5$).

Figure 3.9: Influence of friction coefficient on the resistance in the bearing channel ($l = 5$ mm).
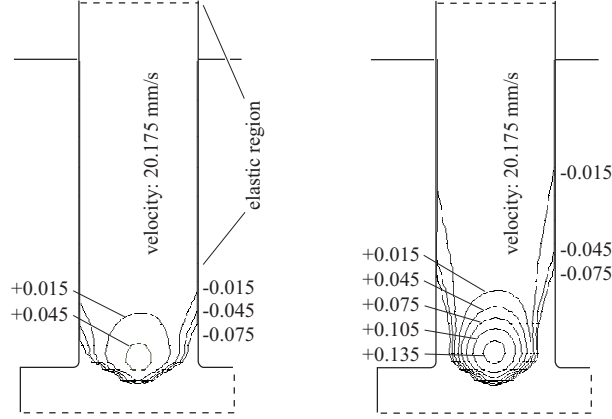
Figure 3.10: Velocity in the bearing channel: elasto-viscoplastic model (left), viscoplastic model (right). Mean velocity in the bearing channel is 20.175 mm/s. Only relative differences to this value are indicated.

compared to the elasto-viscoplastic model. This indicates that in the bearing channel, the elastic effects do have a significant influence.

In Figure 3.9 the influence of the friction coefficient on the resistance in the bearing is illustrated. The same behaviour as observed in Figure 3.8 is apparent. The viscoplastic simulations require a higher value of p_c to force the simulation in the solution with contact. For a higher friction coefficient, the bearing length at which the bifurcation occurs is reduced. The reason for this is that a higher friction coefficient increases the friction forces in zone B and thus the required bearing length to sustain a situation with contact is reduced.

To clearly demonstrate the difference between the elasto-viscoplastic and the viscoplastic models, the velocity of the material in the bearing channel is plotted in Figure 3.10. With the elasto-viscoplastic model, plastic deformation occurs only in the first part of the channel. In the rest of the channel the material is in the elastic domain. The simulation with the viscoplastic model shows a velocity gradient in the entire bearing channel. The material in the centre of the channel has a higher velocity than the material at the wall. Because this velocity difference decreases as the material moves through the bearing, material will flow from the centre to the wall. This will increase the normal stresses and hence the friction forces at the wall.

51
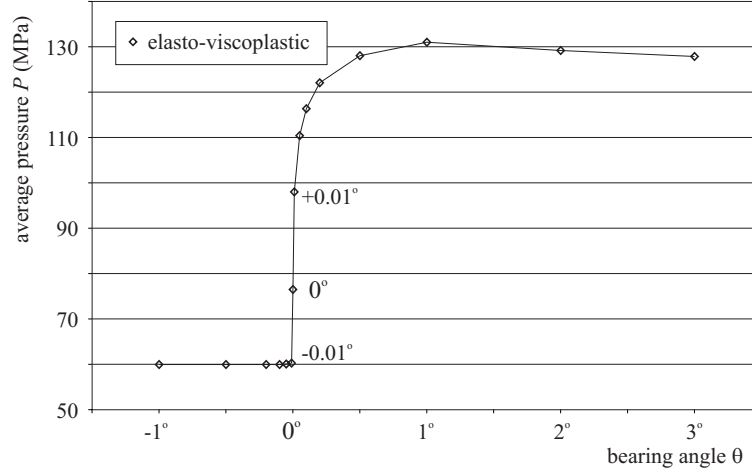
Figure 3.11: Influence of bearing angle on the resistance in the bearing channel ($l =$ 5 mm, $\mu = 0.5$).

3.4.3 Influence of the bearing angle

All previous simulations were carried out with a parallel bearing. However in practical situations, the bearing angle can be changed by deflections of the die. Sometimes the bearing angle is intentionally changed to increase or decrease the resistance in the bearing channel. The effect of the bearing angle on the average pressure P is illustrated in Figure 3.11.

For simulations with a non-parallel bearing, contact is either forced by a choked bearing ($\theta > 0$) or prevented by a relieved bearing ($\theta < 0$). The simulations predict a very large increase in pressure from -0.01°to +0.01°. In this range the solution jumps from a situation without contact to a situation with contact. It is apparent that the resistance of (almost) parallel bearings is very sensitive to small changes in the bearing angle. This trend can also be observed in experimental results by Akeret and Strehmel [26].

3.5 Discussion

In industrial extrusion of thin-walled sections, parallel bearings are often used. Expected differences in exit velocity of the profile are compensated for by varying the

52

Figure 3.12: Geometry of a relieved bearing with sink-in.

bearing length over the section. It is observed in practise that it is very difficult to accurately predict the bearing length in order to obtain a good profile. As a result, dies often do not produce the intended product. This is corrected by locally adjusting the bearing geometry to increase or decrease the resistance in the bearing channel by a trial and error process.

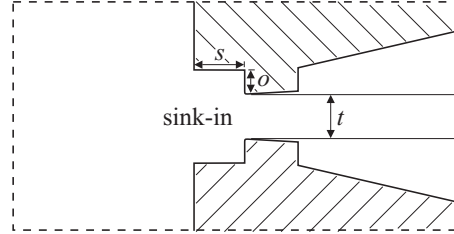The unpredictability observed in practise can be explained very well by the results of the simulations presented in this paper. From the results it is clear that for parallel bearings, changes in bearing length or angle can result in abrupt changes in resistance in the bearing channel. In practise additional factors have to be taken into account. Forces that are exerted on the profile (for example by a puller or by gravity) and effects of non-uniform velocity over the cross-section complicate the situation considerably. However the general trends observed in the simulation still apply. The use of parallel bearings is considered to be one of the most important factors contributing to the unpredictability of the extrusion process. To remove this factor from the extrusion process, either a choked or relieved bearing can be used. In both cases, the sensitivity of the resistance in the bearing channel to small changes in the bearing geometry is reduced significantly.

In the opinion of the author, a relieved bearing is to be preferred rather then a choked bearing since it greatly reduces the pressure necessary for the extrusion process. A problem with this approach is that in a relieved bearing, the bearing length can no longer be used to control the local velocity of the aluminium. In order to obtain a uniform exit velocity for the entire section, it is necessary to adjust the resistance locally. This can be done by adding a sink-in just in front of the bearing as illustrated in Figure 3.12. The depth s and the offset o of the sink-in can be used to control the exit velocity. This approach has been tested in an industrial setting with very encouraging results [27].

3.6 Conclusion

In the aluminium extrusion process, the bearing area has a dominant influence on the characteristics of the process. However, when making numerical simulations of the extrusion process it is also the most complex part of the simulation. To accurately predict the phenomena that occur in this area, a very detailed model is necessary. 2D simulations can give a basic understanding of the phenomena that occur in the bearing area.

A numerical model of the bearing area for the extrusion of a tube is presented in this paper. This model shows that there is hardly any plastic deformation in a parallel bearing channel. Because of this, elastic effects have a dominant influence on the bearing channel. This is demonstrated by comparing simulations with a viscoplastic model and an elasto-viscoplastic model.

The effects of changes in bearing geometry are also investigated in this paper. It is shown that for relatively short bearing lengths no contact occurs in the bearing channel. For longer bearing lengths, two stable solutions occur, one with and one without contact. By applying a force at the exit of the bearing, the solution can be forced to one of the solutions. In practice, forces exerted on the profile will determine whether or not contact occurs.

If the bearing angle is varied, the solution is either forced to contact (choked bearing) or prevented from contact (relieved bearing). With a parallel bearing, the solution can jump to either side. This makes the extrusion process very sensitive for variations in the bearing angle. To avoid this sensitive behaviour a design approach is suggested that uses a relieved bearing with a sink-in to control the local velocity of the material.

References

[1] G. Grasmo, K. Holthe, S. Støren, H. Valberg, R. Flatval, L. Hanssen, M. Lefstad, O. Lohne, T. Welo, R. Ørsund, and J. Herberg. Modelling of two-dimensional extrusion. In *Proc. 5th International Extrusion Technology Seminar*, pages 367–376, Wauconda, Illinois, 1992. Aluminum Association and Aluminum Extruders Council.

[2] Y. S. Kang and D. Y. Yang. Investigation into the thermo-viscoplastic finite element analysis of square die extrusion of square section with Lagrangian de-

scription. *Int. J. Mach. Tools Manufact.*, 36:907, 1996.

[3] L. Tong. *FE simulation of bulk forming processes with a mixed Eulerian-Lagrangian formulation.* PhD thesis, Swiss Federal Institute of Technology Zürich, Switserland, 1995.

[4] H. G. Mooi. *Finite element simulation of aluminium extrusion.* PhD thesis, University of Twente, The Netherlands, 1996.

[5] B. J. E. van Rens. *Finite element simulations of the aluminium extrusion process.* PhD thesis, Technical University Eindhoven, The Netherlands, 1999.

[6] H. Valberg and T. Malvik. An experimental investigation of the material flow inside the bearing channel in aluminium extrusion. *Int. J. of Materials and Product Technology*, 9:428–463, 1994.

[7] J. Lof, G. Klaseboer, J. Huétink, and P. T. G. Koenis. FEM simulations of aluminium extrusion using an elasto-viscoplastic material model. In *Proc. 7th International Extrusion Technology Seminar*, volume 2, pages 157–168, Wauconda, Illinois, 2000. Aluminum Association and Aluminum Extruders Council.

[8] J. Lof and J. Huétink. Isothermal elasto-viscoplastic FEM simulations of the extrusion of a thin aluminium tube. *Comp. Mater. Sci.*, 2000. submitted.

[9] J. Lof and Y. Blokhuis. FEM simulations of the extrusion of complex thin walled aluminium sections. *J. Mater. Proc. Tech.*, 2000. submitted.

[10] B. E. Healy and R. H. Dodds Jr. A large strain plasticity model for implicit finite element analysis. *Computational Mechanics*, 9:95–112, 1992.

[11] J. Lof and A. H. van den Boogaard. Adaptive return mapping algorithms for J_2 elasto-viscoplastic flow. *Int. J. Numer. Meth. Engng.*, 2000. submitted.

[12] H. J. Frost and M. F. Ashby. *Deformation-mechanism maps*, chapter 1, page 13. Pergamon press, 1982.

[13] D. Altenpohl. *Aluminium und aluminium legierungen.* Springer-Verlag, Berlin, 1965. (in German).

[14] L. F. Mondolfo. *Aluminium alloys: structures and properties.* Butterworth, London, 1976.

[15] R. Akeret, H. Jung, and G. Scharf. *Atlas of hot working properties of nonferrous metals*, volume 1. Deutsche Gesellschaft für Metallkunde (DMG), 1978.

[16] J. van de Langkruis, W. H. Kool, C. M. Sellars, M. R. van der Winden, and S. van der Zwaag. The effect of β,β' and β'' precipitates in a homogenised AA6063 alloy on the hot deformability and the peak hardness. *Mat. Sci. Eng. A*, 2000. accepted for publication.

[17] J. van de Langkruis, J. Lof, W. H. Kool, S. van der Zwaag, and J. Huétink. Comparison of experimental AA6063 extrusion trials to 3D numerical simulations, using a general solute-dependent constitutive model. *Comp. Mat. Sci.*, 2000. accepted for publication.

[18] J. Huétink. *On the simulation of thermomechanical forming processes*. PhD thesis, University of Twente, The Netherlands, 1986.

[19] J. Huétink, P. T. Vreede, and J. van der Lugt. Progress in mixed Eulerian-Lagrangian finite element simulation of forming processes. *Int. J. Numer. Meth. Engng.*, 30:1441–1457, 1990.

[20] A. Huerta and W. K. Liu. Viscous flow with large free surface motion. *Comput. Methods Appl. Mech. Engrg.*, 69:277–324, 1988.

[21] W. K. Liu, H. Chang, J. Chen, and T. Belytschko. Arbitrary Lagrangian-Eulerian Petrov-Galerkin finite elements for nonlinear continua. *Comput. Methods Appl. Mech. Engrg.*, 68:259–310, 1988.

[22] J. C. Nagtegaal, D. M. Parks, and J. R. Rice. On numerically accurate finite element solutions in the fully plastic range. *Comput. Methods Appl. Mech. Engrg.*, 4:113–135, 1974.

[23] T. J. R. Hughes. Generalization of selective reduced integration procedures to anisotropic and nonlinear media. *Int. J. Numer. Meth. Engng.*, 15:1413–1418, 1980.

[24] J. Huétink and P. T. Vreede. The simulation of contact problems in forming processes using a mixed Euler-Lagrangian finite element method. In E. G. Thompson, R. D. Wood, O. C. Zienkiewicz, and A. Samualsson, editors, *Numerical methods in forming processes*, pages 549–554, 1989.

[25] T. Björk, J. Bergström, and S. Hogmark. Tribological simulation of aluminium hot extrusion. *Wear*, 224:216–225, 1999.

[26] R. Akeret and W. Strehmel. Control of metal flow in extrusion dies. In *Proc. 4th International Extrusion Technology Seminar*, pages 357–367, Wauconda, Illinois, 1988. Aluminum Association and Aluminum Extruders Council.

[27] J. Lof, J. Huétink, and K.E. Nilsen. FEM simulations of the material flow in the bearing area of the aluminium extrusion process. In *Proc. 7th International Extrusion Technology Seminar*, volume 2, pages 211–222, Wauconda, Illinois, 2000. Aluminum Association and Aluminum Extruders Council.

Chapter 4

Comparison of experimental AA6063 extrusion trials to 3D numerical simulations, using a general solute-dependent constitutive model

J. van de Langkruis, J. Lof, W. H. Kool, S. van der Zwaag, J. Huétink

Abstract

In this paper laboratory scale extrusion experiments carried out on AA6063 billets are compared to numerical simulations. The numerical simulations are performed with a general solute-dependent elasto-viscoplastic constitutive model based on a hyperbolic sine law, allowing for the quantification of pressure levels, strain rate and stresses. The parameters for the material model were determined with compression tests. The extrusion trials were performed isothermally at temperatures of $623\,\mathrm{K}$ and $723\,\mathrm{K}$ and with two distinct material conditions. The results of the numerical simulations show good agreement with the experimental results. It turns out that local high strain rates ($> 40\,\mathrm{s}^{-1}$) have a significant influence on the extrusion pressure. However, adequate test methods to provide constitutive data at these strain rates are very limited. At high temperatures the difference between material conditions had a considerably smaller influence on the extrusion experiments compared to the simulations. It is argued that this effect can be attributed to dynamic precipitation that occurred during the experiments under high temperature, high strain rate conditions.

4.1 Introduction

Finite Element Modelling (FEM) represents a valuable tool for the optimisation of the aluminium extrusion processes. The numerical model should take into account the material conditions, and it should be able to model large deformations that occur during extrusion. It also should be able to model elastic deformations when predicting the frictional resistance in a parallel bearing channel or the stresses in the final profile. Furthermore, the model should accurately describe the flow resistance of the alloy during extrusion.

In FEM codes the flow resistance of the alloy is often described using a relatively simple and easy-to-use empirical constitutive equation , such as the hyperbolic sine law [1, 2, 3, 4] or the power law [1, 5, 6]. This law correlates local flow stress, equivalent plastic strain, strain rate and temperature. The parameters of these constitutive equations are often valid only for a given composition and limited experimental regime, and do not explicitly account for the metallurgical condition of the alloying elements in the aluminium alloy. However, in industrial extrusion billets, the condition of alloying elements depends on billet homogenisation and preheating practice, and changes dynamically during the extrusion process. These factors may significantly affect the extrusion pressure and mechanical properties of the extrudate. In previous work [2, 7] the hyperbolic sine law was adapted to describe solution hardening by accounting for the content of solute Mg and Si in the aluminium matrix. With this model, the effect of solute Mg and Si on the hot flow resistance during plane strain compression was modelled successfully.

In this paper a numerical analysis was made of a series of isothermal laboratory-scale extrusion trials of aluminium AA6063 billets with varying contents of solute Mg and Si. To this end the adapted hyperbolic sine law was implemented into the FEM code DiekA. This code is specialised in the simulation of forming processes like rolling, drawing, sheet metal forming and extrusion. The analysis comprised a quantification of absolute pressure levels, pressure drop along the length of the billet container, solute effects, flow stress and strain rate levels.

4.2 Constitutive model

In this section the constitutive elasto-viscoplastic model is presented, which was implemented into the FEM code. The Von Mises criterion was used to define the effective

stress. The equations are presented in an incremental formulation. This incremental formulation is obtained by integrating the constitutive equations in rate form over a time increment $[t_n, t_{n+1}]$ with an implicit Euler backward integration algorithm [8, 9], and results in:

$$\Delta \boldsymbol{\varepsilon} = \Delta \boldsymbol{\varepsilon}^e + \Delta \boldsymbol{\varepsilon}^{vp} \tag{4.1}$$

$$\Delta \boldsymbol{\sigma}_{n+1} = \mathbf{E} \colon \left(\Delta \boldsymbol{\varepsilon} - \Delta \boldsymbol{\varepsilon}^{vp} \right) \tag{4.2}$$

$$\Delta \boldsymbol{\varepsilon}^{vp} = \Delta \lambda \mathbf{s}_{n+1} \tag{4.3}$$

$$g_{n+1} \left(\boldsymbol{\sigma}_{n+1}, \kappa_{n+1}, \dot{\kappa}_{n+1} \right) = \overline{\sigma}_{n+1} - \sigma_f \left(\kappa_{n+1}, \dot{\kappa}_{n+1}, T \right) \tag{4.4}$$

$$\Delta \lambda \geq 0 \ , \quad \Delta \lambda g_{n+1} = 0 \ , \quad g_{n+1} \leq 0 \tag{4.5}$$

- Equation 4.1 is the incremental form of the strain decomposition. The total strain increment tensor is assumed to be the sum of an elastic part $\Delta \boldsymbol{\varepsilon}^e$ and a viscoplastic part $\Delta \boldsymbol{\varepsilon}^{vp}$.

- Equation 4.2 represents the linear elastic relation between the Cauchy stress tensor $\boldsymbol{\sigma}$ and the elastic strain tensor. In this equation the elastic modulus $\mathbf{E}$ is a fourth order tensor based on the constant scalar values of the Young's modulus E and Poisson's ratio ν, given in Table 4.1.

- Equation 4.3 is the evolution law (flow rule) for the viscoplastic strain rate. Extending the notion of associative plasticity to viscoplasticity, the viscoplastic strain increment is assumed to be in the direction of the deviatoric stress. The plastic multiplier $\Delta \lambda$ is used to scale the viscoplastic strain rate. The deviatoric stress $\mathbf{s}$ is defined by:

$$\boldsymbol{\sigma} = \mathbf{s} - p\mathbf{I}, \quad p = -\tfrac{1}{3} \mathrm{tr} \left(\boldsymbol{\sigma} \right) \tag{4.6}$$

with p the hydrostatic stress and $\mathbf{I}$ the second order unit tensor.

- Equation 4.4 gives the limit function. This function describes the rate dependent behaviour of the material in the plastic domain. The effective stress is calculated with the Von Mises criterion:

$$\overline{\sigma} = \sqrt{\tfrac{3}{2} \mathbf{s} \colon \mathbf{s}} \tag{4.7}$$

61

The flow stress, σ_f, is a function of the state variables κ and $\dot{\kappa}$, representing the equivalent plastic strain and equivalent plastic strain rate respectively. These are defined by the following equations:

$$\kappa_{n+1} = \kappa_n + \sqrt{\tfrac{2}{3}\Delta\varepsilon^{vp} : \Delta\varepsilon^{vp}} \tag{4.8}$$

$$\dot{\kappa}_{n+1} = \frac{\sqrt{\tfrac{2}{3}\Delta\varepsilon^{vp} : \Delta\varepsilon^{vp}}}{\Delta t} \tag{4.9}$$

- Equations 4.5 are the Kuhn-Tucker loading-unloading conditions. The material can be in two states. Firstly the elastic state for which the plastic multiplier is zero and the limit function is lower than or equal to zero. Secondly the plastic state, for which the plastic multiplier is larger than zero and the limit function is zero.

The constitutive behaviour of the specific aluminium alloy is represented in (4.4) by the flow stress. For the simulations presented in this work the relationship between σ_f, $\dot{\kappa}$ and T is given by a hyperbolic sine law [1]. This law is adapted for the effect of solution hardening by Mg and Si atoms in the aluminium matrix as described previously [2, 7]:

$$\sigma_f = s_m \text{arcsinh}\left(\left(\frac{Z}{A}\right)^{\frac{1}{m}}\right)$$

$$Z = (\dot{\kappa} + \dot{\kappa}_0)\exp\left(\frac{Q}{RT}\right) \tag{4.10}$$

$$A = \exp\left(K_1\right)\exp\left(-K_2 X\right)$$

$$X = 2\,[\text{Mg}] + [\text{Si}]$$

Here s_m and m are strain rate sensitivity parameters, assumed to be constant in the experimental regime, Z is the Zener-Hollomon parameter, Q is the apparent activation energy of the deformation process during plastic flow, R is the universal gas constant, T is the absolute temperature and A is a factor, depending explicitly on the Mg and Si matrix solute content. The quantity X is the weighted solute content in the aluminium matrix, K_1 and K_2 are experimentally determined model constants, and [Mg] and [Si] are the solute contents of Mg and Si in the matrix. Because of the high strains encountered in extrusion, strain hardening can be neglected [10].

62

Table 4.1: Constitutive parameters of the adapted hyperbolic sine law.

elastic properties:	E (MPa)	40000
	ν	0.35
constitutive par.:	$\dot{\kappa}_0$ (s^{-1})	0.005
	s_m (MPa)	30.9
	m	4.49
	K_1	27.7
	K_2 (wt%$^{-1}$)	2.52
	Q (J/mol)	$1.58 \cdot 10^5$
	R (J/molK)	8.134

Therefore the equivalent plastic strain is not included in the constitutive model and thus (4.10) describes only the steady state behaviour of the material.

The values of parameters s_m, m, Q, K_1 and K_2 were determined for the same alloy as used in this work independently from the extrusion trials, using plane strain compression tests [2]. These tests were carried out at temperatures of 673 K - 773 K and at strain rates up to 40 s^{-1}. The parameter values are given in Table 4.1. The constant $\dot{\kappa}_0$ is added to the equivalent strain rate in (4.10) to include an elastic region in the material behaviour with a temperature-dependent elastic flow stress at zero strain rate.

4.3 Experimental and numerical setup

The constitutive model described in the previous section was implemented in a finite element code. With this code, simulations were made of isothermal extrusion experiments. The experimental and numerical setup of the extrusion trials is discussed in this section.

4.3.1 Material preparation

A commercial aluminium AA6063 billet with a composition (wt%) Mg: 0.45, Si: 0.4, Fe: 0.19, others < 0.05, Al: balance, was homogenised at 843 K for 4 hours, quenched with forced air to room temperature and subsequently extruded to a rectangular profile with dimensions $1000 * 1000 * 30$ mm^3. From this profile, 12 cylindrical billets

63

Table 4.2: Solute contents for the various material conditions.

alloy condition	[Mg]) (wt%)	[Si] (wt%)	X (wt%)
WQ	0.45	0.4	1.3
β_1	0.046	0.14	0.23
β_2	0.24	0.25	0.73

with diameter 29 mm and length 70 mm were taken. The longitudinal direction of the billets was in the same direction as that of the rectangular profile. The billets were homogenised for 6 hours at 853 K and water quenched to room temperature (WQ-condition). Subsequently, six billets were over-aged at 623 K (β_1 condition), or 723 K (β_2 condition) for 72 hours, three at each temperature, and water quenched to create microstructures with equilibrium volume fraction of β-Mg$_2$Si precipitates corresponding to these temperatures. The matrix concentrations [Mg] and [Si] of the WQ billets are taken identical to the nominal alloy content, whereas for the over-aged billets they were calculated with the thermodynamic software package MTDATA [11]. The Mg and Si concentrations are listed in Table 4.2.

4.3.2 Extrusion trials

The billets were extruded isothermally to a rectangular strip of 1.5 mm $*$ 7.5 mm on a laboratory scale vertical 800 tons extrusion press, with a cylindrical billet container of 70 mm $*$ $\varnothing$30 mm. The billet was inserted into the container, held for 10 minutes to obtain a uniform temperature distribution in billet and container, and isothermally extruded. The extrusion temperature is measured in the die, close to the die opening, approximately 2 mm from the metal flow. The time constant of the temperature measurement was estimated to be 2 s. Isothermal extrusion was accomplished by adapting the extrusion speed to control the developed heat of deformation. To ensure initiation of extrusion the billet preheat temperature was set to 15 K below the pre-set extrusion temperature.

In Figure 4.1 a schematic display is given of the extrusion press. The die has a relieved bearing, as sketched in the detailed view given in Figure 4.1b. A relieved bearing minimises the effect of friction. The figure also indicates the location of the thermocouple.
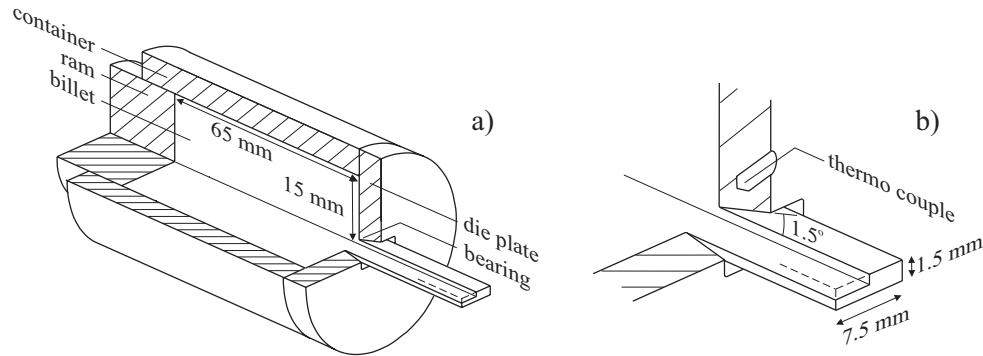
Figure 4.1: Schematic display of the miniature extrusion press; a) ram, container and die; b) detailed display of the die.

The WQ-billets were extruded at 623 K and 723 K, the β_1 billets at 623 K and the β_2 billets at 723 K. Although some degree of dynamic precipitation from the supersaturated solid solution might occur during extrusion of the WQ billets at both temperatures, the solute contents of the β_1 and β_2 billets are stable. During extrusion the location of the ram, extrusion pressure and extrusion temperature were registered using a multi-channel data-logger. Each extrusion test was carried out in triplicate. The experimental accuracy of the extrusion pressure was estimated to be 20 MPa.

4.3.3   Numerical modelling

The simulations of the extrusion process were carried out with the finite element code DiekA. This is an Arbitrary Lagrangian Eulerian (ALE) code developed by Huétink *et al.* [12]. The ALE method can be used to avoid mesh distortion, which occurs when modelling large plastic deformations with a Lagrangian description. With the ALE method the material and mesh displacements are de-coupled and can be controlled independently. The ALE formulation is very suitable for modelling the extrusion process. Inside the die, where high deformations occur, the mesh does not change position. This is accomplished by choosing the mesh displacement equal to zero (effectively a Eulerian description). On the other hand, when the material leaves the die a free surface is formed. In the direction normal to this surface the mesh displacement will be equal to the material displacement. In this way elastic deformation of the profile due to residual stresses in the material can be modelled, which is not possible when using a Eulerian description.
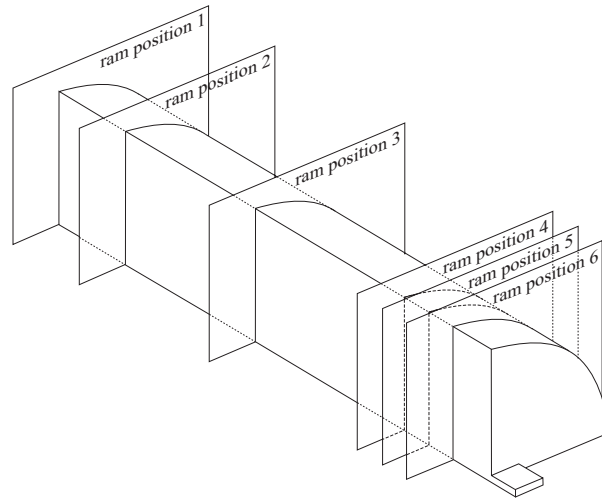
65

Figure 4.2: Simulations are performed for indicated ram positions, located at 65 mm, 56 mm, 36 mm, 13 mm, 10 mm and 6 mm from the die plate.
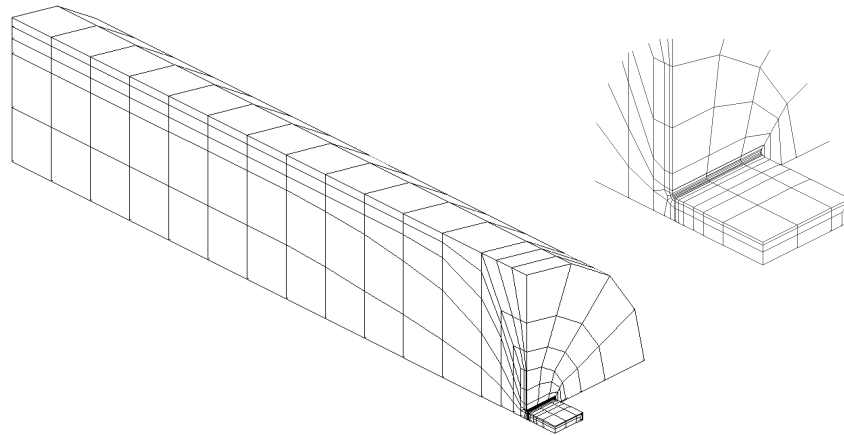

Figure 4.3: Finite element mesh, indicating the refinements near the container boundary and the die.

The extrusion process is not a stationary process, because of the cyclic loading of the billets. To calculate the extrusion pressure as a function of the ram displacement transient calculations should be performed. However this requires a very small time step to ensure stability in the fine mesh at the bearing, resulting in unacceptable calculation times. To avoid these long calculation times the following approach was adopted. For certain ram positions, illustrated in Figure 4.2, the stationary solution of the problem was calculated, which requires only a limited number of increments, and took about 5-10 minutes on a HP J5000 workstation.

In the simulations for each ram position the ram speed was determined from the experimental data and applied to the back of the billet as a boundary condition. The calculations were performed isothermally, with a temperature equal to the pre-set die temperature in the experiment. A drawback of this procedure is the inability to calculate an exact temperature distribution in the billet. However, since extrusion in the experiments was carried out rather slowly (typical ram speeds < 1 mm/s), it was assumed that the effects of local heating were not significant.

The mesh used in the FEM model is illustrated in Figure 4.3. Only a quarter of the experimental set-up is modelled because of symmetry. During the process most deformation occurs in the area directly in front of the bearing. In the container deformation occurs at the wall while at the centre the material moves as a plug. These effects were taken into account during the construction of the mesh. In the container a relatively coarse mesh was used, with smaller elements near the wall. In the bearing area a fine mesh was used.

At the interface between the die and the aluminium billet a Coulomb friction law is applied with a friction coefficient of 0.25. In the simulations the value of the friction coefficient has only a very limited influence on the results, because slipping friction occurs only at the bearing and a relieved bearing was used. Inside the container a stick condition was applied because the friction stresses are much larger than the internal shear strength of aluminium. It must be emphasised that no parameter was adjusted to fit the numerical results to the results of the experiments. The material parameters were determined independently from the extrusion experiments and the influence of the friction coefficient is too small to be used as a fitting parameter.

4.4 Results

One of the main advantages of numerical simulations is that they offer the opportunity to observe effects that occur inside the process. These effects cannot be investigated experimentally. The experimental results however serve as a link to the real process and offer a means of verifying the numerical result. In this section, both the experimental and numerical results are discussed.

4.4.1 Laboratory scale extrusion

In Figures 4.4 and 4.5 the extrusion pressure, ram velocity and die temperature are plotted as a function of the ram position. Ram position 0 corresponds to the ram touching the die. The figures indicate that, after a sharp increase of the extrusion pressure during the upsetting of the billet, two stages can be discerned. Firstly an initial stage is observed (ram position 64 - 48 mm), which is characterised by a high extrusion pressure, a high, but rapidly decreasing ram velocity and a die-temperature drop below the pre-set value. This initial stage lasts approximately 2 s. After a pressure dip a second stage is observed (ram position 48 - 5 mm) at which the pressure remains relatively low and the ram velocity is almost constant and an order of magnitude lower than in the initial stage. During this stage, which lasts approximately 60 s, extrusion proceeds isothermally. The pressure dip before the second stage is an experimental artifact resulting from the ram velocity momentarily dropping to zero when the temperature at the die overshoots the pre-set temperature as a result of the added heat of deformation, see Figure 4.5.

In the extrusion pressure the following trends are observed. The extrusion pressure of the WQ billets is higher than those of the over-aged billets β_1 and β_2, which is attributed to the higher degree of solution hardening in the WQ billets. Also, the extrusion pressures at 623 K are higher than at 723 K, due to the temperature dependence of the deformation resistance. Furthermore, the relative difference in extrusion pressure between the WQ and β_1 condition at 623 K is higher than that between the WQ and β_2 condition at 723 K, which can be attributed partly to a higher difference in solute content at 623 K, see Table 4.2. The small difference between the WQ and β_2 condition at 723 K will be discussed in Section 4.5.2.
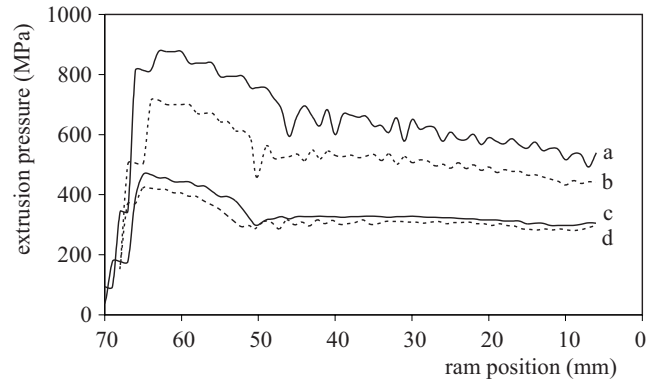
68

Figure 4.4: Extrusion pressure as a function of the ram position; a) WQ-condition, 623 K; b) β_1-condition, 623 K; c) WQ-condition, 723 K; d) β_2-condition, 723 K.
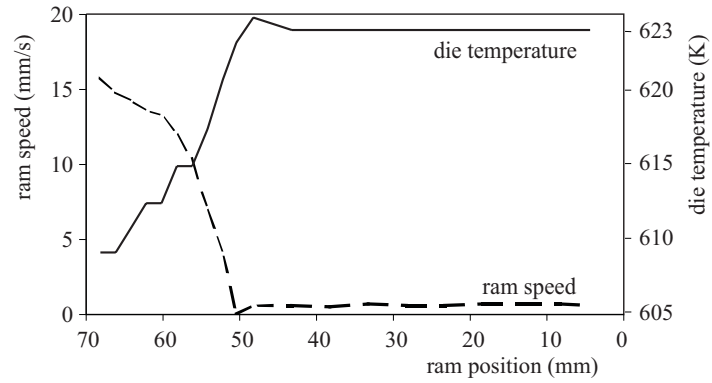

Figure 4.5: Extrusion ram velocity together with the die temperature as a function of the ram position for the β_1-condition, extrusion temperature 623 K.

69

Figure 4.6: Extrusion pressure as a function of the ram position at 623 K, including the simulated curves (dashed lines; marks indicate actual simulations).

4.4.2 Numerical simulations

In Figures 4.6 and 4.7 the calculated and measured extrusion pressure curves are plotted as a function of the ram position. The numerical pressures were calculated by dividing the sum of the reaction forces at the ram by the area of the ram. It can be observed that the calculated curves predict well the absolute pressure levels (typical accuracy of 10 %), although in the initial stage the pressures are over-estimated, and in the secondary stage they are somewhat underestimated. Furthermore, in the secondary stage the pressure decrease with ram position is predicted accurately.

The trends with temperature are similar for both experiments and simulations. The pressure difference resulting from the different degrees of solution hardening of the WQ and over-aged billets is predicted accurately at 623 K, but is somewhat overestimated at 723 K.

In Figure 4.8 contour plots of extrusion pressure and Von Mises stress are given for certain combinations of extrusion temperature, ram position, and pre-treatment condition. The Von Mises stress contours in Figure 4.8 correspond to strain rate contours, listed in Table 4.3. Two deformation zones can be clearly discerned:

- A plug flow zone in the container, characterised by a relatively thin layer of large shear close to the container wall with strain rates up to 1.5 s^{-1} and a large region with very low deformation rates (< 0.1 s^{-1}) in the centre of the container.
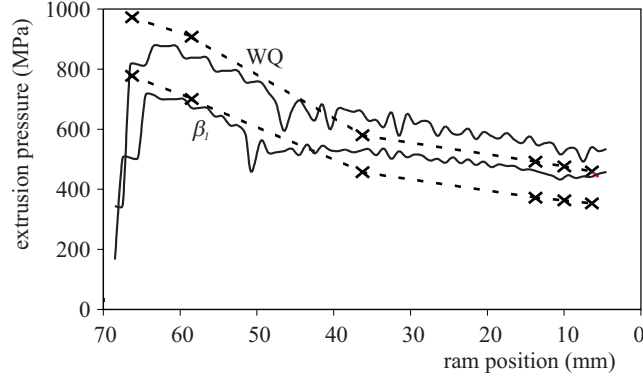
70
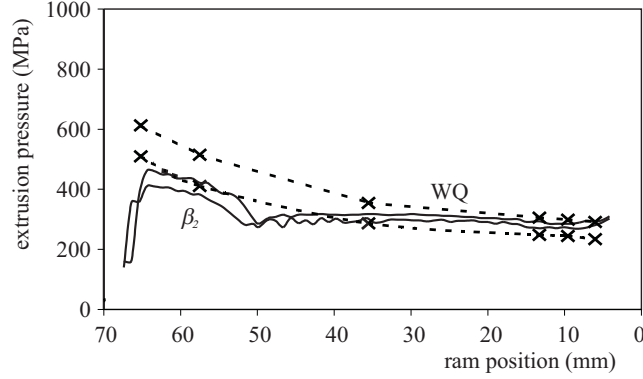
Figure 4.7: Extrusion pressure as a function of the ram position at 723 K, including the simulated curves (dashed lines; marks indicate actual simulations).

- A deformation zone near the die where the material flows to the die opening. In this area the strain rates have values 10 s^{-1} and higher, up to 1000 s^{-1}.

The Von Mises stress contours in Figures 4.8a and 4.8b indicate that the flow patterns are similar at both temperatures, and that only the absolute flow stress and pressure levels differ. In the plug flow zone the pressure decreases linearly with decreasing distance from the die, and the pressure drop at 623 K is approximately twice as large as at 723 K. This difference is related partly to the difference in temperature and partly to a higher ram speed at 623 K. Investigation of the resulting strain rates indicate that ram velocity and strain rate are proportional. Furthermore, it can be observed from the Von Mises stress contours that a small dead metal zone near the die (right hand corner) has formed where the material is in the elastic state (< 19.25 MPa at 623 K, < 10.21 MPa at 723 K).

4.5   Discussion

A good agreement exists between numerical calculations and experimental results with respect to both absolute extrusion pressure levels and trends with solute content and temperature. A similar agreement was reported in the limited number of comparable studies found in the literature [13, 14, 15].

The calculations can be used to quantify the contributions of the plug flow zone and the deformation zone near the die to the extrusion pressure. They also provide infor-

Figure 4.8: Pressure(MPa) in upper graph and Von Mises stress contours(MPa) in lower graph for; a) β_1 billet at 623 K, initial stage (ram position 65 mm, ram spe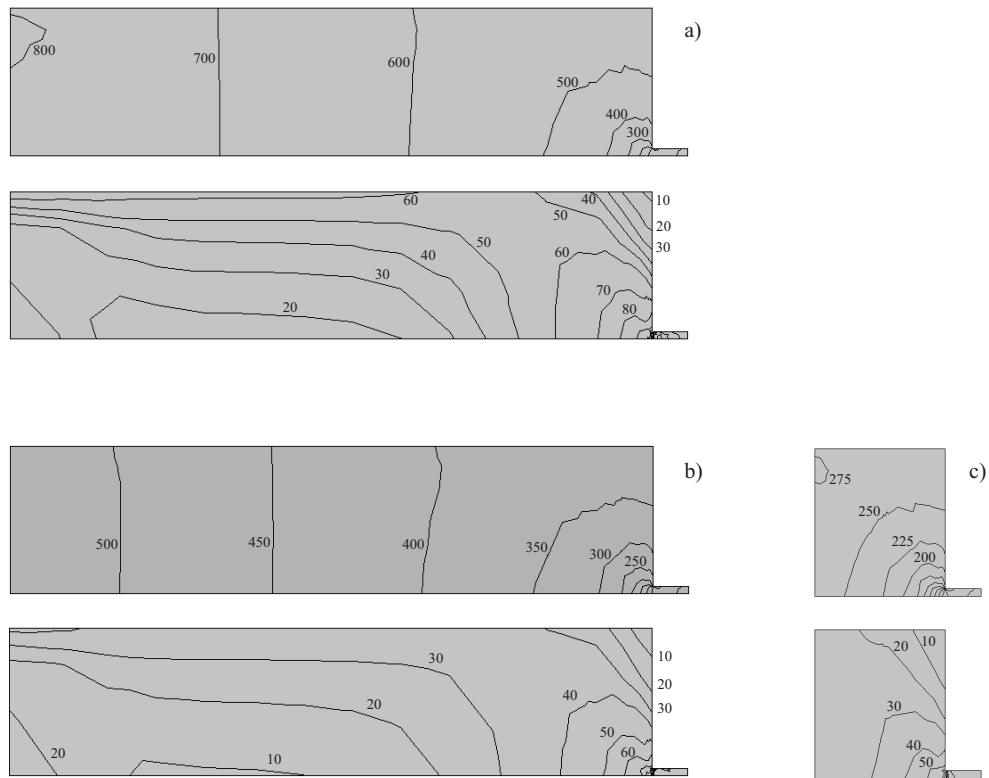ed 14.7 mm/s); b) β_2 billet at 723 K, initial stage (ram position 65 mm, ram speed 6.7 mm/s); c) β_2 billet at 723 K, second stage (ram position 13 mm, ram speed 0.87 mm/s).

Table 4.3: Conversion of Von Mises stress into equivalent strain rate for the overaged conditions at both extrusion temperatures.

Von Mises stress (MPa)	plastic strain rate β_1 623 K (s^{-1})	plastic strain rate β_2 723 K (s^{-1})
10	(elastic)	(elastic)
20	(elastic)	0.11
30	0.049	1.02
40	0.317	6.12
50	1.61	30.7
60	7.44	141
70	32.8	622
80	141	2680
90	602	
100	2550	

mation on flow stress values and strain rates encountered in the material. Differences in temperature and material condition result in different flow stress and extrusion pressure values, but yield similar flow patterns. Finally, the development of a small dead metal zone near the die could be followed.

However, some discrepancies can be distinguished between experiments and simulations: In the simulations the pressure level in the secondary stage is somewhat underestimated, and is somewhat overestimated in the initial stage. Also, the effect of the difference in solution hardening is overestimated at 723 K. These discrepancies will be discussed below, but it should be noted that during the initial stage extrusion proceeds under unstable press conditions, which reduces the accuracy of the experimental results at this stage. Additional effects, which are not accounted for in the numerical model, such as friction between ram and container, may also result in discrepancies between the pressure levels in experimental curves and those predicted by the simulations.

4.5.1 Prediction of the pressure for the initial and secondary stage of extrusion

It can be observed in Figure 4.6 and 4.7 that for all simulated cases the slopes of the experimental and calculated results are in good agreement, indicating that the

model predicts the material behaviour in the plug flow zone accurately. However, in the secondary stage the absolute level of the calculated curves deviates from the experimental results, which indicates that here the pressure calculated for the deformation zone around the die is underestimated. In this area the generated pressure is dominated by high strain rates.

As indicated in the description of the constitutive model the parameter set corresponding to (4.10) was determined using plane strain compression tests for strain rates up to 40 s^{-1}, whereas in the deformation zone near the die the strain rate reaches values up to 1000 s^{-1}. It is therefore possible that at high strain rates the flow stress values calculated with (4.10) may deviate from the flow stress of the real material.

Furthermore, it has been reported that for strain rates of approximately 1000 s^{-1} the strain rate sensitivity of aluminium alloys begins to increase dramatically, which could be caused by inertial effects [16, 17]. The increase of the strain rate sensitivity near 1000 s^{-1} as well as the effect of the limited range of the compression tests when extrapolating to strain rates > 40 s^{-1} may lead to an underestimation of the real flow stress.

To illustrate this, in Figure 4.9 some calculated flow stress values are plotted as a function of $\ln(\dot{\kappa})$ using the parameter values of Table 4.1, together with an alternative parameter set with $s_m = 41.7$ MPa and $K_1 = 29.7$. Some experimental data points are also plotted, with error bars indicating the experimental accuracy of 3 MPa. Both parameter sets describe the experimental values within the bounds of experimental accuracy, but the alternative parameter set yields flow stress values more than 10 % higher at strain rates approaching 1000 s^{-1}. When this second set is used in the simulations, an extrusion pressure is calculated which describes the experimental results to within 5 %. This shows the significance of having flow stress data available covering rates of up to 1000 s^{-1}.

The overestimation in the initial stage of extrusion can be explained by considering that in the laboratory scale extrusion tests the ram velocities and thus the strain rates are an order of magnitude higher than in the secondary stage. This results in a relatively large area in the deformation zone with strain rates of 10 s^{-1} or higher, and increased adiabatic heating. However, this cannot be registered by the thermocouple since the time constant of the temperature measurement (± 2 s) is similar to the time length of the initial stage. This means that in the initial stage the extrusion temperature in the experiment is probably higher than the pre-set value that was

74
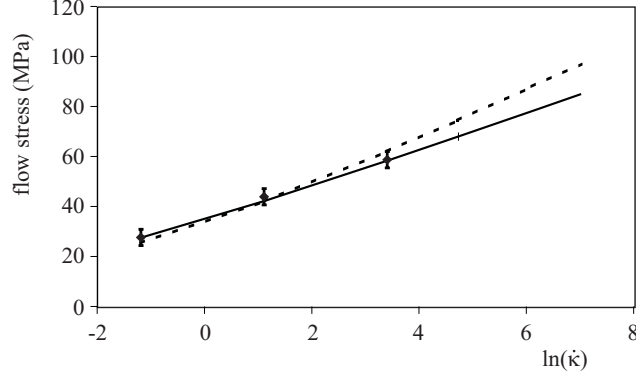
Figure 4.9: Experimental and calculated flow stress as a function of $\ln(\dot{\kappa})$ the error bars indicate the experimental accuracy of the compression test data.

used in the simulations. From Figure 4.4 it can be estimated that a temperature increase of ± 30 K is sufficient to explain the overestimation in the initial stage. This temperature increase is realistic when the high ram velocity in the initial stage is taken into account.

4.5.2 Overestimation of the solute effect on the pressure at 723 K

At 723 K the extrusion experiments showed a much smaller difference between the pressure levels of the WQ and β_2 condition than the simulations, whereas at 623 K the difference was predicted accurately. Also, compression tests with these material conditions showed a significant solute effect at both 623 K and 723 K [2, 18]. It is apparent that during extrusion at 723 K considerable softening of the WQ material takes place. Because the foremost difference between the compression tests and the extrusion trials is the difference in strain rates this softening is attributed to the high strain rates in the deformation zone at the die. In this section possible high strain rate/temperature effects are considered which could cause this softening effect of the WQ condition.

Possible material effects which may occur during extrusion at high strain rates are dynamic precipitation, dynamic recrystallisation, and strain localisation effects by the formation of shear bands or local loss of coherency of the crystal structure. Dynamic recrystallisation is strongest at high values of Z [10, 19], and hence a larger softening

75

would be expected at 623 K than at 723 K, in contrast to the observations. Similar considerations rule out strain localisation [10, 20, 21] as the pertinent mechanism.

Dynamic precipitation induces softening of the material as a result of the reduction of the solute content by precipitation of alloying elements from the solid solution of the matrix during deformation. This has been observed during hot deformation at strain rates ± 1 s^{-1} of highly supersaturated alloys - AA2XXX and highly alloyed AA6XXX - [22, 23]. The driving force for dynamic precipitation is the supersaturation level of the solid solution, and therefore precipitation should be more probable at 623 K than at 723 K, and for supersaturated material. However, at the high strain rates encountered in extrusion the subgrain size of the dislocation cell structure becomes comparable to the diffusion length of the solute atoms. At this stage all solute is within the range of the subgrain boundary, which acts as a nucleation site for dynamic precipitation, and the chance that alloying atoms reach a subgrain boundary by diffusion increases with the temperature. The diffusion length l_D, that solute can travel to reach a nucleation site, is given by:

$$l_D \approx \sqrt{\pi D_i\left(T_0\right) t_{def}} \tag{4.11}$$

in which $D_i\left(T_0\right)$ represents the diffusion coefficient of the solute element i in the matrix at the process temperature T_0 and t_{def} represents the time scale of the deformation process. The temperature dependence of $D_i\left(T_0\right)$ is given by:

$$D_i\left(T_0\right) = D_{0,i}\exp\left(\frac{-Q_i}{RT_0}\right) \tag{4.12}$$

Here $D_{0,i}$ is a constant and Q_i is the activation energy for diffusion of element i in the matrix. Nes [24] showed that, using the principle of similitude observed by Castro-Fernandez et al. [25], the subgrain size, δ, can be related to the flow stress by:

$$\delta = \frac{cGb}{\sigma_f - \sigma_i} \tag{4.13}$$

where c is a constant, G is the shear modulus, b is the length of the Burgers vector for aluminium and σ_i represents frictional stress opposing the moving dislocation. The probability that nuclei are formed or that pre-existing nuclei grow can be expected to increase dramatically when the solute atoms can reach the surplus of nucleation sites at the subgrain boundary within a time t_{def}. This occurs when:

$$\frac{l_D}{\delta} = \frac{\sigma_f - \sigma_i}{cGb}\sqrt{\pi D_i\left(T_0\right) t_{def}} \approx 0.5 \tag{4.14}$$

Table 4.4: Flow stress values and strain rates corresponding to $l_D/\delta = 0.5$.

T (K)	l_D (m)	σ_f (MPa)	$\dot{\kappa}$ (s^{-1})	$l_D/\delta > 0.5$ in deformation zone dynamic precipitation possible
623	$2.5 \cdot 10^{-8}$	286	$1.2 \cdot 10^{14}$	no
723	$1.5 \cdot 10^{-7}$	59	35	yes
773	$3.2 \cdot 10^{-7}$	36	4.8	yes

At temperatures of 623 K and higher $D_{\mathrm{Mg}} \geq D_{\mathrm{Si}}$ and the diffusion rate of Si is the limiting factor for dynamic precipitation. For Si, $D_0 = 2.02 \cdot 10^{-4}$ m^2/s, $Q = 136000$ J/mol [26], and during hot deformation $cGb \approx 13.6$ MPa m [6, 24]. For σ_i a value of 15 MPa was taken. The residence time of the material in the deformation zone around the die where strain rates are 10 s^{-1} or higher was estimated to be $t_{def} \approx 0.25$ s. In Table 4.4 estimates are given of the flow stress and strain rate at which the dimensionless number l_D/δ becomes 0.5 for a range of temperatures. The strain rates were calculated from the σ_f values using (4.10). The trends in the values are relatively insensitive to the precise value of σ_i.

It can be observed that at 623 K the strain rates needed for enhanced dynamic precipitation are out of the range typical for the deformation zone (10 s$^{-1} \leq \dot{\kappa} \leq 1000$ s^{-1}), and dynamic precipitation is not possible. On the other hand at 723 K the deformation zone has strain rates satisfying the condition $l_D/\delta > 0.5$ and dynamic precipitation is possible. Furthermore, it should be noted that the actual diffusion length during hot deformation is not well known and may be larger than the diffusion length under static conditions used here, because of an excess of vacancies and travelling dislocations. Taking for instance a D_0 value 7 times higher than the used value still does not allow for dynamic precipitation at 623 K, and does allow for dynamic precipitation at 723 K. Considering the supersaturation of the WQ billets and a value of $l_D/\delta = 0.5$ at 723 K, dynamic precipitation is adopted as the most likely explanation for the softening of the WQ material during extrusion at 723 K.

4.5.3 Application of the model to industrial extrusion

Although the flow stress values and strain rates in industrial extrusion are similar to those in the described trials, industrial extrusion distinguishes itself from the laboratory scale extrusion trials presented in this study in at least three important aspects: it is non-isothermal, the condition of alloying elements in the alloy changes dynam-

ically during the extrusion process and the geometrical length scales are a factor 10 larger.

The presented FEM code including the solute dependent material model can in principle be applied for modelling non-isothermal extrusion when transient calculations are performed. However, the complexity of the problem to be solved is limited by the computational capacity available, and is strongly related to the complexity of the geometry of the die and the mesh necessary to accurately discretise this geometry. Furthermore, dynamic changes in the condition of Mg and Si take place and affect solution hardening and the condition of Mg and Si after extrusion. These changes can be simulated making use of recently developed models [27, 28, 29], which are capable of describing particle dissolution during a specific temperature-time path. Using these models a table can be generated which can be used to monitor the typical Mg_2Si precipitate size and solute content during simulation of the extrusion process, and can be incorporated into the solute-dependent material model. However, it should be noted that the diffusion coefficients of solute Mg and Si during hot deformation of aluminium are not well known. Further, dynamic precipitation is not likely to occur during extrusion of AA6XXX alloys other than in very highly alloyed systems, because the solvus temperature is often exceeded by the extrusion temperatures in the industry of about 773 K.

In principle the difference in scale of typical industrial and laboratory scale extrusion presses need not cause complications. However, in a typical industrial extrusion press the boundary conditions, for instance temperatures and heat flux at the ram, container and die interface, are less well known than in laboratory scale tests, and additional inaccuracies would seem unavoidable.

4.6 Conclusions

Numerical simulations were carried out on a series of isothermal laboratory scale extrusion trials of aluminium AA6063 billets using the FEM code DiekA. The effect of solution hardening by Mg and Si on the extrusion process was calculated by incorporating a hyperbolic sine law adapted for the effect of solution hardening by Mg and Si. The absolute extrusion pressure levels and pressure decrease with ram position, the flow stress values and the strain rates were investigated. To explain the observed differences between simulations and experiments, the effects of adiabatic heating, dynamic recrystallisation, strain localisation and dynamic precipitation were considered.

The following conclusions are drawn:

- The FEM code DiekA with the adapted hyperbolic sine provides a suitable model for the simulation of isothermal extrusion, without using any fitting parameters. The model allows for the quantification of pressure levels, pressure drop along the billet length, solute effects, flow stress and strain rate levels.

- A good overall agreement was found between simulations and experiments.

- For an accurate description of the material behaviour of aluminium alloys under hot extrusion conditions it is desirable to extend the range of strain rates covered in the experimental determination of the material parameters to values up to 1000 s^{-1}.

- It is inferred that for supersaturated AA6063 dynamic precipitation at high strain rates plays an important role in extrusion at 723 K. Dynamic precipitation is absent at 623 K.

- The described approach can, in principle, be extended to industrial situations.

References

[1] J. J. Jonas, C. M. Sellars, and W. J. McG. Tegart. Strength and structure under hot-working conditions. *Met. Review*, 14:1–24, 1969.

[2] J. van de Langkruis, W. H. Kool, C. M. Sellars, M. R. van der Winden, and S. van der Zwaag. The effect of β,β' and β'' precipitates in a homogenised AA6063 alloy on the hot deformability and the peak hardness. *Mat. Sci. Eng. A*, 2000. accepted for publication.

[3] T. Chanda, J. Zhou, L. Kowalski, and J. Duszczyk. 3D FEM simulation of the thermal events during AA6061 aluminium extrusion. *Scripta Mater.*, 41:195–202, 1999.

[4] B. J. E. van Rens. *Finite element simulations of the aluminium extrusion process.* PhD thesis, Technical University Eindhoven, The Netherlands, 1999.

[5] H. G. Mooi. *Finite element simulation of aluminium extrusion.* PhD thesis, University of Twente, The Netherlands, 1996.

[6] H. J. Frost and M. F. Ashby. *Deformation-mechanism maps*, chapter 1, page 13. Pergamon press, 1982.

[7] J. Langkruis, W. H. Kool, and S. van der Zwaag. Assessment of constitutive equations in modelling the hot deformability of some overaged Al-Mg-Si-alloys with varying solute contents. *Mat. Sci. Eng. A*, 266:135–145, 1999.

[8] F. Auricchio and R. L. Taylor. A generalized visco-plasticity model and its algorithmic implementation. *Computers & Structures*, 53:637–647, 1994.

[9] M. Ortiz and E. P. Popov. Accuracy and stability of integration algorithms for elastoplastic constitutive relations. *Int. J. Numer. Meth. Engng.*, 21:1561–1576, 1985.

[10] F. J. Humphreys and M. Hatherly. *Recrystallization and Related Annealing Phenomena*. Pergamon, Elseviers Science Ltd, Oxford, United Kingdom, 1996.

[11] R. H. Davies, A. T. Dinsdale, J. A. Gisby, S. M. Hodson, and R. G. J. Ball. Thermodynamic modelling using mtdata; a description showing applications involving oxides, alloys and aqueous solutions. In *Applications of thermodynamics in the synthesis and processing of materials*, page 371. Minerals, metals and materials society/AIME, 1996.

[12] J. Huétink. *On the simulation of thermomechanical forming processes*. PhD thesis, University of Twente, The Netherlands, 1986.

[13] G. Grasmo, K. Holthe, S. Støren, H. Valberg, R. Flatval, L. Hanssen, M. Lefstad, O. Lohne, T. Welo, R. Ørsund, and J. Herberg. Modelling of two-dimensional extrusion. In *Proc. 5th International Extrusion Technology Seminar*, pages 367–376, Wauconda, Illinois, 1992. Aluminum Association and Aluminum Extruders Council.

[14] R. J. Dashwood, H. B. McShane, and A. Jackson. Computer prediction of extrusion limit diagrams. In *Proc. 6th International Extrusion Technology Seminar*, pages 331–339, Wauconda, Illinois, 1996. Aluminum Association and Aluminum Extruders Council.

[15] Y. S. Kang and D. Y. Yang. Investigation into the thermo-viscoplastic finite element analysis of square die extrusion of square section with Lagrangian description. *Int. J. Mach. Tools Manufact.*, 36:907, 1996.

[16] U. F. Kocks, A. S. Argon, and M. F. Ashby. Thermodynamics and kinematics of slip. In *Prog. Mat. Sci.*, volume 19, pages 68–109, Oxford, 1975. Pergamon.

[17] J. R. Newby, J. R. Davis, and S. K. Refsnes. *Metals Handbook*, volume 8. American Society for Metals, 1985.

[18] J. van de Langkruis, R. Bergwerf, S. van der Zwaag, and W. H. Kool. Linking plain strain compression tests on AA6063 to laboratory scale extrusion via constitutive equations. In *Mat. Sci. Forum*, volume 331-337, pages 565–570, Charlottesvile, USA, 2000. Proc. of Conference on Aluminium Alloys: Their physical and mechanical properties, ICAA7.

[19] H. J. McQueen, E. Evangelista, and M. E. Kassner. The classification and determination of restoration mechanisms in the hot working of aluminium alloys. *Z. Metallkde*, 82:336–345, 1991.

[20] J. Liu and R. D. Doherty. Particle simulated nucleation of recrystallization in Al-Mg$_2$Si. In *Aluminium Technology '86*, pages 347–356, London, UK, 1986. The Institute of Metals.

[21] J. Hjelen, R. Ørsund, and E. Nes. On the origin of recrystallization textures in aluminium. *Acta Metall.*, 39:1377–1404, 1991.

[22] B. Verlinden, P. Wouters, H. J. McQueen, E. Aernoudt, L. Delaey, and S. Cauwenberg. Effect of different homogenization treatments on the hot workability of aluminium alloy AA6024. *Mat. Sci. Eng. A*, 123:229–237, 1990.

[23] H. J. McQueen and O. C. Celliers. Application of hot workability studies to extrusion processing. I Extrusion control parameters and constitutive equations. *Mat. Sci. Forum*, 17:1–13, 1993.

[24] E. Nes. Modelling work hardening and stress saturation in fcc metals. In *Prog. Mat. Sci.*, volume 41, pages 129–193, Oxford, 1997. Permagon.

[25] F. R. Castro-Fernandez, C. M. Sellars, and J. A. Whiteman. Changes of flow stress and microstructure during hot deformation of Al-MgMn. *Mat. Sci. Techn.*, 6:453–460, 1990.

[26] S. I. Fujikawa, K. Hirano, and Y. Fukushima. Diffusion of Si in aluminium. *Metall. Trans.*, 9A:1811–1815, 1978.

[27] F. J. Vermolen. *Mathematical models for particle dissolution in extrudable aluminium alloys.* PhD thesis, Delft University of Technology, Delft, The Netherlands, 1998.

[28] F. J. Vermolen, K. Vuik, and S. van der Zwaag. A mathematical model for the dissolution kinetics of Mg_2Si-phases in Al-Mg-Si alloys during homogenisation under industrial conditions. *Mat. Sci. Eng. A*, 254:13–32, 1998.

[29] S. P. Chen, M. S. Vossenberg, F. J. Vermolen, J. van de Langkruis, and S. van der Zwaag. Dissolution of β particles in an Al-Mg-Si alloy during dsc runs. *Mat. Sci. Eng. A*, 272:250–256, 1999.

Chapter 5

FEM simulations of the extrusion of complex thin-walled aluminium sections

J. Lof and Y. Blokhuis

Abstract

The Finite Element Method can be used for the simulation of the extrusion process. However, the application of this kind of simulation in the extrusion industry is limited because of the complexity involved. In this paper a method is presented for the simulation of the extrusion of complex profiles, which can be used in an industrial environment. To this end, the bearing area is modelled using an equivalent bearing model. In this way it is possible to describe the resistance in the bearing without using a large number of elements. To avoid the time-consuming and complex work necessary for the development of the FEM model for a particular die, a specialised pre-processor is developed. This pre-processor provides a direct link between the die design in the CAD system Pro/Engineer and the simulations in the FEM code DiekA. The method is demonstrated for a particular die and the results are compared to results obtained in practise.

5.1   Introduction

Aluminium extrusion is a forming process used to produce profiles. A large variety of profiles can be made by pressing a billet of hot aluminium through a hole that closely resembles the required cross-section of the profile. At present, the design of extrusion dies and operation in extrusion companies is primarily based on trial and error. The experience of the die designer, the press operator and the die corrector to a large extent determine the performance of the extrusion die and the efficiency of the process. In order to improve the performance of dies, it is important to obtain more knowledge on the processes that occur during extrusion. To obtain such knowledge, numerical simulations can be a valuable tool. These simulations provide insight into the process which cannot easily be obtained by other methods.

Performing simulations of the extrusion of complex profiles still poses a major challenge. The problems encountered when modelling the bearing area are difficult to solve. Furthermore, much effort has to be put into pre-processing when specialised pre-processing tools are not available. This is an obstacle for the application of simulations in an industrial environment. The aim of this article is to present a method that can be used to simulate the extrusion of complex thin-walled sections, which is simple to use and delivers results fast.

In the past, simulations of extrusion have been limited to relatively simple geometries and low extrusion ratios, because of computational restrictions [1, 2]. Recently attention has shifted to extrusion of more complex thin-walled sections [3, 4]. In this kind of simulation, pre-processing difficulties start to emerge. Van Rens [5] developed a meshing algorithm specifically aimed at extrusion geometries to avoid these difficulties.

In simulations of extrusion of thin-walled sections, modelling the bearing area is complicated. The scale of this area is small compared to the rest of the process, but the deformations and velocities are very high. In order to accurately model this area, a fine mesh is necessary. This results in large calculation times and difficulties with the preparation of the mesh. By decreasing the number of elements in the bearing area, the calculation time can be reduced significantly. In the present paper, an equivalent bearing model is used to model the bearing area [6]. This is a relatively coarse mesh of the bearing which is constructed in such a way that it behaves similarly to a more detailed reference model.

Even more important than the calculation time is the time required to develop the numerical model for a specific die. Because of the complex geometry of extrusion dies, the pre-processing time can easily exceed the calculation time by orders of magnitude if pre-processing is done inefficiently. To simplify pre-processing, an application is developed in the CAD system Pro/Engineer, which is used to design the extrusion dies. The application creates a FEM model for the simulation of the aluminium flow and the deformation of the die, with minimal effort of the user, providing a direct coupling between the design process in Pro/Engineer and the simulations in the FEM code DiekA.

Details of the numerical method used for the simulation are presented in Section 5.2. The constitutive model used to describe the behaviour of hot aluminium is discussed in Section 5.3. The development of the equivalent bearing model is discussed in Section 5.4. In Section 5.5, the pre-processing phase is discussed. To illustrate the applicability of the method, a relatively complex porthole die is simulated as an example. The results of this simulation are discussed in Section 5.6 and compared to results obtained in practise.

5.2 Numerical model

To simulate the extrusion process an Arbitrary Lagrangian Eulerian (ALE) code, DiekA, was used. This code has been developed during the last fifteen years by Huétink *et al.* [7, 8, 9]. In the ALE method the mesh displacement can be controlled independently from the material displacement. The method was first developed in fluid mechanics to model fluid-structure interaction and to model the motion of free surfaces [10, 11]. Later it was introduced to solid mechanics where it is used to avoid mesh distortion which occurs when modelling large deformations with a Lagrangian description. In the extrusion process, very large deformations occur. To avoid mesh distortion, the mesh is fixed to its location, effectively a Eulerian description.

Extrusion is not a stationary process, because of the cyclic loading of the billet. Besides the loading of the billet an irregular cycle of changing of dies occurs during production. The result is a complex pattern of heating and cooling during the extrusion process. The temperature changes influence the behaviour of the aluminium. To take these changes into account, transient thermo-mechanical calculations are necessary. However, this requires a large number of calculation steps, leading to unacceptable calculation times. To avoid this, a stationary solution for the thermo-mechanical

Table 5.1: Material parameters for AA6063 alloy.

parameter		min	used	max
plastic properties:	$\dot{\kappa}_0$ (1/s)	0.001	0.005	0.01
	s_m (MPa)	25	25	76
	m	2.4	5.4	6.0
	A (1/s)	10^9	$6 \cdot 10^9$	10^{12}
	Q (J/mol)	$1.3 \cdot 10^5$	$1.4 \cdot 10^5$	$1.8 \cdot 10^5$
	R (J/molK)		8.314	

problem can be calculated in a limited number of time increments. The stationary temperature distribution gives an upper limit for the thermal problem. In reality these temperatures are never reached. Often isothermal calculations are sufficient and the thermal aspects of the problem can be neglected altogether. Especially in the case where the stresses in the die are concerned, isothermal calculations with a temperature similar to that at the start of an extrusion cycle can be seen as a worst case situation. In this paper only isothermal calculations are presented.

In order to avoid large calculation times the simulation of the aluminium flow and the stress analysis of the die are performed separately. This is possible because the deformations of the die are very small. Normally these deformations will not have a significant effect on the aluminium flow. In some cases, deformation of the die can result in small deflections of the bearing or misalignment of the two faces of the bearing, which can affect the aluminium flow. These effects are not taken into account in the simulations presented in this work.

5.3 Constitutive equations

Hot aluminium has rate dependent or viscoplastic behaviour. This behaviour can be modelled with a viscoplastic model or with an elasto-viscoplastic model. In previous work [12], the influence of the elasticity of the material is investigated. A more elaborate description of the implementation of these constitutive models is also given in this reference.

The constitutive behaviour of the specific aluminium alloy is represented by a relation between the flow stress σ_f and the equivalent plastic strain $\dot{\kappa}$. In this work a modified
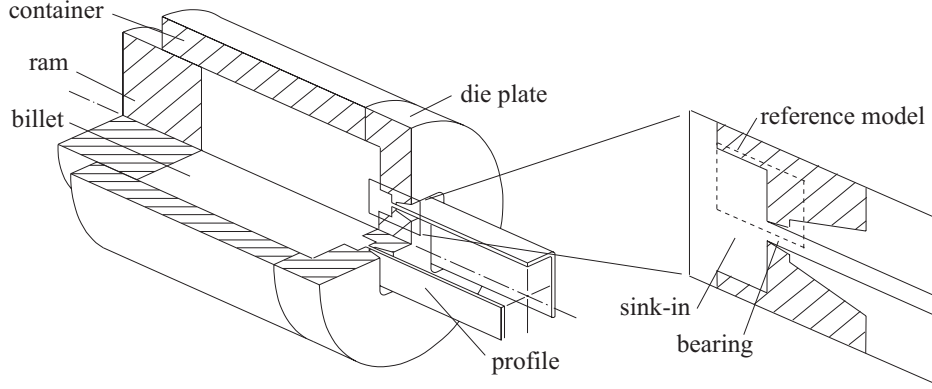
Figure 5.1: The extrusion process.

Sellars-Tegart law [12] is used to describe the behaviour of the aluminium:

$$\sigma_f\left(\dot{\kappa}, T\right) = s_m \mathrm{arcsinh}\left(\left(\frac{\dot{\kappa} + \dot{\kappa}_0\left(T\right)}{A}\exp\left(\frac{Q}{RT}\right)\right)^{\frac{1}{m}}\right) \qquad (5.1)$$

In this equation R is the gas constant, T is the temperature and s_m, A, Q and m are parameters that are used to fit the flow stress to experimental data. A temperature dependent parameter $\dot{\kappa}_0\left(T\right)$ is added to the standard Sellars-Tegart law to include an elastic region in the material law.

The parameters for this model are fitted to data obtained experimentally for an AA6063 aluminium alloy. They are based on unpublished work done at Kings College (London). Other experimental data for the AA6063 alloy was published by Akeret [13] or more recently by Langkruis [14]. In Table 1 an overview is given of the parameter ranges found for this alloy.

Large differences can be observed between the different experimental data. A number of reasons can be suggested to account for these differences. Firstly, different testing methods are used to determine the parameters, namely torsion tests as opposed to compression tests. Secondly, small variations in alloy composition are possible within the AA6063 norm. In addition to this, with the same composition, different material behaviour can occur because of variation in the solution state of alloy components [15].
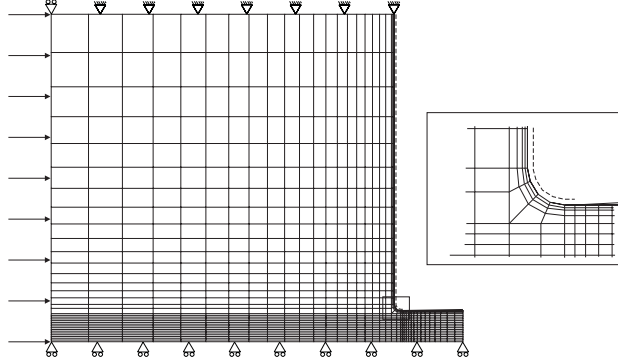
87

Figure 5.2: 2D reference model for plane strain extrusion.

5.4 Equivalent bearing model

In the extrusion process, the function of the bearing is to determine the cross-sectional shape of the profile. With parallel bearings, the length of the bearing is used to control the local exit velocity of the material. In previous work [12] it was concluded that the resistance in parallel bearings is very sensitive to small changes in the bearing angle. Because of this sensitivity it is impossible to predict the resistance in parallel bearings. An alternative to parallel bearings was suggested, namely a relieved bearing with a sink-in to control the exit velocity, as illustrated in Figure 5.1. This kind of bearing gives more predictable results. An additional advantage is the reduced extrusion pressure because of the relieved bearing. This approach was tested in practise with very satisfying results. Therefore further developments in simulation techniques for the bearing, presented in this paper, have focussed on simulating a relieved bearing.

To accurately describe the complex flow that occurs in and just in front of the bearing, a very detailed model is necessary. This model requires a large number of elements, resulting in unacceptable calculation times. An additional problem is that it is very difficult to make an adequate mesh in the bearing area for complex profiles. In order to solve these problems, the equivalent bearing model was developed.

The basic idea behind the equivalent bearing model is the following. For the simulations of the extrusion process we are interested in the general behaviour of the aluminium flow, for example the loads that are imposed on the die and the velocities of the aluminium. It is not necessary to obtain the stresses and strains in the bearing area very accurately. A model is needed for the bearing, which accurately describes the resistance against flow through the bearing, but it does not have to give detailed

results in this area. To achieve this, a very coarse mesh is used to model the bearing. This model is constructed such, that it gives the same flow resistance as a more detailed reference model. This reference model will be discussed first, followed by a description of the equivalent bearing model.

5.4.1 Reference model

In Figure 5.2, the reference model is illustrated. It represents a 2D plane strain extrusion problem based on the geometry presented in Figure 5.1. The entrance of the bearing channel is modelled with a small rounding with a radius of 0.1 mm which complies to the bearings used in practise. Symmetry conditions are applied at the bottom of the mesh. The model consists of 4 node elements with selective reduced integration, also referred to as the $\overline{B}$-approach [16, 17], to prevent volume locking.

Friction is modelled along the dotted boundaries with a Coulomb friction law (friction coefficient $\mu = 0.5$). Since the normal stresses are high on this boundary, a stick condition applies. In the bearing channel, no friction occurs because the bearing is relieved. Only in the rounding at the start of the bearing does slipping friction actually occur. Since this area is small, the friction coefficient has almost no influence on the results.

A number of simulations were carried out with this model, varying extrusion speed and profile thickness. The results of these simulations are compared with the results of the equivalent bearing model in order to verify the accuracy of the equivalent model.

5.4.2 Construction of equivalent bearing model

The development of the equivalent bearing model was inspired by the following demands: the model should have fewer degrees of freedom compared to the detailed model, it should be easy and fast to mesh even for complex shapes of the section and its accuracy should not be reduced too much compared to the detailed model.

In order to reduce the number of degrees of freedom, the model should have significantly fewer elements in the bearing area. To simplify meshing it is convenient to use an automatic meshing algorithm. For the complex geometry associated with extrusion, these algorithms are only available for tetrahedron elements. Since linear tetrahedron elements are unsuitable for plastic flow calculations, quadratic elements are used. To avoid volume locking, selective reduced integration is used. A 3D mesh
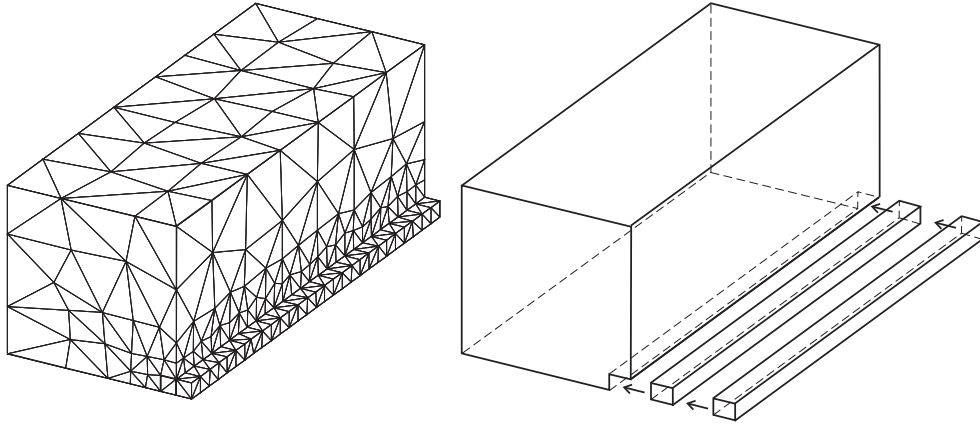
Figure 5.3: Equivalent bearing model for comparison with plane strain reference model and exploded view of the parts necessary for the construction of the triple nodes.
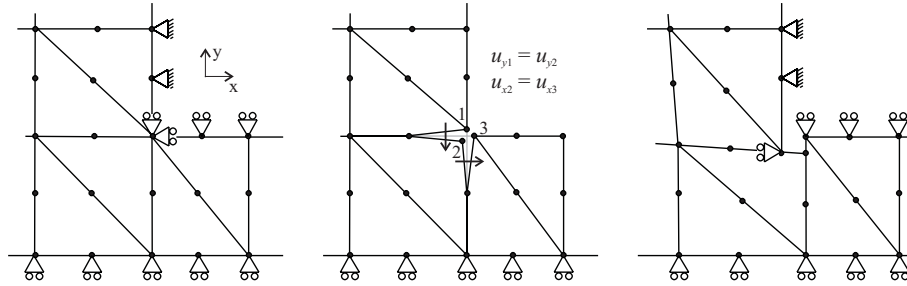

Figure 5.4: Triple node construction to model the corner of the bearing (left: locking corner node; middle: triple node construction; right: resulting displacement field).

is constructed corresponding to the 2D plane strain reference model. This model is illustrated in Figure 5.3.

The radius in front of the bearing cannot be modelled in the equivalent model, because this would significantly increase the number of elements in the bearing. Instead a sharp corner is modelled. However such a sharp corner exhibits locking effects, because of the boundary conditions on the perpendicular surfaces. This is illustrated in Figure 5.4 on the left. When only a limited number of elements are present in the bearing, this locking will affect the resistance in the bearing, effectively blocking a significant part of it. To avoid this a so-called triple node is used. The node at the corner is replaced by three separate nodes connected to the elements as illustrated in Figure 5.4 in the middle. The degrees of freedom of these nodes are connected to each other as indicated. The resulting displacement field is indicated on the right in Figure 5.4.

To obtain a mesh in 3D, similar in configuration to the mesh in Figure 5.4, it is convenient to separate the bearing geometry into three different parts as illustrated in Figure 5.3. The automatic meshing algorithm will create elements that conform to the boundaries of these parts. The nodes on the corner edge at the start of the bearing are split into three nodes. Then each node is reconnected to the elements in one of the three parts. Subsequently, the connections between the degrees of freedom of the nodes are generated.

5.4.3 Evaluating the results of the equivalent bearing model

To compare the equivalent bearing model to the 2D reference model a number of simulations have been performed varying the extrusion speed and profile thickness. In Figure 5.5, the pressure distribution in the reference model and the equivalent model are compared. They clearly show that a good agreement exist between the two models. Other results such as velocities and plastic strain rates give similar agreement.

In Figure 5.6 two graphs illustrating the average pressure on the inflow surface are plotted. In the left graph, the extrusion speed is varied and on the right, the profile thickness. Both graphs show that the pressure build-up in the equivalent model is slightly lower compared to the reference model. This is caused by the triple nodes which show a little less resistance to the flow compared to the rounded corner in the reference model. Since the difference is not very large it is accepted.
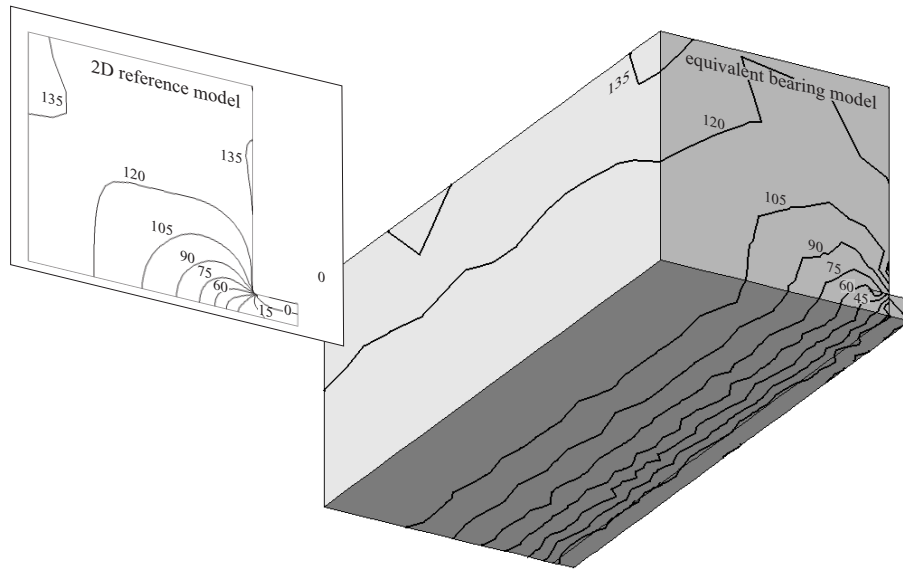
Figure 5.5: Pressure (MPa) in plane strain extrusion (left: reference model; right: equivalent bearing model).
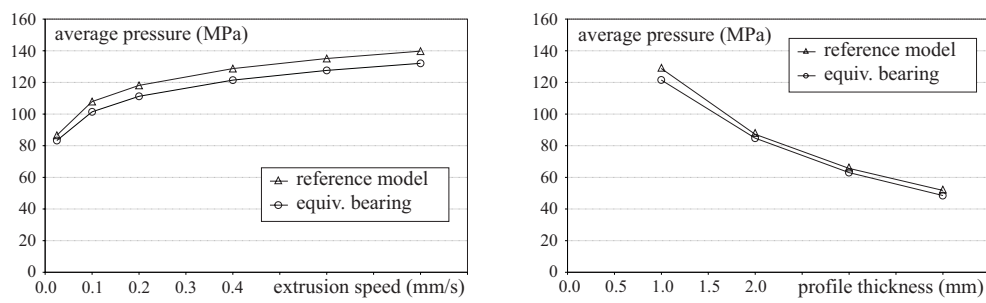

Figure 5.6: Average pressure on inflow edge for different extrusion speeds and profile thickness.
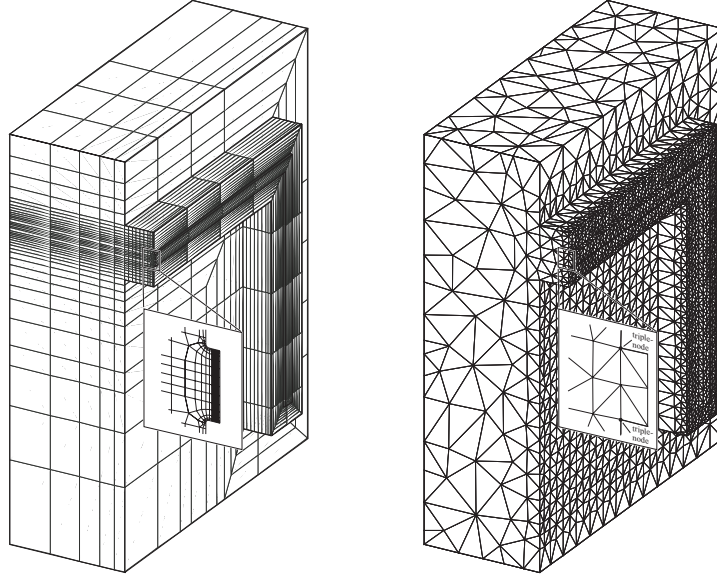
Figure 5.7: Model of extrusion of U-shaped profile (left: reference model; right: equivalent bearing model).
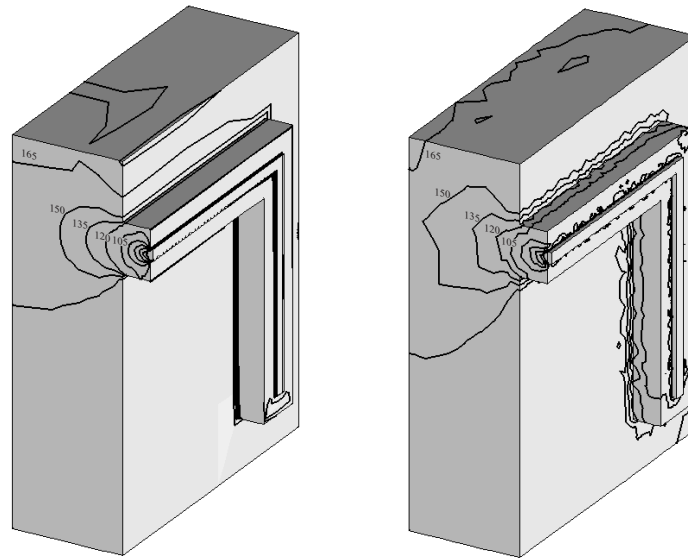
Figure 5.8: Pressure (MPa) for extrusion of U-shaped profile (left: reference model; right: equivalent bearing model).
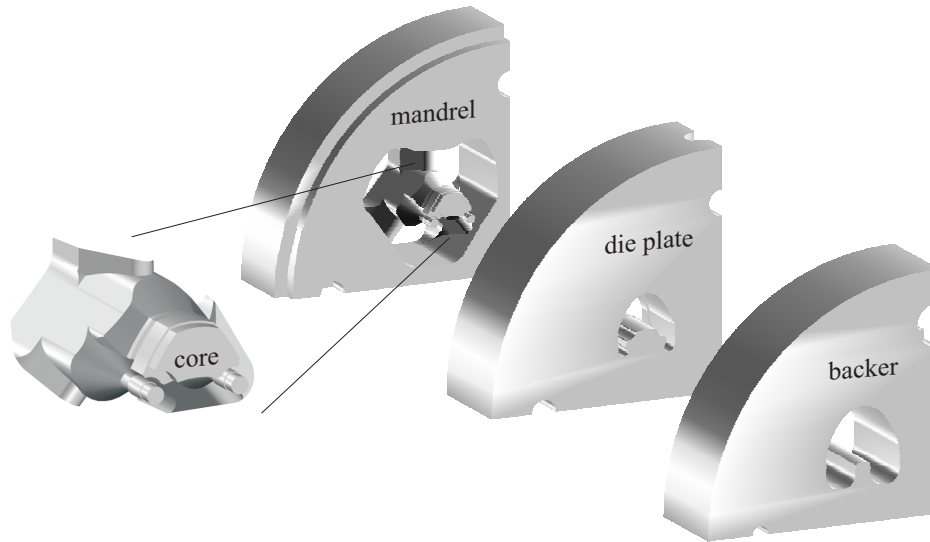
Figure 5.9: Example of a complex extrusion die.

A more complex comparison is performed to check the equivalent bearing model in
a more realistic extrusion problem. Figure 5.7 illustrates both the reference model
and the equivalent bearing model for the extrusion of a U-shaped profile (Figure 5.1).
Only half is modelled because of symmetry. Again a relieved bearing is modelled.
The reference model is based on a 2D cross-section which is extended to 3D along
the path of the profile. It consists of 8 node brick elements with selective reduced
integration to prevent volume locking. Boundary conditions are similar to the 2D
plain strain model.

The results of the U-profile are illustrated in Figure 5.8. Again, the pressure in the
equivalent bearing model is slightly underestimated compared to the reference model.
Near the bearing the results of the equivalent model are not very smooth due to
the coarse mesh in this area and the random orientation of the elements. Taking al
things into consideration, it is concluded that the equivalent bearing model is accurate
enough to provide an alternative way of modelling the bearing in simulations of the
entire extrusion process.
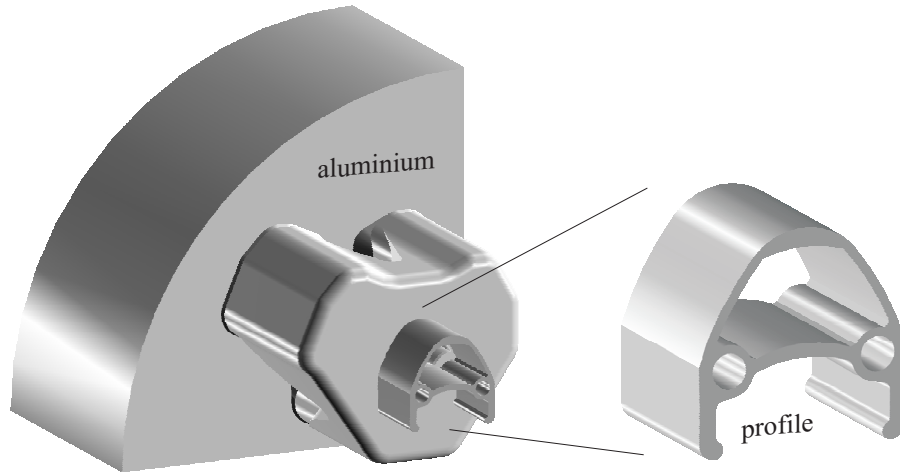
Figure 5.10: Aluminium geometry associated with the die from Figure 5.9.

5.5 Pre-processing

In simulations of extrusion, it is vital to have an efficient pre-processing method because of the complex shapes of extrusion dies. In Figure 5.9 a typical extrusion die is illustrated. It is a four-hole die used to produce the profile illustrated in Figure 5.10. The die is relatively complex, because of the multiple hollows in the profile and the variation in wall thickness. This die will be used as an example to illustrate the current capabilities in the area of extrusion simulations.

For simulation purposes it is necessary to have a completely defined 3D model of the geometry of the die and of the aluminium inside the die. When the die is designed using a 3D CAD system, the geometry created in the CAD system can be used for the generation of the FEM mesh. For the simulations presented here, the geometry of the die was obtained from the die producer. The geometry was made in the CAD application Pro/Engineer. The geometry of the aluminium can be derived easily by subtracting the geometry of the die from a solid cylindrical object. For the construction of the triple nodes, two parts, representing the profile, are separated from the geometry of the aluminium. The geometry of the aluminium is illustrated in Figure 5.10.

With the geometry of the model completely defined, the generation of the FEM model can start. This pre-processing for the aluminium flow simulation consists of the following steps:

- Meshing of the aluminium geometry.
- Applying boundary conditions on aluminium:
  - Prescribed displacement on the aluminium billet.
  - Symmetry conditions on the aluminium.
  - Stick conditions on the aluminium-die interface.
- Construction of triple nodes (illustrated in Figure 5.4):
  - Splitting corner nodes in three separate nodes.
  - Reconnecting the elements to the appropriate nodes.
  - Applying appropriate connections between nodal degrees of freedom.

For the stress analysis of the die, the following pre-processing steps must be carried out:

- Meshing of the die geometry.
- Applying boundary conditions on die:
  - Reaction forces on the aluminium-die interface (obtained from the results of the aluminium flow simulation).
  - Symmetry conditions on the die.
  - Support conditions on the die.

For meshing of complex 3D shapes adequate algorithms are available in most pre-processing applications. Since the aluminium simulation is separated from the die deformation calculation, both models could be constructed separately. However since the loads on the die are determined from the aluminium flow calculation, it is convenient when the mesh of die and aluminium are equal on the interface. In that case, the reaction forces calculated in the aluminium flow simulation can be directly applied to the die. To obtain a mesh that is equal on the interface, meshing of the geometry of aluminium and die is performed simultaneously. Meshing is performed in the CAD system Pro/Engineer which has a built-in meshing function. To obtain a suitable
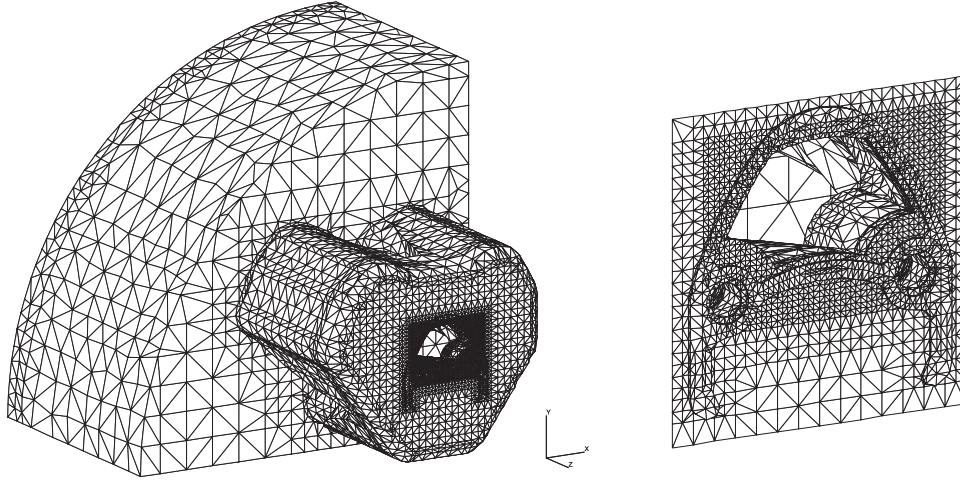
Figure 5.11: Finite element mesh of the aluminium geometry.

mesh, a local element size has to be applied at critical locations like the bearing area. This requires some trial and error and an experienced operator. In Figure 5.11 the mesh for the aluminium domain is illustrated.

Application of the boundary conditions to the FEM mesh is done manually in most pre-processing applications. However in the case of a complex extrusion die, the number of faces on which boundary conditions have to be applied is very high. In the example used here, the aluminium-die interface consists of approximately 200 surfaces. Applying a stick condition to all of these surfaces is a very time-consuming task. Manual construction of the triple nodes is even more difficult and time-consuming. To avoid this manual work, a specialised pre-processor was developed to automatically generate both the boundary conditions and the triple nodes. This pre-processor was developed within the Pro/Engineer CAD system. It provides a direct coupling between the geometry construction in Pro/Engineer and the simulations in the FEM code DiekA.

Summarizing it can be concluded that for generating a FEM model for a complex extrusion die like the one illustrated in Figure 5.9 it is essential to construct specialised tools that are able to do much of the manual pre-processing tasks. With these tools, pre-processing can be performed in a very efficient way without the risk of making errors. In the application developed for the simulations presented here the only task for the user is to apply local element sizes on critical areas of the geometry and to judge whether the automatically generated mesh is adequate for the simulation.

Figure 5.12: Pressure distribution on cross-section of the aluminium (MPa).

Figure 5.13: Effective stress on cross-section of the aluminium (MPa).

5.6 Results of the simulations

The simulation of the aluminium flow still takes a relatively long time. On a HP J5600 workstation it takes about 10 hours to obtain a stationary solution for the model described above. With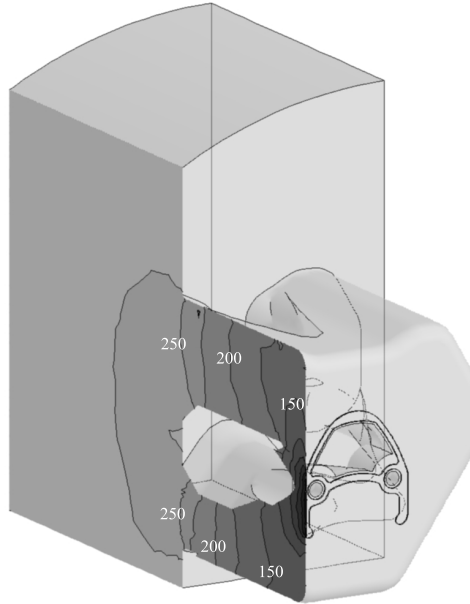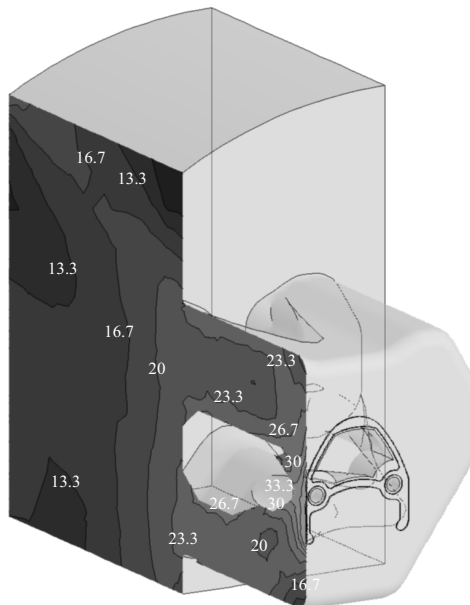 the results of this model, the forces on the die can be applied and a stress analysis of the die can be made. Since this is a linear elastic or a simple elasto-plastic calculation it requires considerably less time (approximately 30 minutes). First the results of the flow simulation will be discussed. In the second part of this section the results of the stress analysis are shown.

5.6.1 Flow simulation

A large variety of results can be obtained from the aluminium flow calculation. These include the velocities, stresses, equivalent plastic strain rate and reaction forces. The reaction forces are used in the stress analysis of the die. Also interesting are the velocities and the pressure distribution in the aluminium. The pressure on a cross-section through the die is shown in Figure 5.12. It clearly shows the pressure build-up from the bearing through the feeder holes to the billet. The effective stress (Von Mises) is shown in Figure 5.13. The effective stress is related directly to the plastic strain rate through (5.1).

To judge whether this die will perform adequately in practise, it is important to see the exit velocity of the profile over the cross-section of the profile, as illustrated in Figure 5.14. The results of the simulation represent the velocities at the start of the extrusion process. They give an indication of how the nose-end of the profile will look. From this figure it is clear that the thin middle part has a relative low exit velocity compared to the thicker parts. Based on these results the design of the bearing area can be modified to compensate for this velocity difference.

It is difficult to obtain a good experimental verification of the numerical results. However a rough comparison with the actual exit velocity can be obtained by looking at the nose-end of the profile. This nose-end is shown in Figure 5.15. The figure clearly shows that the distribution in exit velocity is comparable with the calculated result. A more elaborate experimental verification of the simulations was performed for a simple rectangular profile [15]. This verification showed a good agreement between experimental and numerical results.
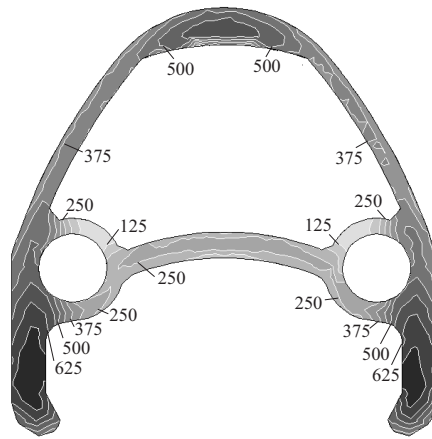
Figure 5.14: Exit velocity of the profile (mm/s).
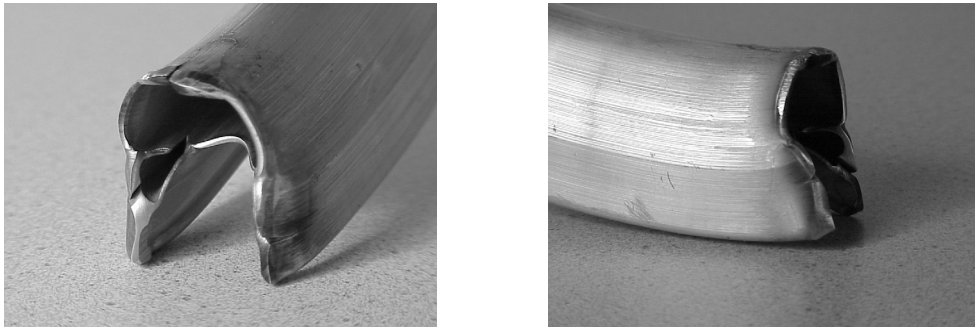
Figure 5.15: Nose-end of the profile.
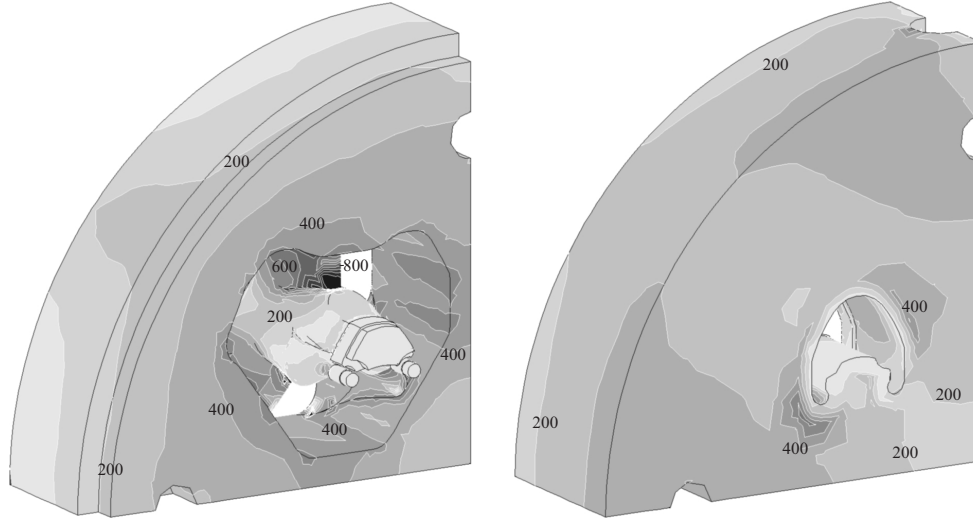
Figure 5.16: Effective stress in the mandrel and die plate (MPa).

5.6.2 Stress analysis

When the reaction forces on the aluminium-die interface are applied to the die, stresses in the die can be calculated. In Figure 5.16 the Von Mises stress on the mandrel and die plate are plotted. From these results it is clear that the legs are confronted with the highest stresses. Research aimed at improvement of the strength and stiffness of the die should be focussed on the design of the legs. Optimisation of the design of the legs was performed based on a simpler porthole die discussed elsewhere [18].

5.7 Discussion and concluding remarks

It is demonstrated that simulations of complex extrusion dies are feasible. It is difficult to estimate the accuracy of these calculations because it is nearly impossible to perform accurate measurements on the extrusion process in practise. However the results show good agreement with overall process characteristics like total extrusion pressure and exit velocity.

Two practical applications for the simulations can be considered. First of all, the simulations can be used to increase the general knowledge of the extrusion process and to derive design rules that can be used in practise. A second application is to use

the simulations directly in the design process of specific dies in order to improve the performance of these dies.

Design rules can be derived based on parameter studies on specific parts of the die design. This kind of approach has already been used successfully for the optimization of the shape of the legs used in porthole dies. At the moment, the influence of the dimensions of the core, the welding chamber and the legs on the exit velocity of the profile is investigated. The objective of this study is to derive general design rules for the design of porthole dies. This application of the simulations looks very promising and has the potential to improve the performance of extrusion dies considerably.

The direct application of simulations in the design process requires fast and robust simulation techniques. The simulations presented here have the ability to improve on the performance of dies and to reduce the number of trial pressings, but they still require considerable effort and a skilled user.

References

[1] G. Grasmo, K. Holthe, S. Støren, H. Valberg, R. Flatval, L. Hanssen, M. Lefstad, O. Lohne, T. Welo, R. Ørsund, and J. Herberg. Modelling of two-dimensional extrusion. In *Proc. 5th International Extrusion Technology Seminar*, pages 367–376, Wauconda, Illinois, 1992. Aluminum Association and Aluminum Extruders Council.

[2] Y. S. Kang and D. Y. Yang. Investigation into the thermo-viscoplastic finite element analysis of square die extrusion of square section with Lagrangian description. *Int. J. Mach. Tools Manufact.*, 36:907, 1996.

[3] L. Tong. *FE simulation of bulk forming processes with a mixed Eulerian-Lagrangian formulation*. PhD thesis, Swiss Federal Institute of Technology Zürich, Switserland, 1995.

[4] H. G. Mooi. *Finite element simulation of aluminium extrusion*. PhD thesis, University of Twente, The Netherlands, 1996.

[5] B. J. E. van Rens. *Finite element simulations of the aluminium extrusion process*. PhD thesis, Technical University Eindhoven, The Netherlands, 1999.

[6] J. Lof and J. Huétink. Isothermal elasto-viscoplastic FEM simulations of the extrusion of a thin aluminium tube. *Comp. Mater. Sci.*, 2000. submitted.

[7] J. Huétink. Analysis of metal forming processes based on a combined Eulerian-Lagrangian finite element formulation. In J. F. T. Pittman et al., editors, *Numerical Methods in Industrial Forming Processes*, pages 501–509. Pineridge Press, 1982.

[8] J. Huétink. *On the simulation of thermomechanical forming processes.* PhD thesis, University of Twente, The Netherlands, 1986.

[9] J. Huétink, P. T. Vreede, and J. van der Lugt. Progress in mixed Eulerian-Lagrangian finite element simulation of forming processes. *Int. J. Numer. Meth. Engng.*, 30:1441–1457, 1990.

[10] A. Huerta and W. K. Liu. Viscous flow with large free surface motion. *Comput. Methods Appl. Mech. Engrg.*, 69:277–324, 1988.

[11] W. K. Liu, H. Chang, J. Chen, and T. Belytschko. Arbitrary Lagrangian-Eulerian Petrov-Galerkin finite elements for nonlinear continua. *Comput. Methods Appl. Mech. Engrg.*, 68:259–310, 1988.

[12] J. Lof. Elasto-viscoplastic FEM simulations of the extrusion of the aluminium flow in the bearing area for extrusion of thin walled sections. *J. Mater. Proc. Tech.*, 2000. submitted.

[13] R. Akeret, H. Jung, and G. Scharf. *Atlas of hot working properties of nonferrous metals*, volume 1. Deutsche Gesellschaft für Metallkunde (DMG), 1978.

[14] J. van de Langkruis, W. H. Kool, C. M. Sellars, M. R. van der Winden, and S. van der Zwaag. The effect of β,β' and β'' precipitates in a homogenised AA6063 alloy on the hot deformability and the peak hardness. *Mat. Sci. Eng. A*, 2000. accepted for publication.

[15] J. van de Langkruis, J. Lof, W. H. Kool, S. van der Zwaag, and J. Huétink. Comparison of experimental AA6063 extrusion trials to 3D numerical simulations, using a general solute-dependent constitutive model. *Comp. Mat. Sci.*, 2000. accepted for publication.

[16] J. C. Nagtegaal, D. M. Parks, and J. R. Rice. On numerically accurate finite element solutions in the fully plastic range. *Comput. Methods Appl. Mech. Engrg.*, 4:113–135, 1974.

[17] T. J. R. Hughes. Generalization of selective reduced integration procedures to anisotropic and nonlinear media. *Int. J. Numer. Meth. Engng.*, 15:1413–1418, 1980.

[18] J. Lof, G. Klaseboer, J. Huétink, and P. T. G. Koenis. FEM simulations of aluminium extrusion using an elasto-viscoplastic material model. In *Proc. 7th International Extrusion Technology Seminar*, volume 2, pages 157–168, Wauconda, Illinois, 2000. Aluminum Association and Aluminum Extruders Council.

Chapter 6

Concluding remarks

In this final chapter, a reflection on the work presented in this thesis will be given. As stated in the introduction, the aim of this work is not only to develop numerical tools for the simulation of extrusion, but also to use these tools to increase knowledge of the extrusion process. In the first section of this chapter an overview of the developments in the area of numerical modelling is given. Some recommendations for further development are also discussed in this section. The practical application of the work is discussed in Section 6.2.

6.1 Current state of modelling

In this thesis some developments in the techniques used for the simulation of aluminium extrusion are presented. The work is mainly focussed on the following three areas: the simulation of the aluminium flow through the bearing area, the verification of extrusion simulations to experimental results and the development of a practical method to make simulations for complex sections. In Sections 6.1.1 to 6.1.3, the result of this work is briefly summarized. The final result of this work is a method to make simulations of the extrusion process for arbitrary sections. However in these simulations, not all aspects which play a role in the extrusion process are included, this is discussed in Section 6.1.4. Recommendations for further developments are given in Section 6.1.5.

6.1.1 Modelling the aluminium flow in the bearing area

The bearing area has a dominant influence on the characteristics of the extrusion process. However when making numerical simulations, it is also the most complex

part to model. To get a basic understanding of the phenomena that occur in the bearing, a detailed 2D model is developed. With this model, the influences of the elastic material behaviour, of friction and of the bearing geometry are investigated.

The results of this model lead to one important conclusion. The resistance in a parallel bearing channel is very sensitive to small changes in bearing geometry and process conditions. This conclusion has two far-reaching consequences: firstly, it is impossible to accurately predict the behaviour of a parallel bearing channel with numerical simulations and secondly, the behaviour of a parallel bearing in practise will be very unpredictable. The practical implications of this result will be discussed in more detail in Section 6.2. For the development of the simulation tools, the result is that attention is shifted from the simulation of parallel bearings to the simulation of relieved bearings.

6.1.2 Experimental verification of extrusion simulations

It is very difficult to verify the simulations of extrusion with experimental results, because of a number of reasons: First of all, it is necessary to have an accurate description of the material behaviour taking into account the solution state of the alloy components. Secondly, the experimental conditions have to be controlled precisely and modelled accurately in the simulation.

In order to obtain experimental verification of the numerical model, simulations were made of extrusion experiments conducted at Delft University of Technology. The numerical and experimental results of these extrusion experiments showed good agreement. The differences that exist can be attributed to the lack of material data for high strain rates and to dynamic precipitation that occurs under specific conditions. It is concluded that in principle simulation are sufficiently accuracy to provide quantitative information about the extrusion process. However in the industrial application of extrusion, only limited knowledge of, and control over, the exact process and material conditions is available. Consequently, it is not possible to obtain similar accuracy as found in the results presented in Chapter 4. Therefore it is concluded that the results of the simulations should be used mainly as qualitative indicators of the actual phenomena.

6.1.3   Development of an efficient method for the simulation of the extrusion process

For the simulation of complex sections, one of the most difficult problems is the creation of the FEM model. Not only meshing the complex geometries associated with extrusion, but also application of the boundary conditions can be a very time-consuming task when done inefficiently.

In Chapter 5 it was demonstrated that it is possible to make simulations of the extrusion of complex sections, without much effort. The bearing area is modelled with an equivalent bearing model. This model reduces the complexity of the FEM model in the bearing area considerably. The result of this is that both the calculation time and the meshing difficulties are reduced significantly. To minimize the manual work, a specialized pre-processor was developed within the CAD system Pro/Engineer. This pre-processor provides a direct link between the die design process in Pro/Engineer and the simulations in the FEM code DiekA.

The results of the model provide clear insight into the stresses and strain rates that occur within the aluminium during extrusion. It also provides a clear picture of the velocity of the material inside the die. Separate from the flow simulation, the deformation and stresses of the die can be calculated.

6.1.4   Limitations of the FEM model

The extrusion process is a transient process, because of the cyclic loading of the billet and the changing off the dies. Transient effects include the loading of an empty die, the reduction in billet length and the heating and cooling of the material during a billet cycle. To accurately model all these effects, transient calculations are necessary. However these kinds of calculations require unacceptably long calculation times. As an alternative, a stationary extrusion process can be simulated. The stationary solution gives the extrusion load at a certain billet length and it provides an upper limit for the temperature distribution.

In the simulations presented in this thesis, the stationary solution is not calculated directly, but by an incremental approach. Approximately 30 to 50 time increments are necessary to obtain a stationary solution. The result of this is that the efficiency of the calculation is less than optimal. This is especially the case for thermo-mechanical calculations. Therefore, the simulations have been limited to isothermal problems.

During the extrusion process, the temperature of the aluminium increases approximately 50° to 100°. A significant portion of this heating takes place inside the container. The rest occurs when the material flows through the die. Because the thermal conductivity in aluminium is high, it is expected that localised heating is limited. A significant increase in temperature is only expected in areas with extreme strain rates, such as the bearing. Since the material description is also unreliable in this area, because of the lack of experimentally determined material data for high strain rates, the results in this area should be considered with some reservation.

Furthermore, there are some limitations related to the pre-processing application. At present it is impossible to make a simulation in which the die deformation and flow simulation are coupled. It is also not possible to model the deformation of the profile after it leaves the die. However, the pre-processor can be extended to include these options.

6.1.5   Recommendations for further development

To enhance the possibilities of the simulation and to reduce the calculation time it is necessary to directly solve the stationary solution of the problem. In principle this is possible within the FEM application DiekA. However, very bad convergence behaviour is observed when this is attempted. The reason for this is the ill-conditioned system, resulting from a penalty approach to enforce plastic incompressibility in combination with the use of iterative solvers. Further research should focus on this point, because it has the potential to significantly reduce the calculation times of the flow simulations. In addition to this, it also makes the solution of the thermo-mechanical problem and the coupled aluminium flow - die deformation problem a lot more efficient.

If it turns out to be impossible to calculate the solution of the stationary problem directly, the thermal problem and the aluminium flow - die deformation problem could be solved decoupled from the flow problem. This might be a very efficient way to obtain a solution even compared with the direct calculation the stationary solution of the coupled problem.

Further development to the pre-processor in Pro/Engineer are necessary to include die deformation and profile deformation in the flow simulations. More attention could also be given to the meshing algorithm. At the moment the standard meshing algorithm of Pro/Engineer is used. While this gives good results, it still requires the manual application of element sizes in critical areas of the geometry.
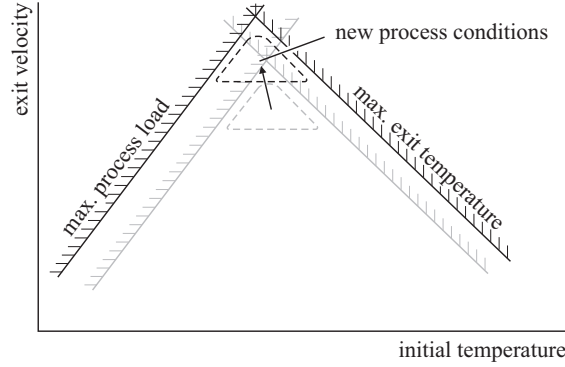
Figure 6.1: New optimised process conditions.

To obtain more quantitative results, it is necessary to know the process and material conditions more accurately. Especially the thermal aspects of the process and the mechanical properties of the extrudate at high strain rates have to be described well in order to obtain accurate results.

6.2 Application to extrusion practise

In the introduction of this thesis, a number of problems encountered in extrusion practise were identified. A major problem is the number of trial pressings that are necessary before dies can be used in practise. Another problem is the lack of knowledge, complicating the optimisation of the process conditions. In this section the advancements that have been made in solving these problems are discussed.

In Chapter 3, the reason for the unpredictable behaviour of extrusion dies was identified. It turns out that the use of parallel bearings, which is common in extrusion, is the cause of this behaviour. As an alternative for parallel bearings, it is suggested to use a relieved bearing. To control the exit velocity, a small sink-in can be placed before the bearing. Based on simulations of the bearing area a design rule was developed which can be used to design the sink-in geometry in order to obtain a uniform exit velocity of the profile [1]. This approach has been tested in practise with satisfactory results.

In order to better optimise process conditions for the extrusion process, quantitative results, including the thermal behaviour during an extrusion cycle, are necessary. The

109

results of the simulations are not accurate enough at the moment to be used in this way. However, with the insight gained from the simulations, it is possible to improve specific parts of the process. These improvements can lead to an expansion of the process window as illustrated in Figure 6.1. For example the introduction of a relieved bearing has reduced the process load and the heating because of friction. The result is that the limitations imposed by the maximum process load and the exit temperature are reduced. Another example of this is the improvement of the strength of porthole dies by optimising the cross-sectional shape of the legs [2].

With the development of the extrusion pre-processor in Pro/Engineer it has become possible to use simulations directly in the design process. Simulations can help to predict the exit velocities of the aluminium and the deformations and stresses in the die. Correction of the design is then possible before the die is actually manufactured. In principle this application has the potential to significantly improve the design of extrusion dies, although it has not yet been tested in practise.

References

[1] J. Lof, J. Huétink, and K.E. Nilsen. FEM simulations of the material flow in the bearing area of the aluminium extrusion process. In *Proc. 7th International Extrusion Technology Seminar*, volume 2, pages 211–222, Wauconda, Illinois, 2000. Aluminum Association and Aluminum Extruders Council.

[2] J. Lof, G. Klaseboer, J. Huétink, and P. T. G. Koenis. FEM simulations of aluminium extrusion using an elasto-viscoplastic material model. In *Proc. 7th International Extrusion Technology Seminar*, volume 2, pages 157–168, Wauconda, Illinois, 2000. Aluminum Association and Aluminum Extruders Council.

Appendix A

Basic theory

The simulations presented in this thesis were made with the finite element code DiekA. This is an Arbitrary Lagrangian Eulerian (ALE) code, specialised in the simulation of forming processes [1]. In this appendix the theoretical background of this FEM code is explained briefly. For a thorough treatment of continuum mechanics and the nonlinear finite element method, the reader is referred to the work of Belytscko, Liu and Moran [2].

A.1   Continuum mechanics

This section gives an overview of the continuum mechanics used to describe the motion and deformation of a body. Firstly, definitions of motion, deformation and stress are given. Then a brief overview of the relation between stresses and strains, the constitutive equations is given. Finally, the conservation laws are treated. For an elaborate treatment of continuum mechanics, the reader is referred to Malvern [3].

A.1.1   Kinematics

Consider a body in an initial configuration Ω_0, which is transformed to a current configuration Ω. The position of a material point in the initial configuration is given by $\mathbf{X}$. The vector $\mathbf{X}$ is called the Lagrangian or material coordinate. This vector does not change with time and can be considered a label for a material particle. The motion of the material particle is described as a transition from the initial configuration to the reference configuration.

$$\mathbf{x} = \phi\left(\mathbf{X}, t\right) \tag{A.1}$$
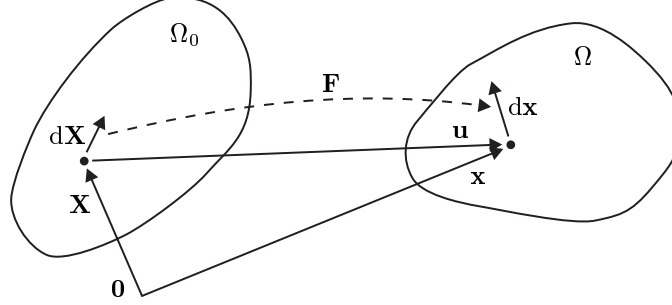
Figure A.1: Initial and current configurations of a body.

Where $\mathbf{x}$ is the position of material point $\mathbf{X}$ at time t. The vector $\mathbf{x}$ is called the Eulerian or spatial coordinate. The motion of the body is described by the function ϕ which maps the initial configuration onto the current configuration.

Two approaches are used to describe the deformation of the body. In the first approach, the independent variables are the the Lagrangian coordinates $\mathbf{X}$ and the time t. This approach is called the Lagrangian description. In the second approach the independent variables are the Eulerian coordinates $\mathbf{x}$ and the time t. This approach is called the Eulerian description.

The displacement of a material point is given by the difference between its initial and current positions.

$$\mathbf{u}\left(\mathbf{X}, t\right) = \phi\left(\mathbf{X}, t\right) - \phi\left(\mathbf{X}, 0\right) = \phi\left(\mathbf{X}, t\right) - \mathbf{X} \tag{A.2}$$

The velocity of a material point is defined as the material time derivative of the displacement $\mathbf{u}$.

$$\mathbf{v}\left(\mathbf{X}, t\right) = \frac{\mathrm{d}\left(\mathbf{u}\left(\mathbf{X}, t\right)\right)}{\mathrm{d}t} = \dot{\mathbf{u}}\left(\mathbf{X}, t\right) \tag{A.3}$$

A.1.2   Deformation

In order to describe the deformation of a body, the deformation gradient is defined (Figure A.1):

$$\mathbf{F} = \frac{\partial \phi\left(\mathbf{X}, t\right)}{\partial \mathbf{X}} = \mathbf{u}\overset{\leftarrow}{\nabla}_0 + \mathbf{I} \tag{A.4}$$

In order to describe the response of a body to deformation, some kind of measure of the amount of deformation, the strain, is necessary. To begin with the spatial velocity

112
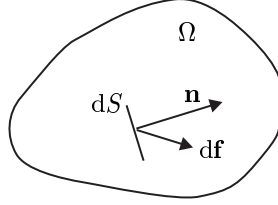
Figure A.2: Force acting on a surface.

gradient is defined as:

$$\mathbf{L} = \mathbf{v}\overleftarrow{\nabla} = \dot{\mathbf{F}} \cdot \mathbf{F}^{-1} \tag{A.5}$$

The velocity gradient $\mathbf{L}$ can be decomposed into a symmetric part and a skew-symmetric part:

$$\mathbf{L} = \mathbf{D} + \mathbf{W} \tag{A.6}$$

The symmetric part of the velocity gradient is called the rate of deformation tensor $\mathbf{D}$.

$$\mathbf{D} = \tfrac{1}{2}\left(\mathbf{v}\overleftarrow{\nabla} + \overrightarrow{\nabla}\mathbf{v}\right) \tag{A.7}$$

The skew-symmetric part is called the spin tensor $\mathbf{W}$.

$$\mathbf{W} = \tfrac{1}{2}\left(\mathbf{v}\overleftarrow{\nabla} - \overrightarrow{\nabla}\mathbf{v}\right) \tag{A.8}$$

The rate of deformation is a measure for the change in the length of an infinitesimal line segment $d\mathbf{x}$, i.e. the strain rate.

$$\begin{aligned}
\frac{d}{dt}\left(d\mathbf{x} \cdot d\mathbf{x}\right) &= 2d\mathbf{x} \cdot d\mathbf{v} = 2d\mathbf{x} \cdot \frac{\partial \mathbf{v}}{\partial \mathbf{x}} \cdot d\mathbf{x} = 2d\mathbf{x} \cdot \mathbf{L} \cdot d\mathbf{x} \\
&= 2d\mathbf{x} \cdot \left(\mathbf{D} + \mathbf{W}\right) \cdot d\mathbf{x} = 2d\mathbf{x} \cdot \mathbf{D} \cdot d\mathbf{x}
\end{aligned} \tag{A.9}$$

A.1.3 Stress definition

The Cauchy stress or true stress $\boldsymbol{\sigma}$, is defined as a force acting on a deformed surface as illustrated in Figure A.2:

$$dS\mathbf{n} \cdot \boldsymbol{\sigma} = d\mathbf{f} \tag{A.10}$$

113

In which $d\mathbf{f}$ is the force acting on an infinitesimal surface dS with normal $\mathbf{n}$. The Cauchy stress can be divided into a hydrostatic part and a deviatoric part. The hydrostatic stress or pressure is defined as:

$$p = -\tfrac{1}{3}\mathrm{tr}(\boldsymbol{\sigma}) \qquad\qquad\qquad (A.11)$$

The deviatoric stress is defined as:

$$\mathbf{s} = \boldsymbol{\sigma} + p\mathbf{I} \qquad\qquad\qquad (A.12)$$

A.1.4 Constitutive equations

The relation between stress and strain in a body is given by the constitutive equations. In this section a brief overview is given of these relations. A thorough treatment of the thermo-dynamical background of these equations was written by Mooi [4]. Rietman [5] gives more details on these equations from a materials science point of view.

Principle of frame indifference

According to the principle of frame indifference, the constitutive equations must be invariant to changes in reference frames. To obtain an objective expression for the stress rate, the Cauchy stress and the rate of deformation are written in corotational form. In this form, all components are expressed in an invariant coordinate frame:

$$\hat{\boldsymbol{\sigma}} = \mathbf{R}^{\mathrm{T}} \cdot \boldsymbol{\sigma} \cdot \mathbf{R} \qquad\qquad\qquad (A.13)$$

$$\hat{\mathbf{D}} = \mathbf{R}^{\mathrm{T}} \cdot \mathbf{D} \cdot \mathbf{R} \qquad\qquad\qquad (A.14)$$

Since only isotropic constitutive behaviour is considered, the orientation of the material is of no consequence. Consider a corotational coordinate system with an arbitrary orientation defined by the rotation tensor $\mathbf{Q}$ which has a spin $\mathbf{W}$. The rotation tensor $\mathbf{R}$ and its time derivative are defined as:

$$\mathbf{R} = \mathbf{Q} \qquad\qquad \dot{\mathbf{R}} = \mathbf{W} \cdot \mathbf{Q} \qquad\qquad\qquad (A.15)$$

The time derivative of the invariant corotational stress $\hat{\boldsymbol{\sigma}}$ is:

$$\begin{aligned}
\frac{d\hat{\boldsymbol{\sigma}}}{dt} &= \dot{\mathbf{R}}^{\mathrm{T}} \cdot \boldsymbol{\sigma} \cdot \mathbf{R} + \mathbf{R}^{\mathrm{T}} \cdot \dot{\boldsymbol{\sigma}} \cdot \mathbf{R} + \mathbf{R}^{\mathrm{T}} \cdot \boldsymbol{\sigma} \cdot \dot{\mathbf{R}} \\
&= \mathbf{Q}^{\mathrm{T}} \cdot (\dot{\boldsymbol{\sigma}} - \mathbf{W} \cdot \boldsymbol{\sigma} + \boldsymbol{\sigma} \cdot \mathbf{W}) \cdot \mathbf{Q}
\end{aligned} \qquad\qquad (A.16)$$

By rotating (A.16) back to the current reference frame, the objective Jaumann stress rate is defined:

$$\overset{\circ}{\boldsymbol{\sigma}} = \dot{\boldsymbol{\sigma}} - \mathbf{W} \cdot \boldsymbol{\sigma} + \boldsymbol{\sigma} \cdot \mathbf{W} \tag{A.17}$$

For anisotropic material behaviour, the orientation of the material has to be followed during the deformation. In this case the corotational reference frame should be related to the material orientation. Hence the rotation tensor $\mathbf{Q}$ should reflect the rotation of the material [6]. For isotropic material, the orientation of the material is of no consequence. Hence the rotation $\mathbf{Q}$ can be chosen equal to the unity tensor $\mathbf{I}$. As a result, the corotational stress $\hat{\boldsymbol{\sigma}}$ and strain rate $\hat{\mathbf{D}}$ are equal to their non-rotated counterparts $\boldsymbol{\sigma}$ and $\mathbf{D}$.

Rate equations

In plasticity it is not possible to define the relation between stress and strain directly. As a consequence, the constitutive equations are generally defined as a relation between stress rate and strain rate. A first step in the definition of the constitutive relation is the assumption that the strain rate can be split into an elastic part and a (visco)plastic part:

$$\mathbf{D} = \mathbf{D}^e + \mathbf{D}^{vp} \tag{A.18}$$

In the case of metal plasticity, the elastic deformations are generally small. The elastic response to deformation is given by the generalised Hooke's law:

$$\overset{\circ}{\boldsymbol{\sigma}} = \mathbf{E} \colon \mathbf{D}^e - \boldsymbol{\sigma} \operatorname{tr}(\mathbf{D}) \tag{A.19}$$

With $\mathbf{E}$ the 4$^{\text{th}}$-order linear elastic tensor. The plastic strain rate can be written as the product of a scalar value $\dot{\lambda}$ which determines the magnitude and a tensor $\mathbf{m}$ which determines the direction of the plastic flow.

$$\mathbf{D}^p = \dot{\lambda}\mathbf{m} \tag{A.20}$$

The behaviour of the material in the plastic domain is governed by a limit function $g(\boldsymbol{\sigma}, \mathbf{q})$. This function gives a relation between the stress in the material and the state variables $\mathbf{q}$ when the material is in the plastic domain. The conditions of the material can be formally written using the Kuhn-Tucker conditions:

$$g \leq 0 \, , \qquad \dot{\lambda} \geq 0 \, , \qquad g\dot{\lambda} = 0 \tag{A.21}$$

When the material is in the elastic state, the plastic multiplier $\dot{\lambda}$ is equal to zero and hence the plastic strain rate (A.20) is zero. If the material is in the plastic state, the limit function g is zero, and consequently its time derivative is also equal to zero. This is known as the consistency condition:

$$\dot{g} = 0 \tag{A.22}$$

In the case of perfect plasticity, the consistency condition can be elaborated as:

$$\dot{g} = \frac{\partial g}{\partial \boldsymbol{\sigma}} : \overset{\circ}{\boldsymbol{\sigma}} = \mathbf{n}^{\mathrm{T}} : \overset{\circ}{\boldsymbol{\sigma}} = 0 \tag{A.23}$$

In which $\mathbf{n}$ is normal to the surface defined by $g = 0$ at the current stress point. Combining (A.19-A.23) an explicit expression for the relation between stress rate and strain rate can be obtained:

$$\overset{\circ}{\boldsymbol{\sigma}} = \left(\mathbf{E} - \frac{\mathbf{E} : \mathbf{m} \mathbf{n}^{\mathrm{T}} : \mathbf{E}}{\mathbf{n}^{\mathrm{T}} : \mathbf{E} : \mathbf{m}} \right) : \mathbf{D} - \boldsymbol{\sigma} \mathrm{tr}\,(\mathbf{D}) \tag{A.24}$$

For hardening plasticity and viscoplasticity a similar approach can be used to find an relation between stress rate and strain rate. In general, this can be expressed as:

$$\overset{\circ}{\boldsymbol{\sigma}} = \mathbf{C} : \mathbf{D} - \boldsymbol{\sigma} \mathrm{tr}\,(\mathbf{D}) \tag{A.25}$$

The second term in this equation is often neglected for metal plasticity, as volume changes are very small for metals. However, since this term cancels out in the finite element formulation it is left here.

A.1.5   Conservation laws

A group of fundamental relations of continuum mechanics arises from the conservation laws. These relations must always be satisfied by physical systems. The first relation is the conservation of mass, which states that changes in density ρ are equal but opposite to changes in the volume of the continuum:

$$\dot{\rho} + \rho \vec{\nabla} \cdot \mathbf{v} = 0 \tag{A.26}$$

The second relation is the conservation of momentum, also referred to as the equilibrium equation:

$$\vec{\nabla} \cdot \boldsymbol{\sigma} + \rho \mathbf{b} = \rho \dot{\mathbf{v}} \tag{A.27}$$

116

In which **b** are the body forces. The final relation is the conservation of energy, which is the first law of thermodynamics:

$$\rho \dot{u} = \boldsymbol{\sigma} : \mathbf{D} - \mathbf{q} \cdot \overset{\leftarrow}{\nabla} + \rho r \tag{A.28}$$

In which u is the specific internal energy, **q** the internal heat flux and r a specific heat source.

A.2 Finite element formulation

The equations governing the deformation of a body as described in the previous section can generally not be solved analytically. To obtain an approximate solution, the finite element method is used. For an elaborate treatment of the finite element method, the reader is referred to Zienkiewicz and Taylor [7].

The starting point for defining the finite element formulation is the strong form of the equilibrium equation (A.27). If we consider a body Ω with boundary Γ and neglect inertia forces, the equilibrium equation can be expressed as:

$$\begin{aligned} \vec{\nabla} \cdot \boldsymbol{\sigma} + \rho \mathbf{b} &= 0 && \text{in} && \Omega \\ \boldsymbol{\sigma} \cdot \mathbf{n} &= \mathbf{t} && \text{on} && \Gamma_t \end{aligned} \tag{A.29}$$

In which $\mathbf{b}$ are the body forces and $\mathbf{t}$ are forces that act on part of the boundary Γ_t. The strong form of the equilibrium equation can be transformed to the weak form, given by:

$$\int_\Omega \delta \mathbf{w} \cdot \left(\vec{\nabla} \cdot \boldsymbol{\sigma} + \rho \mathbf{b} \right) d\Omega = 0 \qquad \forall \quad \delta \mathbf{w} \tag{A.30}$$

Applying Gauss theorem, the weak form of the equilibrium equation can be written as:

$$\int_\Omega \left(\delta \mathbf{w} \overleftarrow{\nabla} \right) : (\boldsymbol{\sigma}) \, d\Omega = \int_\Omega \delta \mathbf{w} \cdot (\rho \mathbf{b}) \, d\Omega + \int_{\Gamma_t} \delta \mathbf{w} \cdot \mathbf{t} d\Gamma_t \qquad \forall \quad \delta \mathbf{w} \tag{A.31}$$

A.2.1 Finite element discretisation (spatial discretisation)

To obtain a solution for the equilibrium equation, the current domain Ω is subdivided into elements Ω_e. Integrals are evaluated over these elements and subsequently, the contributions of all the elements are added to a large system, representing the whole domain. The elements are connected by nodes located on the boundaries of the elements. The motion of Ω can be approximated by:

$$\mathbf{x} = \phi\left(\mathbf{X}, t\right) = \mathbf{x}_I\left(t\right) N_I\left(\mathbf{X}\right) \tag{A.32}$$

Where N_I are the interpolation functions and $\mathbf{x}_I$ is the position vector of node I and assuming a summation over I. The displacement field (A.2) is approximated by:

$$\mathbf{u}\left(\mathbf{X}, t\right) = \left(\mathbf{x}_I\left(t\right) - \mathbf{X}_I\right) N_I\left(\mathbf{X}\right) = \mathbf{u}_I\left(t\right) N_I\left(\mathbf{X}\right) \tag{A.33}$$

Where $\mathbf{u}_I$ are the nodal displacements. The velocity field (A.3) is obtained by taking the material time derivative of the displacement field:

$$\mathbf{v}\left(\mathbf{X}, t\right) = \dot{\mathbf{u}}_I\left(t\right) N_I\left(\mathbf{X}\right) = \mathbf{v}_I\left(t\right) N_I\left(\mathbf{X}\right) \tag{A.34}$$

With $\mathbf{v}_I$ the nodal velocities. The velocity gradient (A.5) can be written as:

$$\mathbf{L} = \mathbf{v}\overset{\leftarrow}{\nabla} = \mathbf{v}_I N_I \overset{\leftarrow}{\nabla} \tag{A.35}$$

The symmetric part of the velocity gradient, the rate of deformation tensor (A.7) is defined as:

$$\mathbf{D} = \tfrac{1}{2}\left(\mathbf{L} + \mathbf{L}^{\mathrm{T}}\right) = \tfrac{1}{2}\left(\mathbf{v}_I N_I \overset{\leftarrow}{\nabla} + \overset{\rightarrow}{\nabla} N_I^{\mathrm{T}} \mathbf{v}_I^{\mathrm{T}}\right) = \mathbf{B}_I \mathbf{v}_I \tag{A.36}$$

Galerkin

Following a standard Galerkin approach, the class of weighting functions for which the weak form of the equilibrium equation (A.31) must be satisfied, is limited to functions which can be written as:

$$\delta\mathbf{w} = \delta\mathbf{v}_I N_I \tag{A.37}$$

Substituting the above into (A.31):

$$\int_\Omega \delta\mathbf{v}_I N_I \overset{\leftarrow}{\nabla} : \boldsymbol{\sigma}\,\mathrm{d}\Omega = \int_\Omega \delta\mathbf{v}_I N_I \cdot \left(\rho\mathbf{b}\right)\mathrm{d}\Omega + \int_{\Gamma_t} \delta\mathbf{v}_I N_I \cdot \mathbf{t}\mathrm{d}\Gamma_t \qquad \forall\delta\mathbf{v}_I \tag{A.38}$$

Which implies:

$$\int_\Omega N_I \overset{\leftarrow}{\nabla} : \boldsymbol{\sigma}\,\mathrm{d}\Omega = \int_\Omega N_I \cdot \left(\rho\mathbf{b}\right)\mathrm{d}\Omega + \int_{\Gamma_t} N_I \cdot \mathbf{t}\mathrm{d}\Gamma_t \tag{A.39}$$

This is the discretised equation that is solved in the finite element formulation. It can be written more conveniently by defining an internal and an external force vector:

$$\begin{aligned} \mathbf{f}_I^{int} &= \int_\Omega N_I \overset{\leftarrow}{\nabla} : \boldsymbol{\sigma}\,\mathrm{d}\Omega \\ \mathbf{f}_I^{ext} &= \int_\Omega N_I \cdot \left(\rho\mathbf{b}\right)\mathrm{d}\Omega + \int_{\Gamma_t} N_I \cdot \mathbf{t}\mathrm{d}\Gamma_t \end{aligned} \tag{A.40}$$

Equilibrium in the discretised problem requires:

$$\mathbf{f}_I^{int} = \mathbf{f}_I^{ext} \tag{A.41}$$

A.2.2 Incremental formulation (time discretisation)

To evaluate the deformation of the body Ω, the time domain of interest is subdivided into a number of time increments. Within each time increment the velocities are assumed to be constant.

$$\mathbf{v}_I = \frac{\Delta \mathbf{u}_I}{\Delta t} \tag{A.42}$$

Where $\Delta \mathbf{u}_I$ are the incremental nodal displacements and Δt is the time increment. At the end of each increment the global system must be in equilibrium. This requires the solution of the non-linear equation (A.41). Adopting an updated Lagrangian approach, the reference configuration is defined as the configuration at the start of the increment Ω_n.

The strain increment is approximated by integration of the rate of deformation using a midpoint rule:

$$\Delta \boldsymbol{\varepsilon} = \int_{t_n}^{t_{n+1}} \mathbf{D} \mathrm{d}t \approx \tfrac{1}{2} \left(\Delta \mathbf{u}_I N_I \overleftarrow{\nabla}_m + \overrightarrow{\nabla}_m N_I \Delta \mathbf{u}_I \right) \tag{A.43}$$

The rotation during the increment is approximated by integration of the spin tensor:

$$\mathbf{Q} \approx \mathbf{I} + \int_{t_n}^{t_{n+1}} \mathbf{W} \mathrm{d}t \approx \mathbf{I} + \tfrac{1}{2} \left(\Delta \mathbf{u}_I N_I \overleftarrow{\nabla}_m - \overrightarrow{\nabla}_m N_I \Delta \mathbf{u}_I \right) \tag{A.44}$$

Integration of the constitutive model

To obtain an expression for the internal force vector, the constitutive equation has to be integrated over the time increment. The constitutive equation is integrated in a coordinate frame half-way between the reference frame and the current frame, defined by the rotation tensor $\sqrt{\mathbf{Q}}$. The new stress is calculated as:

$$\boldsymbol{\sigma}_{n+1} = \sqrt{\mathbf{Q}} \cdot \left(\sqrt{\mathbf{Q}} \cdot \boldsymbol{\sigma}_n \cdot \sqrt{\mathbf{Q}^{\mathrm{T}}} + \Delta \boldsymbol{\sigma} \right) \cdot \sqrt{\mathbf{Q}^{\mathrm{T}}} \tag{A.45}$$

An expression for the stress increment can be obtained by integration of the constitutive equation:

$$\Delta \boldsymbol{\sigma} = \int_{t_n}^{t_{n+1}} \overset{\circ}{\boldsymbol{\sigma}} \mathrm{d}t \tag{A.46}$$

This integration is approximated with a return mapping algorithm as explained in Chapter 2 of this thesis.

Iterative procedure

Since the equilibrium equation (A.41) is non-linear, it is solved by an iterative procedure. Generally, a Newton-Raphson method gives the best convergence.

$$\mathbf{g}_I \left(\Delta \mathbf{u}_I \right) = \mathbf{f}_I^{int} \left(\Delta \mathbf{u}_I \right) - \mathbf{f}_I^{ext} \left(\Delta \mathbf{u}_I \right) = 0 \tag{A.47}$$

$$\Delta \mathbf{u}_I^{i+1} = \Delta \mathbf{u}_I^i + \delta \mathbf{u}_I \tag{A.48}$$

With:

$$\delta \mathbf{u}_I = \mathbf{K}_i^{-1} \mathbf{g}_I^i \tag{A.49}$$

Where $\mathbf{K}_i$ follows from the linearisation of g_I around $\Delta \mathbf{u}_I^i$:

$$\mathbf{g}_I \left(\Delta \mathbf{u}_I^i + \delta \mathbf{u}_I \right) \stackrel{lin}{\approx} \mathbf{g}_I \left(\Delta \mathbf{u}_I^i \right) + \mathbf{K}_i \delta \mathbf{u}_I \tag{A.50}$$

A.2.3   Linearisation of the equilibrium equation

For each iteration in the Newton-Raphson process, the equilibrium equation has to be linearised around the current solution. In the simulations presented in this thesis, the external force vector is constant. Hence the linear variation of this vector $\delta \mathbf{f}^{ext}$ is zero. In the remainder of this section, an expression for the linear variation of the internal force vector $\delta \mathbf{f}^{int}$ is derived.

Since an updated Lagrangian method is used, the configuration at the end of the previous increment (step n) is used as reference configuration. The deformation gradient $\mathbf{F}_n$ maps the configuration of step n to the current configuration (step $n+1$). To begin with, the expression for the internal force vector (A.40) is transformed from the current configuration Ω to the reference configuration Ω_n:

$$\begin{aligned}
\mathbf{f}_I^{int} &= \int_{\Omega_n} \left(N_I \overleftarrow{\nabla}_n \cdot \mathbf{F}_n^{-1} \right) : \boldsymbol{\sigma} \det \left(\mathbf{F}_n \right) \mathrm{d}\Omega_n \\
&= \int_{\Omega_n} N_I \overleftarrow{\nabla}_n : \left(\mathbf{F}_n^{-1} \cdot \boldsymbol{\sigma} \right) \det \left(\mathbf{F}_n \right) \mathrm{d}\Omega_n
\end{aligned} \tag{A.51}$$

Linearisation of the factor $\det \left(\mathbf{F}_n \right)$ yields:

$$\begin{aligned}
\det \left(\mathbf{F}_n \right) = \det \left(\mathbf{F}_n^i + \delta \mathbf{F} \right) &= \det \left(\mathbf{F}_n^i \cdot \left(\mathbf{I} + \left(\mathbf{F}_n^i \right)^{-1} \delta \mathbf{F} \right) \right) \\
&= \det \left(\mathbf{F}_n^i \right) \det \left(\mathbf{I} + \left(\mathbf{F}_n^i \right)^{-1} \delta \mathbf{F} \right) \\
&\stackrel{lin}{\approx} \det \left(\mathbf{F}_n^i \right) \left(1 + \left(\mathbf{F}_n^i \right)^{-1} : \delta \mathbf{F} \right)
\end{aligned} \tag{A.52}$$

Linearisation of the factor $(\mathbf{F}_n^{-1} \cdot \boldsymbol{\sigma})$ yields:

$$
\begin{aligned}
\mathbf{F}_n^{-1} \cdot \boldsymbol{\sigma} &= \left(\mathbf{F}_n^i + \delta \mathbf{F} \right)^{-1} \cdot \left(\boldsymbol{\sigma}^i + \delta \boldsymbol{\sigma} \right) \\
&\overset{lin}{\approx} \left(\mathbf{F}_n^i \right)^{-1} \cdot \boldsymbol{\sigma}^i - \left(\mathbf{F}_n^i \right)^{-1} \cdot \delta \mathbf{F} \cdot \left(\mathbf{F}_n^i \right)^{-1} + \left(\mathbf{F}_n^i \right)^{-1} \cdot \delta \boldsymbol{\sigma}
\end{aligned} \tag{A.53}
$$

Substituting equations A.52, A.53 into equation A.51 and linearising gives:

$$
\begin{aligned}
\mathbf{f}_I^{int} &= \int_{\Omega_n} N_I \overleftarrow{\nabla}_n : \left(\left(\mathbf{F}_n^i \right)^{-1} \cdot \boldsymbol{\sigma}^i + \delta \mathbf{F}^{-1} \cdot \boldsymbol{\sigma}^i + \left(\mathbf{F}_n^i \right)^{-1} \cdot \delta \boldsymbol{\sigma} \right) \\
&\qquad\qquad \det \left(\mathbf{F}_n^i \right) \left(1 + \left(\mathbf{F}_n^i \right)^{-1} : \delta \mathbf{F} \right) \mathrm{d}\Omega_n \\
&\overset{lin}{\approx} \int_{\Omega_n} N_I \overleftarrow{\nabla}_n : \left(\left(\mathbf{F}_n^i \right)^{-1} \cdot \boldsymbol{\sigma}^i \right) \det \left(\mathbf{F}_n^i \right) \mathrm{d}\Omega_n \\
&\qquad + \int_{\Omega_n} N_I \overleftarrow{\nabla}_n : \left(\left(\mathbf{F}_n^i \right)^{-1} \cdot \boldsymbol{\sigma}^i \cdot \left(\left(\mathbf{F}_n^i \right)^{-1} : \delta \mathbf{F} \right) \right. \\
&\qquad \left. + \delta \mathbf{F}^{-1} \cdot \boldsymbol{\sigma}^i + \left(\mathbf{F}_n^i \right)^{-1} \cdot \delta \boldsymbol{\sigma} \right) \det \left(\mathbf{F}_n^i \right) \mathrm{d}\Omega_n
\end{aligned} \tag{A.54}
$$

The linear variation of the internal force vector is the second term in the above equation:

$$
\begin{aligned}
\delta \mathbf{f}_I^{int} &= \int_{\Omega_n} N_I \overleftarrow{\nabla}_n : \left(\mathbf{F}_n^i \right)^{-1} \cdot \left(\boldsymbol{\sigma}^i \cdot \left(\left(\mathbf{F}_n^i \right)^{-1} : \delta \mathbf{F} \right) \right. \\
&\qquad \left. - \delta \mathbf{F} \cdot \left(\mathbf{F}_n^i \right)^{-1} \cdot \boldsymbol{\sigma}^i + \delta \boldsymbol{\sigma} \right) \det \left(\mathbf{F}_n^i \right) \mathrm{d}\Omega_n
\end{aligned} \tag{A.55}
$$

Which can be transformed back to the current configuration Ω:

$$
\delta \mathbf{f}_I^{int} = \int_{\Omega} N_I \overleftarrow{\nabla} : \left(\boldsymbol{\sigma}^i \cdot \left(\left(\mathbf{F}_n^i \right)^{-1} : \delta \mathbf{F} \right) - \delta \mathbf{F} \cdot \left(\mathbf{F}_n^i \right)^{-1} \cdot \boldsymbol{\sigma}^i + \delta \boldsymbol{\sigma} \right) \mathrm{d}\Omega \tag{A.56}
$$

Since $\mathbf{L}$ is constant in an increment, the first term in (A.56) can be rewritten as:

$$
\boldsymbol{\sigma}^i \cdot \left(\left(\mathbf{F}_n^i \right)^{-1} : \delta \mathbf{F} \right) = \boldsymbol{\sigma}^i \cdot \mathbf{I} : \delta \mathbf{L} \Delta t = \boldsymbol{\sigma}^i \cdot \mathrm{tr} \left(\delta \mathbf{D} \Delta t \right) \tag{A.57}
$$

The second term in (A.56) can be rewritten as:

$$
\delta \mathbf{F} \cdot \left(\mathbf{F}_n^i \right)^{-1} \cdot \boldsymbol{\sigma}^i = \delta \mathbf{L} \Delta t \cdot \boldsymbol{\sigma}^i \tag{A.58}
$$

Using the above two expressions in (A.56) the following is obtained:

$$
\delta \mathbf{f}_I^{int} = \int_{\Omega} N_I \overleftarrow{\nabla} : \left(\boldsymbol{\sigma}^i \cdot \mathrm{tr} \left(\delta \mathbf{D} \Delta t \right) - \delta \mathbf{L} \Delta t \cdot \boldsymbol{\sigma}^i + \delta \boldsymbol{\sigma} \right) \mathrm{d}\Omega \tag{A.59}
$$

An expression for $\delta \boldsymbol{\sigma}$ follows from the constitutive law that is used to model the material. For now it will be assumed that the corotational rate of the stress can be expressed in the general form (A.25):

$$
\overset{\circ}{\boldsymbol{\sigma}} = \dot{\boldsymbol{\sigma}} - \mathbf{W} \cdot \boldsymbol{\sigma} + \boldsymbol{\sigma} \cdot \mathbf{W} = \mathbf{C} : \mathbf{D} - \boldsymbol{\sigma} \mathrm{tr} \left(\mathbf{D} \right) \tag{A.60}
$$

This relation is integrated to obtain an expression for the stress increment. This is integration is elaborated on in Chapter 2 of this thesis. The linear variation of $\Delta\boldsymbol{\sigma}$ can be expressed as:

$$\delta\boldsymbol{\sigma} = \mathbf{C}^* : \delta\mathbf{D}\Delta t - \boldsymbol{\sigma}^i tr\left(\delta\mathbf{D}\Delta t\right) + \delta\mathbf{W}\Delta t \cdot \boldsymbol{\sigma}^i - \boldsymbol{\sigma}^i \cdot \delta\mathbf{W}\Delta t \tag{A.61}$$

Where $\mathbf{C}^*$ is the consistent tangent. Substituting this into (A.59) results in:

$$\delta\mathbf{f}_I^{int} = \int_\Omega N_I \overleftarrow{\nabla} : \left(-\delta\mathbf{L}\Delta t \cdot \boldsymbol{\sigma}^i + \mathbf{C}^* : \delta\mathbf{D}\Delta t + \delta\mathbf{W}\Delta t \cdot \boldsymbol{\sigma}^i - \boldsymbol{\sigma}^i \cdot \delta\mathbf{W}\Delta t\right) \mathrm{d}\Omega \tag{A.62}$$

Which can be rewritten with (A.6):

$$\delta\mathbf{f}_I^{int} = \int_\Omega N_I \overleftarrow{\nabla} : \left(\mathbf{C}^* : \delta\mathbf{D}\Delta t - \delta\mathbf{D}\Delta t \cdot \boldsymbol{\sigma}^i - \boldsymbol{\sigma}^i \cdot \delta\mathbf{D}\Delta t + \delta\mathbf{L}\Delta t \cdot \boldsymbol{\sigma}^i\right) \mathrm{d}\Omega \tag{A.63}$$

With (A.35) and (A.36) the following expressions can be derived:

$$\delta\mathbf{L}\Delta t = \mathbf{N}_I \overleftarrow{\nabla} \delta\mathbf{u}_I$$
$$\delta\mathbf{D}\Delta t = \mathbf{B}_I \delta\mathbf{u}_I \tag{A.64}$$

Which gives:

$$\delta\mathbf{f}_I^{int} = \int_\Omega N_I \overleftarrow{\nabla} : \left(\left(\mathbf{C}^* - \mathbf{H} \cdot \boldsymbol{\sigma}^i - \boldsymbol{\sigma}^i \cdot \mathbf{H}\right) : \mathbf{B}_I + \left(\mathbf{H} \cdot \boldsymbol{\sigma}^i\right) : \mathbf{N}_I \overleftarrow{\nabla}\right) \mathrm{d}\Omega \delta\mathbf{u}_I \tag{A.65}$$

With $\mathbf{H}$ is the 4$^{\text{th}}$-order unity tensor, this can be simplified to:

$$\delta\mathbf{f}_I^{int} = \left(\int_\Omega \mathbf{B}_I^{\mathrm{T}} : \left(\mathbf{C}^* - \mathbf{H} \cdot \boldsymbol{\sigma}^i - \boldsymbol{\sigma}^i \cdot \mathbf{H}\right) : \mathbf{B}_I \mathrm{d}\Omega \right.$$
$$\left. + \int_\Omega N_I \overleftarrow{\nabla} : \left(\mathbf{H} \cdot \boldsymbol{\sigma}^i\right) : \mathbf{N}_I \overleftarrow{\nabla} \mathrm{d}\Omega\right) \delta\mathbf{u}_I \tag{A.66}$$

This expression defines the matrix K_i, which is used in the Newton-Raphson algorithm for solving the non-linear system.
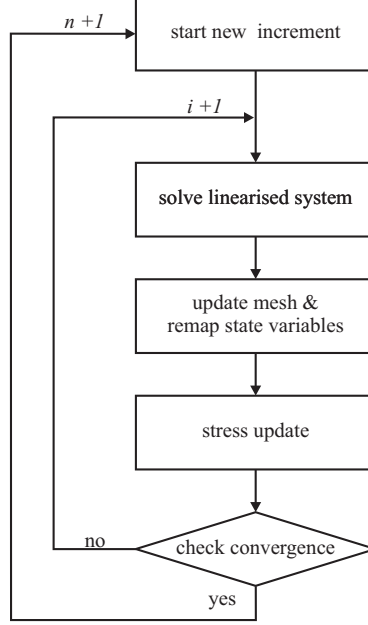
Figure A.3: Flow chart of semi-coupled ALE method.

A.2.4   Arbitrary Lagrangian Eulerian method

When using an updated Lagrangian description, distortions in the element mesh may occur when large deformations are modelled. This reduces the accuracy of the simulation and may eventually lead to loss of convergence. With a Eulerian description these problems are avoided, but it is difficult to model free surfaces with this method. The Arbitrary Lagrangian Eulerian (ALE) method is a combination of the Lagrangian and Eulerian descriptions. In this formulation, the reference frame is not necessarily moving with the material (Lagrangian description) or fixed in space (Eulerian description), but can be chosen independently from the material displacement. This method was first developed in fluid mechanics, to model fluid-structure interaction [8, 9] and to model the motion of free surfaces [10, 11]. Later it was applied to the simulation of forming processes [12, 13].

In the work presented in this thesis, a semi-coupled ALE method was used [14]. This method is outlined in Figure A.3. For each iteration, the material displacement increments are first calculated with an updated Lagrangian method. For each iteration, the mesh is updated and the state variables are remapped to the new mesh. Subse-

quently the stresses are updated and convergence is checked. The iteration process is continued until a convergence criterion is met. An advantage of this model is that the system is in equilibrium at the end of the step. The disadvantage is that convergence may be less than optimal, because the mesh update is not taken into account when linearising the system.

References

[1] J. Huétink. *On the simulation of thermomechanical forming processes*. PhD thesis, University of Twente, The Netherlands, 1986.

[2] T. Belytschko, W. K. Liu, and B. Moran. *Nonlinear finite element analysis for continua and structures*. Wiley, 2000.

[3] M. E. Malvern. *Introduction to the mechanics of continuous medium*. Prentice Hall, 1969.

[4] H. G. Mooi. *Finite element simulation of aluminium extrusion*. PhD thesis, University of Twente, The Netherlands, 1996.

[5] B. Rietman. *Numerical analysis of inhomogeneous deformation in plane strain compression*. PhD thesis, University of Twente, The Netherlands, 1999.

[6] V. T. Meinders. *Developments in numerical simulations of the real-life deep drawing process*. PhD thesis, University of Twente, The Netherlands, 2000.

[7] O. C. Zienkiewicz and R. L. Taylor. *The Finite Element Method*. McGraw-Hill, London, 4th edition, 1989.

[8] T. Hughes, W. Liu, and T. Zimmermann. Lagrangian-Eulerian finite element formulation for incompressible viscous flows. *Comput. Methods Appl. Mech. Engrg.*, 29:329–349, 1981.

[9] J. Donea, S. Guiliani, and J. Halleux. An Arbitrary Lagrangian Eulerian finite element method for transient dynamic fluid structure interaction. *Comput. Methods Appl. Mech. Engrg.*, 33:689–723, 1982.

[10] A. Huerta and W. K. Liu. Viscous flow with large free surface motion. *Comput. Methods Appl. Mech. Engrg.*, 69:277–324, 1988.

[11] W. K. Liu, H. Chang, J. Chen, and T. Belytschko. Arbitrary Lagrangian-Eulerian Petrov-Galerkin finite elements for nonlinear continua. *Comput. Methods Appl. Mech. Engrg.*, 68:259–310, 1988.

[12] J. Huétink. Analysis of metal forming processes based on a combined Eulerian-Lagrangian finite element formulation. In J. F. T. Pittman et al., editors, *Numerical Methods in Industrial Forming Processes*, pages 501–509. Pineridge Press, 1982.

[13] P. Schreurs, F. Veldpaus, and W. Brekelmans. Simulation of forming processes, using the arbitrary Eulerian-Lagrangian formulation. *Comput. Methods Appl. Mech. Engrg.*, 58:19–36, 1986.

[14] H. Wisselink. *Analysis of guillotining and slitting*. PhD thesis, University of Twente, The Netherlands, 2000.

List of Symbols

Scalars:

b	length of the Burgers vector for aluminium (m)
f	yield function (MPa)
$\mathbf{f}_I^{int}$	internal force vector (N)
$\mathbf{f}_I^{ext}$	external force vector (N)
g	limit function (MPa)
h	viscoplastic modulus (MPa)
i	iteration number
l	bearing length (m)
l_D	diffusion length (m)
m	material parameter in Sellars-Tegart law ()
n	step number
o	sink-in offset (m)
p	hydrostatic pressure (MPa)
p_c	counter pressure used in bearing simulations (MPa)
r	specific heat source W/kg
s	sink-in depth (m)
s_m	material parameter in Sellars-Tegart law (MPa)
t	time (s), profile thickness (m)
t_{def}	time the material spends in the deformation zone (s)
u	specific internal energy (J/kg)
A	material parameter in Sellars-Tegart law (1/s)
C_b	bulk modulus (MPa)
D_i	diffusion coefficient of solute element i (m^2/s)
E	Young's modulus (MPa)
G	shear modulus (MPa)

I	node number
K_1	material parameter in solute dependent Sellars-Tegart law ()
K_2	material parameter in solute dependent Sellars-Tegart law (1/wt%)
N_I	interpolation function for node I ()
P	average pressure, used as measure for resistance in bearing (MPa)
Q	activation energy in Sellars-Tegart law (J/mol)
R	universal gas constant (J/molK)
S	length of inflow edge in bearing simulations (m)
T	temperature (K)
X	weighted solute content in aluminium matrix (wt%)
Z	Zener-Hollomon parameter (1/s)
α	weighting factor for return mapping algorithm ()
δ	subgrain size (m)
$\dot{\kappa}$	equivalent (visco)plastic strain rate (1/s)
$\dot{\kappa}_0$	parameter to include elastic region in Sellars-Tegart law (1/s)
$\dot{\lambda}$	plastic multiplier (1/MPas)
μ	friction coefficient ()
θ	bearing angle (°)
ρ	density (kg/m^3)
$\overline{\sigma}$	effective stress (MPa)
σ_f	flow stress (MPa)
σ_y	yield stress (MPa)
σ_i	friction stress opposing a moving dislocation (MPa)
Δt	time increment (s)
$\Delta\epsilon_q$	equivalent plastic strain increment ()
$\Delta\epsilon^{vol}$	volumetric strain increment ()
$\Delta\gamma$	scaling parameter for viscoplastic model (1/MPas)
$\Delta\kappa$	equivalent (visco)plastic strain increment ()
$\Delta\lambda$	plastic multiplier (1/MPa)

Vectors:

b	body forces (N/kg)
f	force (N)
n	normal ()
q	internal heat flux (W/m^2)
t	traction forces (N/m^2)
u	displacement (m)
v	velocity (m/s)
x	spatial coordinate (m)
X	material coordinate (m)
$\delta\mathbf{w}$	weighting function ()

Tensors:

m	direction of plastic flow ()
n	normal on the limit surface defined by $g = 0$ ()
s	deviatoric stress (MPa)
$\mathbf{B}_I$	symmetric part of the gradient of the shape functions (1/m)
D	strain rate (1/s)
$\hat{\mathbf{D}}$	corotational strain rate (1/s)
$\mathbf{D}^e$	elastic strain rate (1/s)
$\mathbf{D}^{vp}$	(visco)plastic strain rate (1/s)
F	deformation gradient ()
L	spatial velocity gradient (1/s)
I	unity tensor
Q	rotation tensor ()
R	rotation tensor ()
W	spin (1/s)
$\dot{\boldsymbol{\varepsilon}}$	strain rate (1/s)
$\dot{\boldsymbol{\varepsilon}}^e$	elastic strain rate (1/s)
$\dot{\boldsymbol{\varepsilon}}^{vp}$	(visco)plastic strain rate (1/s)
$\boldsymbol{\sigma}$	Cauchy stress (MPa)
$\hat{\boldsymbol{\sigma}}$	corotational stress (MPa)
$\overset{\circ}{\boldsymbol{\sigma}}$	corotational stress rate (MPa/s)
$\Delta\mathbf{e}$	deviatoric strain increment ()

$\Delta\boldsymbol{\varepsilon}$ strain increment ()

$\Delta\boldsymbol{\varepsilon}^e$ elastic strain increment ()

$\Delta\boldsymbol{\varepsilon}^{vp}$ (visco)plastic strain increment ()

$\Delta\boldsymbol{\sigma}$ stress increment (MPa)

4th-order tensors:

E   elastic tensor (MPa)

H   unity tensor

Samenvatting

Aluminium extrusie is een vormgevingsproces dat wordt gebruikt om profielen te maken. Een grote verscheidenheid aan profielen kan worden gemaakt door een blok heet aluminium door een gat te drukken met de vorm van de gewenste doorsnede van het profiel. Momenteel wordt het ontwerp van extrusiematrijzen en de procesbesturing voornamelijk proefondervindelijk gedaan. De ervaring van de matrijsontwerper, de persoperator en de matrijscorrector bepalen de efficiëntie van het proces. Het is noodzakelijk om meer kennis van het extrusie proces te verkrijgen om de efficiëntie te verbeteren. Numerieke simulaties kunnen hierbij helpen.

In dit proefschrift worden een aantal nieuwe ontwikkelingen op het gebied van eindige elementen simulaties van extrusie behandeld. De stof is opgedeeld in vier hoofd-stukken die in de vorm van artikelen ook elders worden gepubliceerd. De aandacht is gericht op de volgende drie onderwerpen:

- Het modelleren van de bearing

- Experimentele verificatie van de simulaties

- Het ontwikkelen van een praktische methode voor het simuleren van willekeurige profielen.

Het is gebruikelijk om een viscoplastisch constitutief model te gebruiken voor het simuleren van het materiaal gedrag van aluminium tijdens extrusie. In zo'n model wordt het elastische gedrag verwaarloosd. Dit is mogelijk omdat de plastische ver-vormingen die optreden vele malen groter zijn dan de elastische vervormingen. In het bearingkanaal zijn de vervormingen echter minimaal en elastische effecten hebben wel degelijk een belangrijke invloed op de resultaten.

131

Om de processen die in de bearing spelen te onderzoeken zijn er gedetailleerde 2D simulaties van de stroming in dit gebied gemaakt. Met deze simulaties zijn de effecten van het materiaalgedrag, de wrijving en de geometrie van de bearing onderzocht. Uit de resultaten kon worden gekonkludeerd dat elastische effecten een belangrijke rol spelen in parallelle bearings. Verder is er aangetoond dat de weerstand in parallelle bearings zeer gevoelig is voor kleine veranderingen in de geometrie en in de procescondities. Dit verklaart het onvoorspelbare gedrag van extrusiematrijzen in de praktijk. Er is een nieuwe ontwerpfilosofie voorgesteld om dit te voorkomen.

Experimentele verificatie van het numerieke model is uitgevoerd door de simulaties te vergelijken met extrusie experimenten. De numerieke simulaties zijn uitgevoerd met een elasto-viscoplastic constitutief model dat is gebaseerd op de Sellars-Tegart wet aangepast voor het effect van oplosharding. De parameters voor dit model zijn bepaald m.b.v. compressietesten. De extrusie proeven zijn isotherm uitgevoerd. De resultaten van het numerieke model geven een goede overeenkomst met de experimentele resultaten.

De toepassing van de numerieke simulaties in de extrusie praktijk wordt beperkt door de complexiteit van deze simulaties. Het is nodig om een praktische methode te ontwikkelen voor het maken van simulaties van willekeurige profielen. Er is een equivalent bearing model ontwikkeld om de weerstand in de bearing te modelleren zonder een groot aantal elementen te gebruiken. Om het tijdrovende en ingewikkelde werk van het maken van een EEM model te vermijden, is er een speciale pre-processor voor extrusie gemaakt. Hiermee is een directe koppeling tussen het matrijsontwerp in het CAD programma Pro/Engineer en de simulaties in de EEM code DiekA tot stand gekomen.

De simulaties kunnen in de praktijk gebruikt worden om specifieke aspecten van het extrusieproces te onderzoeken. De simulaties zijn al succesvol gebruikt om de vorm van de vleugels in porthole matrijzen te verbeteren en om ontwerpregels voor de bearinggeometrie af te leiden. Deze ontwerpregels zorgen voor een uniforme uitstroomsnelheid van het profiel. In principe kunnen de simulaties ook rechtstreeks in het ontwerpproces worden gebruikt om het ontwerp van specifieke matrijzen te verbeteren.